

UCLA

UCLA Electronic Theses and Dissertations

Title

Measurements and predictions of the radiation characteristics of biofuel-producing microorganisms

Permalink

<https://escholarship.org/uc/item/6935r8w1>

Author

Heng, Ri-Liang

Publication Date

2015

Peer reviewed|Thesis/dissertation

UNIVERSITY OF CALIFORNIA

Los Angeles

**Measurements and predictions of the radiation
characteristics of biofuel-producing microorganisms**

A dissertation submitted in partial satisfaction

of the requirements for the degree

Doctor of Philosophy in Mechanical Engineering

by

Ri-Liang Heng

2015

© Copyright by
Ri-Liang Heng
2015

ABSTRACT OF THE DISSERTATION

Measurements and predictions of the radiation characteristics of biofuel-producing microorganisms

by

Ri-Liang Heng

Doctor of Philosophy in Mechanical Engineering

University of California, Los Angeles, 2015

Professor Laurent Pilon, Chair

Biofuel produced from photosynthetic microorganisms offers a green and sustainable alternative to fossil fuels and bioethanol for next generation transportation fuels. Their simple cell structures enable them to be more efficient in photosynthesis than higher order plants. However, large scale cultivation of these microorganisms is typically hampered by the poor light utilization of photobioreactor systems. In order to increase biomass productivities, the light transfer in photobioreactors must be characterized and optimized. The radiation characteristics of photosynthetic microorganisms are essential parameters in this analysis. This study aims to (1) experimentally measure the radiation characteristics of various photosynthetic microorganisms of different morphologies and (2) to develop models that can predict these radiation characteristics.

First, the spectral complex indices of refraction of unicellular spheroidal green algae *Botryococcus braunii*, *Chlorella sp.*, and *Chlorococcum littorale* were retrieved from their experimentally measured average absorption and scattering cross-sections. Next, the temporal evolution of the scattering and absorbing cross-sections of marine eustigmatophycease *Nannochloropsis oculata* grown in flat-plate photobioreactor (PBR) was reported. The variations in cross-sections were found to be directly related to the up- and down-regulations of pigments and other intracellular components and vary significantly with time in response to changes in light and nutrients availability. Furthermore, this study demonstrates that

the light transfer in the PBR could be predicted using constant radiation characteristics measured during the exponential growth phase with reasonable accuracy provided that the cultures were not nitrogen limited. In addition, this study presents experimental measurements of the absorption and scattering cross-sections and the spectral complex index of refraction of filamentous heterocystous cyanobacterium *Anabaena cylindrica*. Its filaments, consisting of long chains of polydisperse cells, were modeled as infinitely long and randomly oriented volume-equivalent cylinders. Finally, it was demonstrated that the absorption and scattering cross-sections and asymmetry factor of randomly oriented and optically soft bispheres, quadspheres, and circular rings of spheres, with either monodisperse or polydisperse monomers, can be approximated by an equivalent coated sphere with identical volume and average projected area. Based on this approximation, the spectral complex index of refraction of unicellular dumbbell-shaped cyanobacterium *Synechocystis sp.* was retrieved from experimental measurements of its average absorption and scattering cross-sections and size distribution.

The dissertation of Ri-Liang Heng is approved.

Suzanne Paulson

Chih-Ming Ho

Pei-yu Chiou

Laurent Pilon, Committee Chair

University of California, Los Angeles

2015

TABLE OF CONTENTS

1	Introduction	1
1.1	Motivations	1
1.2	Biofuel Production from Microorganisms	4
1.2.1	Microbiology and Microorganisms	4
1.2.2	Solar Radiation	6
1.2.3	Photobioreactors	7
1.2.4	Challenges for Industrial Production	10
1.3	Objectives of Present Study	11
2	Background and Tasks	12
2.1	Light Harvesting Pigments	12
2.2	Radiation Transfer Through Microalgae Suspensions	14
2.3	Radiation Characteristics of Microalgae	16
2.3.1	Theoretical Prediction	17
2.3.2	Experimental Measurements	18
2.4	Effective Optical Properties of Microorganisms	19
2.4.1	Direct Experimental Measurements	19
2.4.2	Model-Based Measurements	20
2.5	Tasks	21
2.6	Organization of this document	22
3	Spectral optical properties of selected photosynthetic microalgae produc-	
	ing biofuels	23

3.1	Introduction	23
3.1.1	<i>B. braunii</i> , <i>Chlorella sp.</i> , <i>C. littorale</i>	24
3.2	Analysis	25
3.2.1	Assumptions	25
3.2.2	Equivalent diameter and size distribution	25
3.2.3	Prediction of the Radiation Characteristics of Microalgae	28
3.2.4	Optimization Algorithm	28
3.2.5	Experimental Uncertainties	31
3.3	Results and Discussions	31
3.3.1	Validation: Retrieving n_λ and d_s of Monodisperse Latex Particles	31
3.3.2	Retrieved Spectral Complex Index of Refraction of Microalgae	32
3.3.3	Discussion	35
3.4	Conclusion	36
4	Time-Dependent Radiation Characteristics of <i>Nannochloropsis Oculata</i> During Batch Culture	38
4.1	Introduction	38
4.1.1	<i>Nannochloropsis oculata</i>	40
4.2	Materials and Methods	40
4.2.1	Cultivation and sample preparation	40
4.2.2	Radiation characteristics	42
4.2.3	Chemical analysis	46
4.3	Results and Discussions	47
4.3.1	Cell growth	47
4.3.2	Mass absorption and scattering cross-sections	49

4.3.3	Average fluence rate and radiant power absorbed	52
4.4	Chapter summary	57
5	Radiation Characteristics and Optical Properties of Filamentous Cyanobac-	
	terium <i>Anabaena Cyindrica</i>	58
5.1	Introduction	58
5.1.1	<i>Anaebena cylindrica</i>	59
5.1.2	Radiation characteristics of photosynthetic microorganisms	60
5.2	Materials and Methods	61
5.2.1	Cultivation and sample preparation	61
5.2.2	Cell morphology	63
5.2.3	Radiation characteristics measurements	64
5.2.4	Effective optical properties of filamentous cyanobacteria	65
5.3	Results and Discussions	67
5.3.1	Size distribution and heterocyst frequency	68
5.3.2	Scattering phase function	70
5.3.3	Mass absorption and scattering cross-sections	71
5.3.4	Effective optical properties	76
5.4	Chapter summary	79
6	Absorption and scattering by bispheres, quadspheres, and circular rings	
	of spheres and their equivalent coated spheres	81
6.1	Introduction	81
6.2	Background	84
6.2.1	Scattering matrix	84

6.2.2	Heterogeneous and spheroidal particles	85
6.2.3	Aggregates of spherical monomers	86
6.2.4	Equivalent scattering particles	87
6.3	Analysis	89
6.3.1	Problem statement	89
6.3.2	Methodology	92
6.4	Results and discussions	95
6.4.1	Absorption and scattering cross-sections	95
6.4.2	Scattering phase function and asymmetry factor	99
6.4.3	Scattering matrix elements	103
6.4.4	Effect of the relative complex index of refraction	108
6.4.5	Aggregates of polydisperse monomers	111
6.4.6	Computational time	113
6.5	Chapter summary	114
7	Rapid and Accurate Retrieval of The Complex Index of Refraction of Aggregates and <i>Synechocystis sp.</i>	115
7.1	Introduction	115
7.1.1	<i>Synechocystis sp.</i>	116
7.1.2	Radiation characteristics of photosynthetic microorganisms	118
7.2	Analysis	120
7.2.1	Assumptions	120
7.2.2	Aggregates and their equivalent coated spheres	120
7.2.3	Inverse method algorithm	123
7.2.4	Validation of the inverse method	124

7.3	Experimental Methods	128
7.3.1	Cultivation and sample preparation	128
7.3.2	Size distribution	128
7.3.3	Radiation characteristics measurements	129
7.4	Results and discussions	131
7.4.1	Validation of inverse method	131
7.4.2	Experimental results	137
7.5	Chapter summary	143
8	Summary	145
	References	148

LIST OF FIGURES

1.1	Lifecycle diagram of microalgal biofuel production [1].	2
1.2	Schematic of input and output of photosynthetic microorganisms consuming CO ₂ and producing lipids or H ₂ [2].	5
1.3	Averaged daily extraterrestrial solar irradiance and ASTM G173-03 direct and hemispherical irradiance (in W/m ² .nm) at sea level on 37° sun-facing tilted surface [3].	6
1.4	Photographs of (a) open race-way ponds, (b) inclined-column photobioreactors, (c) flat-plate photobioreactors, and (d) tubular photobioreactors.	8
2.1	<i>In vivo</i> specific absorption coefficient Ea (in m ² /mg) of primary pigments chlorophylls <i>a</i> , <i>b</i> , and <i>c</i> and photosynthetic carotenoids (PSC), and photoprotective carotenoids (PPC) over the spectral region from 400 to 750 nm [4].	13
3.1	Number frequency $f(d_s)$ of the equivalent sphere diameter of (a) <i>B. braunii</i> ($c=0.961$, $\epsilon=1.333$), (b) <i>Chlorella sp.</i> ($c=0.965$, $\epsilon=1.301$), and (c) <i>C. littorale</i> ($c=0.975$, $\epsilon=1.212$). The equivalent diameter was estimated from Equation (3.2) and major and minor diameter distributions reported in Figure 2 in Ref. [5].	27
3.2	Block diagram of the procedure used to retrieve the refraction index n_λ and absorption index k_λ from the absorption and scattering cross-sections $\bar{C}_{abs,\lambda}$ and $\bar{C}_{sca,\lambda}$ at a given wavelength λ for number frequency $f(d_s)$. We used N=120 individuals per generation for a maximum of 50 generations. n_λ and k_λ were allowed to range from 1.33 to 1.53 and from 10 ⁻⁵ to 0.01, respectively.	30
3.3	Comparison of the retrieved refraction and absorption indices between 400 and 750 nm for <i>B. braunii</i> , <i>Chlorella sp.</i> , and <i>C. littorale</i> using their number frequency $f(d_s)$	33

4.1	Schematic of experimental setup used to determine (a) the extinction coefficient β_λ from normal-normal spectral transmittance and (b) the absorption coefficient κ_λ from normal-hemispherical spectral transmittance.	43
4.2	Cell number density evolution with respect to growth times for <i>N. oculata</i> batch cultures grown under 7,500 and 10,000 lux of red light. Lag, exponential, and stationary phases and onset of nitrogen starvation are also shown.	47
4.3	(a) and (b) Average absorption cross-section $\bar{C}_{abs,\lambda}$ and (c) and (d) average scattering cross-section $\bar{C}_{sca,\lambda}$ in the spectral range from 400 to 750 nm for <i>N. oculata</i> grown under 7,500 and 10,000 lux, respectively.	49
4.4	(a) and (b) Temporal evolutions of average absorption cross-section at 485 and 676 nm and (c) and (d) pigment concentrations (Chl <i>a</i> and carotenoids) for <i>N. oculata</i> grown under 7,500 and 10,000 lux, respectively.	51
4.5	Evolution of the average fluence rate in the flat-plate PBR as a function of time for cultures grown under (a) 7,500 lux and (b) 10,000 lux predicted using Equation (2.8) to (2.11) and (i) time-dependent $\bar{C}_{abs,\lambda}$ and $\bar{C}_{sca,\lambda}$ and (ii) $\bar{C}_{abs,\lambda}$ and $\bar{C}_{sca,\lambda}$ measured after ~ 140 hours during the exponential phase.	54
4.6	Evolution of the average radiant power absorbed per microalgae cell A_{ave} [Equation (2.12)] for cultures grown under 7,500 and 10,000 lux.	56
5.1	Micrograph image of <i>A. cylindrica</i> showing vegetative cells and heterocysts 2.5-3 μm in diameter. Reproduced with permission from Prof. Yuuji Tsukii, Hosei University, Protist Information Server http://protist.i.hosei.ac.jp	59
5.2	Block diagram of the procedure used to retrieve the refraction index n_λ and absorption index k_λ from the measured absorption and scattering cross-sections per unit length $\bar{C}'_{abs,\lambda}$ and $\bar{C}'_{sca,\lambda}$ at a given wavelength λ for volume-equivalent diameter distribution $f(d_{c,eq})$. Here, P=100 individuals per generation for a maximum of 500 generations.	66

5.3	Histograms of volume-equivalent diameter distribution $f(d_{c,eq})$ of <i>A.cylindrica</i> filaments for Samples 1, 2, 3, and 4 at concentrations (a) $X_1 = 0.086 \text{ kg/m}^3$, (b) $X_2 = 0.108 \text{ kg/m}^3$, (c) $X_3 = 0.151 \text{ kg/m}^3$, and (d) $X_4 = 0.171 \text{ kg/m}^3$ obtained from more than 1120 cells for each sample.	69
5.4	Scattering phase function of <i>A.cylindrica</i> at 633 nm measured experimentally using a polar nephelometer and predicted using the retrieved values of n_{633} and k_{633} for Sample 3 with $x_w = 0.75$	70
5.5	(a) Absorption coefficient κ_λ , (b) scattering coefficient $\sigma_{s,\lambda}$, (c) average mass absorption cross-section $\bar{A}_{abs,\lambda} = \kappa_\lambda/X$, and (d) average mass scattering cross-section $\bar{S}_{sca,\lambda} = \sigma_{s,\lambda}/X$ from 400 to 750 nm of <i>A.cylindrica</i> in Sample 3 for mass concentrations $X_{3,1} = 0.431$, $X_{3,2} = 0.296$, and $X_{3,3} = 0.202 \text{ kg/m}^3$. . .	72
5.6	Average mass (a) absorption $\bar{A}_{abs,\lambda}$ and (b) scattering cross-sections $\bar{S}_{sca,\lambda}$ from 400 to 750 nm of <i>A.cylindrica</i> for Samples 1, 2, 3, and 4 collected after day 6, 9, 12, and 14, respectively.	74
5.7	Retrieved (a) refraction n_λ and (b) absorption k_λ indices between 400 to 750 nm for <i>A.cylindrica</i> assuming water mass fraction to be $x_w = 0.75$ or 0.85 for Samples 1, 2, 3, and 4 collected after day 6, 9, 12, and 14, respectively. . . .	77
6.1	Micrographs of cyanobacteria: (a) free floating <i>Synechocystis sp.</i> , (b) <i>Synechocystis sp.</i> immediately after cell division, (c) <i>Anabaenopsis elenkinii</i> , and (d) <i>Anabaenopsis circularis</i> . Reproduced with permission from (a), (b) Prof. Yuuji Tsukii (Hosei University), (c) Dr. Seija Hällfors (University of Jyväskylä Biology Department and (d) Dr. Roger Burks (University of California at Riverside), Prof. Mark Schneegurt (Wichita State University), and Cyanosite.	83

6.2	Schematic of simulated (a) bispheres, (b) quadspheres, and (c) rings of spheres with $N_s = 5$ and 10 monodisperse monomers of radius r_s and complex index of refraction $m_s = n_s + ik_s$ surrounded by a non-absorbing medium of refraction index n_m . These idealized aggregates are representative of the cyanobacteria shown in Figure 7.1.	90
6.3	Schematic of the projected area of a bisphere onto the x-y plane when viewed along the z-axis.	93
6.4	Absorption cross-section of randomly oriented (a) bispheres and quadspheres and (b) rings of $N_s = 10$ and 20 spheres and of their corresponding equivalent spheres and coated spheres as a function of monomer size parameter χ_s ranging from 0.01 to 10 for $m = 1.03 + i0.004$. Relative errors in the absorption cross-section between the T-matrix predictions and the equivalent particles for (c) bispheres, (e) quadspheres (d) rings of 10 spheres, and (f) rings of 20 spheres.	96
6.5	Scattering cross-section of randomly oriented (a) bispheres and quadspheres and (b) rings of $N_s = 10$ and 20 spheres and of their corresponding equivalent spheres and coated spheres as a function of monomer size parameter χ_s ranging from 0.01 to 10 for $m = 1.03 + i0.004$. Relative errors in the scattering cross-sections between the T-matrix predictions and the equivalent particles for (c) bispheres, (e) quadspheres, (d) rings of 10 spheres, and (f) rings of 20 spheres.	97
6.6	(a) Absorption and (b) scattering cross-sections of bispheres, quadspheres, rings of 10 and 20 spheres as functions of $N_s\chi_s^3$ and $N_s^2\chi_s^6$, respectively.	99
6.7	Scattering phase function $F_{11}(\Theta)$ as a function of scattering angles Θ for (a) bispheres, (b) quadspheres, and rings of spheres with (c) $N_s = 10$ and (d) $N_s = 20$ monomers with monomer size parameters $\chi_s = 0.01, 0.1, 1$, and 10 and $m = 1.03 + i0.004$ along with those for their corresponding volume and average projected area equivalent coated spheres.	100

6.8	Asymmetry factor g as a function of monomer size parameter χ_s ranging from 0.01 to 10 with $m = 1.03 + i0.004$ for (a) bispheres, (b) quadrspheres, and rings of spheres with (c) $N_s = 10$ and (d) $N_s = 20$ monomers and for their corresponding equivalent volume and average projected area coated spheres.	102
6.9	Scattering matrix element ratios (a) and (b) $-F_{12}/F_{11}$, (c) and (d) F_{33}/F_{11} , (e) and (f) F_{44}/F_{11} , and (g) and (h) F_{34}/F_{11} as functions of scattering angle Θ obtained with the T-matrix method for bispheres and quadrspheres and for the corresponding volume and average projected area equivalent coated spheres for monomer size parameters $\chi_s = 0.01$, 0.1, 1, and 10.	105
6.10	Scattering matrix element ratios (a) and (b) $-F_{12}/F_{11}$, (c) and (d) F_{33}/F_{11} , (e) and (f) F_{44}/F_{11} , and (g) and (h) F_{34}/F_{11} as functions of scattering angle Θ obtained with the T-matrix method for rings of 10 spheres and 20 spheres, respectively, and for the corresponding volume and average projected area equivalent coated spheres for monomer size parameters $\chi_s = 0.01$, 0.1, 1, and 10.	107
6.11	(a)-(d) Absorption and (e)-(h) scattering cross-sections and (i)-(l) asymmetry factors of bispheres, quadrspheres, and rings of 10 and 20 spheres, respectively, as functions of monomer size parameters χ_s ranging from 0.01 to 10 and their corresponding volume and average projected area equivalent coated spheres with different complex indices of refraction.	109
7.1	Micrographs of (a) free floating dumbbell-shaped <i>Synechocystis sp.</i> cell with lengths $r_{s,1}$ and $r_{s,2}$ about 1 μm long and (b) <i>Synechocystis sp.</i> immediately after cell division. Reproduced with permission from Prof. Yuuji Tsukii (Hosei University, http://protist.i.hosei.ac.jp/).	117

7.2	Schematics of (a) a bisphere, (b) a quadsphere, (c) a fractal aggregate of spherical monomer of radius r_s , and (d) an average projected area and volume equivalent coated sphere with inner radius $r_{eq,i}$ and outer radius $r_{eq,o}$. The monomers and the coating of the coated sphere had the same complex index of refraction $m_{s,\lambda}$. The surrounding medium and the core of the coated sphere were non-absorbing with refraction index $n_{m,\lambda}$	121
7.3	Block diagram of the procedure used to retrieve the refraction index $n_{s,\lambda}$ and absorption index $k_{s,\lambda}$ from the measured average spectral absorption and scattering cross-sections $\bar{C}_{abs,\lambda}$ and $\bar{C}_{sca,\lambda}$ and the volume and average projected area equivalent coated sphere radii distribution $f(r_{eq,i}, r_{eq,o})$. Here, P=100 individuals per generation for a maximum of 500 generations. The objective function δ_λ to be minimized is defined in Equation (7.7).	123
7.4	Histograms of the bisphere and quadsphere monomer radius frequency distribution and the equivalent coated sphere radii frequency distribution of Suspensions 1 and 2, respectively.	125
7.5	Histograms of the monomer number frequency distribution of Suspension 3 and Suspension 4, respectively and of the corresponding equivalent coated sphere radii frequency distribution.	126
7.6	(a) and (b) Absorption $\bar{C}_{abs,\lambda}$ and (c) and (d) scattering cross-section $\bar{C}_{sca,\lambda}$ as functions of relative refractive n_λ and absorption k_λ indices for Suspensions 1 and 2, respectively.	132
7.7	Contour plots of the sum of relative errors ϵ between the input and retrieved refraction and absorption index as a function of relative refraction n and absorption index k of the monomers in Suspensions (a) 1 and (b) 2, respectively. The dots on the contour plots represent the location of the computed data points.	134

7.8	Histograms of (a) the measured <i>Synechocystis sp.</i> radius distribution $f_{b,exp}(r_s)$ and of (b) the equivalent coated sphere radii distribution $f_{exp}(r_{eq,i}, r_{eq,o})$	138
7.9	Scattering phase function of <i>Synechocystis sp.</i> at 633 nm as a function of scattering angle θ from 0 to 180° measured experimentally using a polar nephelometer and predicted using the equivalent coated sphere approximation in conjunction with $f_{exp}(r_{eq,i}, r_{eq,o})$, plotted in Figure 8, and n_{633} and k_{633} , retrieved using the inverse method.	139
7.10	Measured (a) absorption coefficient κ_λ , (b) scattering coefficient $\sigma_{s,\lambda}$, (c) average absorption cross-section $\bar{C}_{abs,\lambda} = \kappa_\lambda/N_T$, and (d) average scattering cross-section $\bar{C}_{sca,\lambda} = \sigma_{s,\lambda}/N_T$ of <i>Synechocystis sp.</i> as functions of wavelength λ from 400 to 750 nm for cell number densities $N_{T,1} = 1.89 \times 10^{13}$ cells/m ³ and $N_{T,2} = 8.16 \times 10^{12}$ cells/m ³	140
7.11	Retrieved effective (a) refraction n_λ and (b) absorption k_λ indices of <i>Synechocystis sp.</i> as functions of wavelength λ from 400 to 750 nm using the inverse method shown in Figure 3 with $f_{exp}(r_{eq,i}, r_{eq,o})$, $\bar{C}_{abs,\lambda}$, and $\bar{C}_{sca,\lambda}$ plotted in Figures 8 and 10, respectively.	142

LIST OF TABLES

1.1	Comparison of oil yield from certain plants and microalgae [6].	3
1.2	Advantages and limitations of various culture systems for algae [7].	9
6.1	Comparison between absorption and scattering cross-sections and asymmetry factor of randomly oriented rings of polydisperse spherical monomers and their volume and average projected area equivalent coated spheres. Here also, $m = 1.03 + i0.004$	112
7.1	Comparison of (i) the relative refractive n_λ and absorption k_λ indices and size parameter χ_s of the monomers used as input in T-matrix method to compute the average absorption $\bar{C}_{abs,\lambda}$ and scattering $\bar{C}_{sca,\lambda}$ cross-sections in Suspensions 3 and 4 and (ii) those retrieved by inverse method treating the aggregates as homogeneous volume and average projected area equivalent coated spheres.	136

NOMENCLATURE

A_{ave}	average radiant power absorbed per cell, $\mu\text{mol/s/cell}$
\bar{A}_{abs}	average mass absorption cross-section, m^2/kg
\bar{A}_p	aggregate average projected area
b_λ	backward scattering ratio
c_i	pigment mass concentration, kg/m^3
\bar{C}_{abs}	average absorption cross-section, m^2
\bar{C}_{ext}	average extinction cross-section, m^2
\bar{C}_{sca}	average scattering cross-section, m^2
D_f	fractal dimension
d_s	equivalent sphere diameter, μm
Ea	<i>in vivo</i> pigment specific absorption cross-section, m^2/kg
$[F(\Theta)]$	Stokes matrix
f	number frequency distribution
G_{in}	incident irradiance, $\mu\text{mol}_{h\nu}/\text{m}^2\cdot\text{s}$
G	fluence rate, $\mu\text{mol}_{h\nu}/\text{m}^2\cdot\text{s}$
g_λ	Henyey-Greenstein asymmetry factor
I	radiation intensity, $\text{W}/\text{m}^2\cdot\text{nm}\cdot\text{sr}$
k	absorption index
k_f	fractal prefactor
L	PBR thickness, cm
l	cuvette pathlength, cm
m	relative complex index of refraction
n	refractive index
N_s	number of monomers per aggregate
N_T	cell number density, cells/m^3
OD	optical density

p	cell size distribution
Q_{abs}	absorption efficiency factor
Q_{sca}	scattering efficiency factor
\mathbf{r}	location vector, m
r_s	equivalent sphere radius, μm
R_g	radius of gyration, μm
\hat{s}	direction vector
\bar{S}_{sca}	average mass scattering cross-section, m^2/kg
T	transmittance
t	time, hours
x_w	water volume fraction
X	biomass concentration, kg/m^3
V	microalgae sample volume, m^3
V_{32}	mean particle volume, m^3
V_T	aggregate total volume, μm^3
w	pigment mass fraction
$[Z(\Theta)]$	Mueller matrix
z	PBR depth coordinate, cm

Greek symbols

α	two-flux model coefficient
β	extinction coefficient, m^{-1}
δ	two-flux model coefficient
κ	absorption coefficient, m^{-1}
χ	apparent extinction coefficient, m^{-1}
χ_s	monomer size parameter
ϵ	spectrometer correction factor
λ	wavelength, nm

Ω	solid angle, sr
Φ_λ	scattering phase function
ρ_{dm}	dry mass density, kg/m ³
ρ_λ	reflectance
σ_s	single scattering coefficient, m ⁻¹
Θ	scattering angle, degrees

Subscripts

<i>abs</i>	absorbed
<i>ave</i>	average
<i>b</i>	bisphere
<i>h</i>	normal-hemispherical
<i>i</i>	inner
<i>inc</i>	incident
<i>n</i>	normal-normal
<i>o</i>	outer radius
<i>q</i>	quadsphere
<i>s, eq</i>	surface area equivalent
<i>sca</i>	scattered
$\bar{A}_{p, eq}$	average projected area equivalent

ACKNOWLEDGMENTS

I would like to thank my advisor, Professor Laurent Pilon, for his guidance and encouragement throughout the duration of my doctoral work. My thanks also go to Professors Chi-ming Ho, Eric Chiou, and Suzanne Paulson for their contribution as members of my thesis committee. I would also like to acknowledge my fellow student collaborators Euntaek Lee and Razmig Kandillian. Finally, I would like to dedicate this dissertation to my loving parents Wui-Tong and Bee-Lay Heng. A special thanks to my grandmother and sister for all their love and support.

VITA

- 2011 B.S., Mechanical Engineering
 Nanyang Technological University
 Singapore, Singapore
- 2013 M.S., Mechanical Engineering
 University of California Los Angeles
 Los Angeles, CA

PUBLICATIONS

E. Lee, R.L. Heng, and L. Pilon, Spectral optical properties of selected photosynthetic microalgae producing biofuels, *Journal of Quantitative Spectroscopy and Radiative Transfer*, Vol. 114, pp. 122-135, 2013.

R.L. Heng and L. Pilon, Time-dependent radiation characteristics of *Nannochloropsis oculata* during batch culture, *Journal of Quantitative Spectroscopy and Radiative Transfer*, Vol. 144, pp. 154-163, 2014.

R.L. Heng, E. Lee, and L. Pilon, Radiation characteristics and optical properties of filamentous cyanobacterium *Anabaena cylindrica*, *Journal of the Optical Society of America A*, Vol. 31, No. 4, pp. 836-845, 2014.

R. Kandilian, R.L. Heng, and L. Pilon, Absorption and scattering by fractal aggregates and by their equivalent coated spheres, *Journal of Quantitative Spectroscopy and Radiative Transfer*, Vol. 151, pp. 310-326, 2015.

R.L. Heng, K.C. Sy, and L. Pilon, Absorption and scattering by bispheres, quadspheres, and circular rings of spheres and their equivalent coated spheres, *Journal of the Optical Society of America A*, Vol. 32, No. 1, pp. 46-60, 2015.

CHAPTER 1

Introduction

This chapter presents the motivations of this study. First, it discusses the effects of using fossil fuels for energy production and also the increasing need to find sustainable alternatives. Next, it describes the advantages of using biofuels and the different types of crops that produce them. Then, the chapter focuses on the biology of biofuel producing microorganisms and their cultivation methods. Finally, the chapter presents the existing challenges that have to be overcome in order for microalgal biofuel production to be economically viable as well as the objectives of this study.

1.1 Motivations

The prolonged reliance on fossil fuels for producing energy has resulted in an accumulation of greenhouse gases in the atmosphere, which due to greenhouse effect, causes rising sea levels and global climate change [8]. While global energy consumption is expected to increase steadily by 39% over the next two decades [9], the supply of fossil fuels remain finite and is being depleted at an increasing rate. Also, geopolitical instability in oil-rich regions is a major concern for many nations seeking to ensure their energy security. Hence, finding sustainable solutions to meet global energy demands and mitigating the resulting environmental damage are key issues needing to be addressed.

Industrialization of the emerging economies of developing nations is one of the main reasons for increasing energy demands. Among the various energy intensive sectors, transportation has shown the highest growth in greenhouse gases emission and is expected to

increase energy usage by 60% by 2030 [10]. Today, energy for transportation comes almost exclusively from petroleum [9, 11]. These observations call for the urgent development of clean and sustainable transportation fuels.

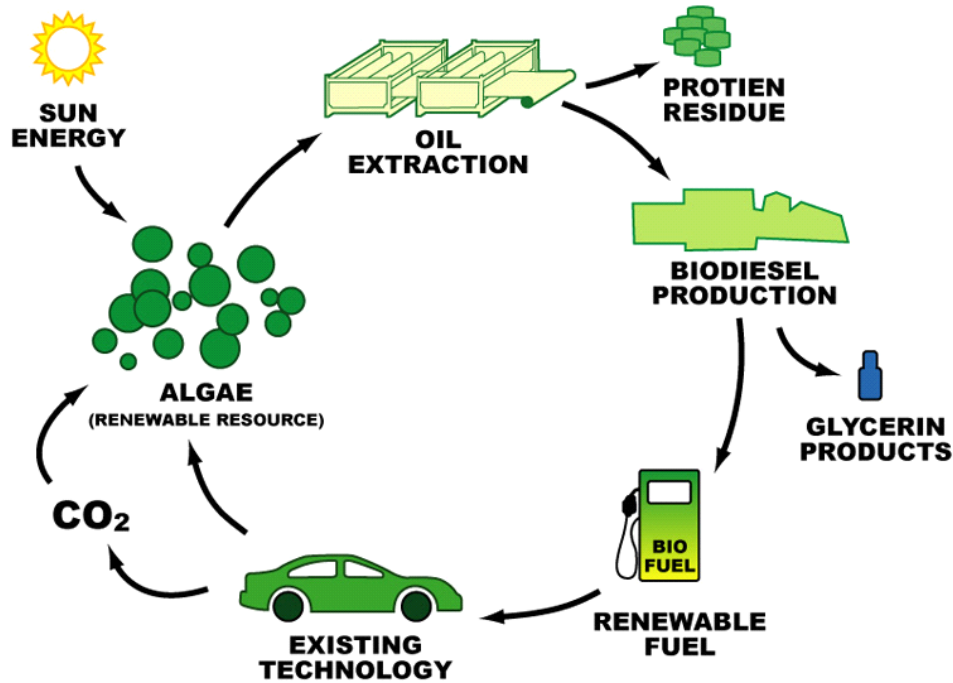


Figure 1.1: Lifecycle diagram of microalgal biofuel production [1].

Despite recent emphasis surrounding electric vehicles, the production of electricity remains dependent on fossil fuels. In contrast, biofuels may prove to be a more promising and practical solution. Figure 1.1 shows the biodiesel life cycle where renewable resources such as microalgae utilize carbon dioxide and solar radiation to produce hydrogen or lipids which can be refined into biodiesel. Biofuels are deemed to be carbon-neutral as its production and consumption does not add to the carbon dioxide concentration already present in the atmosphere. In addition, existing infrastructures and vehicle technologies are already compatible with liquid biofuels.

Bioethanol is currently produced from various food crops such as corn, sugar cane, and palm oil [11]. It is typically blended with regular gasoline (up to 10%) to reduce carbon

Crop	Oil yield (L/ha)	Land area needed (M ha) ^a	Percent of existing US cropping area ^a
Corn	172	1540	846
Soybean	446	594	326
Canola	1190	223	122
Jatropha	1892	140	77
Coconut	2689	99	54
Oil palm	5950	45	24
Microalgae ^b	136,900	2	1.1
Microalgae ^c	58,700	4.5	2.5

^a For meeting 50% of all transport fuel needs of the United States.

^b 70% oil (by wt) in biomass.

^c 30% oil (by wt) in biomass.

Table 1.1: Comparison of oil yield from certain plants and microalgae [6].

monoxide and dioxide emissions of internal combustion engines. However, bioethanol production has been controversial (i) due to the intensive use of arable land, sometimes associated with deforestation, (ii) extensive freshwater needs, and (iii) the stress put on world food markets resulting in higher food prices [6]. In contrast, microalgae has shown great potential for biofuel production as they are more efficient in utilizing solar energy to convert carbon dioxide to biomass than higher plants due to their simple single-celled structure. The microbial oil content in microalgae is known to reach values as high as 75% dry weight [6]. Table 1.1 shows that displacing 50% of all transport fuel needs of the country would require only 1.1-2.5% of the existing cropping area in the United States for microalgae cultivation [6]. In contrast, it would require 846% of existing cropping area for corn which is currently the main feedstock for bioethanol production in the United States [12]. Despite multiple advantages, the technology of microalgal biofuel is not ready for commercial production and faces many challenges before implementation.

1.2 Biofuel Production from Microorganisms

1.2.1 Microbiology and Microorganisms

Microorganisms can be classified into two major groups known as prokaryotes and eukaryotes. Unlike prokaryotes, eukaryotes have a nucleus where the genetic material is stored and other membrane-enclosed organelles [13]. In general, bacteria are prokaryotes while algae are eukaryotes [14]. Despite this difference, cyanobacteria and purple non-sulphur bacteria are often mistakenly referred to as microalgae due to their ability to utilize sunlight for photosynthesis. Photosynthesis consist of two reactions namely light and dark reactions. During light reactions, solar energy is converted to chemical energy and stored as adenosine triphosphate (ATP) and nicotinamide adenine dinucleotide phosphate (NADPH) [2]. Metabolic processes in the cell use ATP as an energy source while NADPH acts as a reducing agent for anabolic reactions [2, 15]. The subsequent dark reactions uses the products from the light reaction to fix CO_2 [2, 16]. Figure 1.2 presents a schematic showing the inputs and outputs of photosynthetic microorganisms.

Photosynthetic microorganisms contain chlorophyll pigments and use water as their electron source, sunlight as their energy source and CO_2 as their carbon source to produce oxygen, carbohydrates and lipids [17]. In addition, some species of cyanobacteria are able to fix atmospheric nitrogen N_2 and nitrous oxide NO_x and play an important role in global nitrogen cycle [14, 18].

Photosynthetic microorganisms produce lipids that are used in structural components of cells, cell storage, and cellular signaling [2, 19]. The lipids produced can be classified into a broad group of molecules [2, 19]. Among this group, neutral lipids which are also known as triacylglycerols are the most relevant to biofuel production [2, 19]. Neutral lipid production involves synthesizing of fatty acids using the products of photosynthesis, additional ATP and NADPH [2]. The fatty acids are then reacted in direct glycerol pathways to form triacylglycerols [2, 20, 21]. Under low irradiance, production of structural polar lipids is favored whereas high irradiance increases the production and accumulation of neutral lipids

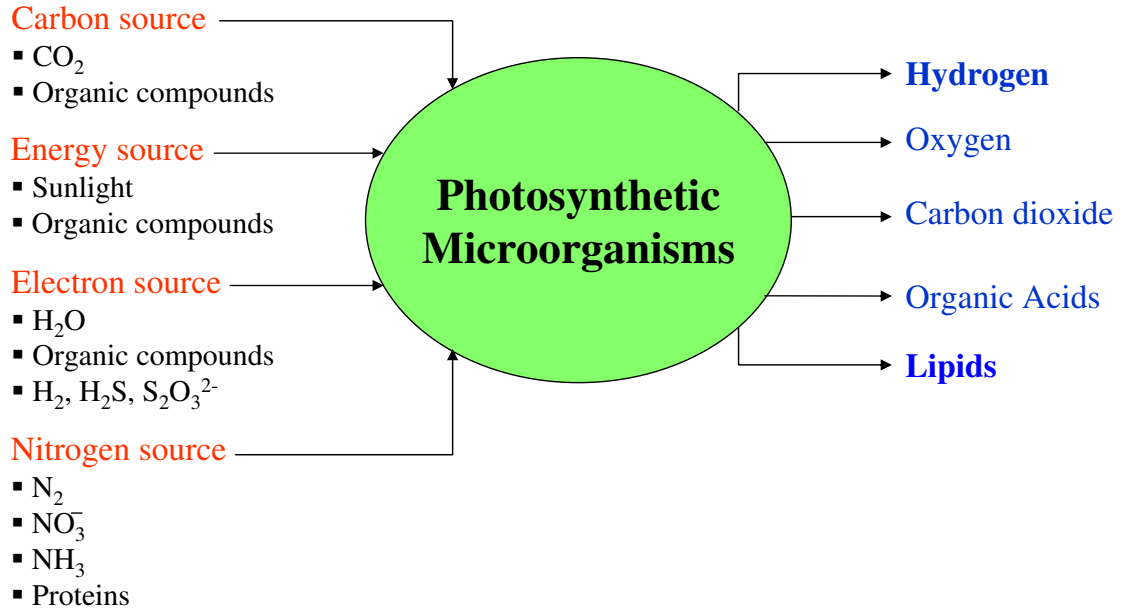


Figure 1.2: Schematic of input and output of photosynthetic microorganisms consuming CO_2 and producing lipids or H_2 [2].

in cells [22, 23].

Limitations of the inputs illustrated in Figure 1.2 may cause the microorganisms to change their photosynthetic products [6, 24]. For example, green algae and cyanobacteria are capable of producing hydrogen under anaerobic conditions. Similarly, nitrogen and phosphorus starvation of marine green algae *Nannochloropsis sp.* can increase its lipid content by up to 60% [25]. In addition to biofuel production, photosynthetic microorganisms can be cultivated to produce a variety of valuable products such as nutritional supplements, natural dyes, cosmetics, and fertilizers [26, 27]. Furthermore, they can be used to remove metal contaminants, phosphates, and nitrates from effluent water [27] and/or to reduce carbon dioxide emissions from industrial exhaust gases [28].

1.2.2 Solar Radiation

To minimize expense, microalgae production must rely on freely available sunlight [6]. The total solar irradiance at the outer surface of Earth's atmosphere and oriented perpendicular to the sun's rays was measured to be 1367 W/m^2 [2,29]. Due to the absorption and scattering effect of gases and aerosol particles, solar irradiance is attenuated when it travels through the atmosphere. The attenuation effect can be seen from Figure 1.3 which shows the spectral solar irradiance between 250 and 4000 nm at the extraterrestrial level and at the earth's surface.

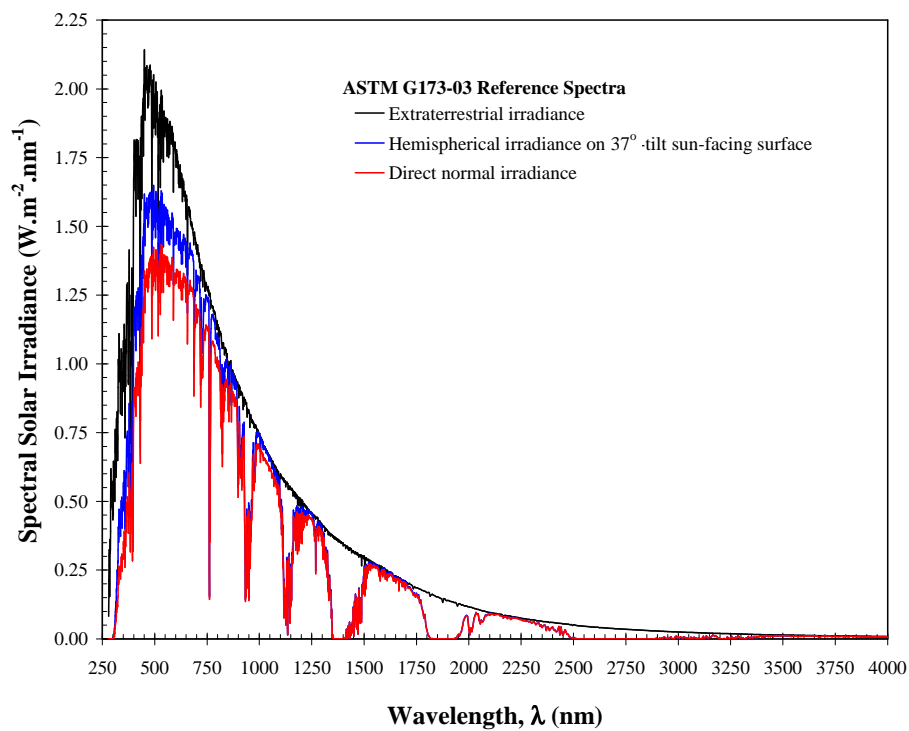


Figure 1.3: Averaged daily extraterrestrial solar irradiance and ASTM G173-03 direct and hemispherical irradiance (in $\text{W/m}^2.\text{nm}$) at sea level on 37° sun-facing tilted surface [3].

Oxygen and ozone molecules absorb most of the ultraviolet (UV) component while small gas molecules such as oxygen (O_2) and water molecules H_2O scatter the visible component [2].

Water vapor and greenhouse gases such as carbon dioxide (CO_2), carbon monoxide (CO), nitrous oxide (N_2O), and methane (CH_4) absorb the near-infrared part of the spectrum [2]. The sun delivers 6.38×10^{19} Wh/year on the surface of the atmosphere and this amount exceeds the 2011 world energy consumption rate of 1.42×10^{17} Wh/year [2, 9, 30]. Thus, the ability to effectively harness this abundant amount of solar energy can help reduce the reliance on fossil fuels.

1.2.3 Photobioreactors

At present, producing biofuels using microorganisms is not economically viable. Despite this, commercial production of microalgae in other industries has existed since the early 1970s' [7]. *Spirulina* biomass is used as a health supplement and cultivated in open pond systems. One of the largest production sites include Lake Texcoco in central Mexico. In the United States, microalgae has been employed for water treatment purposes [31]. The biomass recovered was decomposed to produce methane which can then be burnt to produce energy [31].

Photosynthetic microorganisms are typically cultivated in open or closed photobioreactor (PBR) systems. Open culture systems such as raceway ponds are comparatively low-cost and easy to operate but suffer from contamination, occupy large land areas and suffer high evaporative losses of water [6, 7]. In contrast, closed culture systems enable better control of cultivation conditions and lower risk of contamination [6, 7]. Table 1.2 summarizes the advantages and limitations of various commonly used photobioreactors such as (1) open ponds, (2) vertical-column, (3) flat-plates, and (4) tubular. Figure 1.4 shows photographs of the most common open and closed photobioreactors. Vertical-column photobioreactors have small illumination surface area which decreases upon scaling up [6, 7]. However, it offers good mixing with low shear stress and is easy to sterilize. On the other hand, flat-plate and tubular photobioreactors have large illumination areas but suffer from microalgae growing on the walls of the photobioreactors [7]. Despite higher biomass production rates, closed culture systems are costlier than open ponds and there has been much debate over which

system is more favorable for biofuel production.

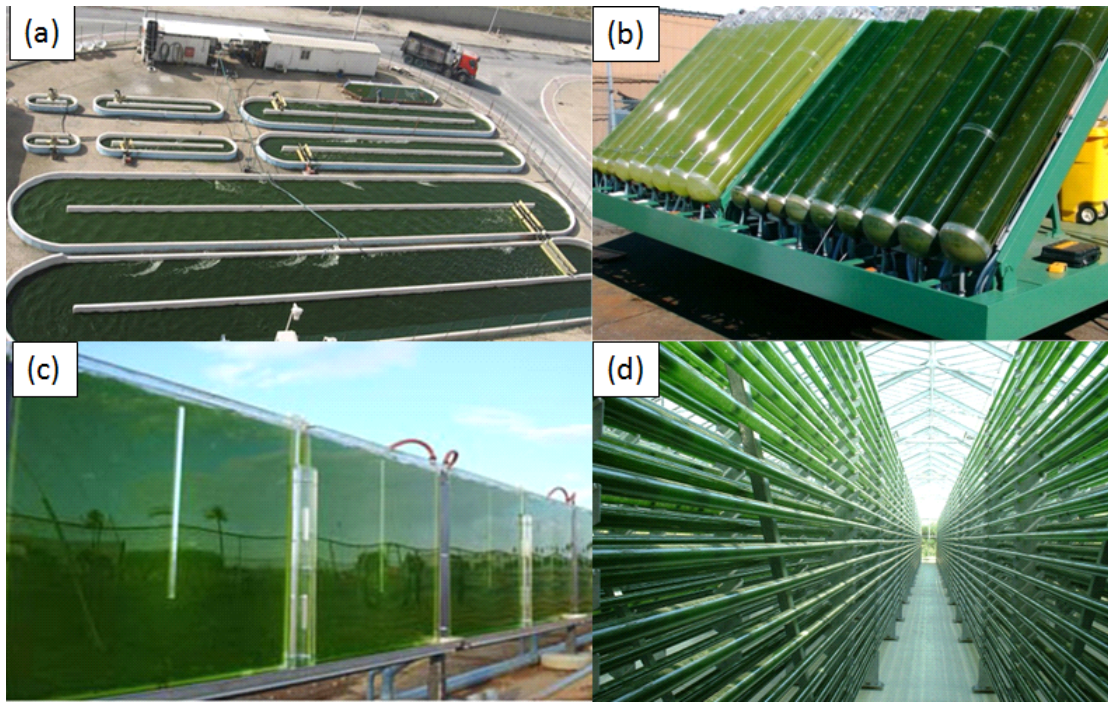


Figure 1.4: Photographs of (a) open race-way ponds, (b) inclined-column photobioreactors, (c) flat-plate photobioreactors, and (d) tubular photobioreactors.

Culture systems	Prospects	Limitations
Open ponds	Relatively economical, easy to clean up after cultivation, good for mass cultivation of algae	Little control of culture conditions, difficulty in growing algal cultures for long periods, poor productivity, occupy large land mass, limited to few strains of algae, cultures are easily contaminated
Vertical-column photobioreactors	High mass transfer, good mixing with low shear stress, low energy consumption, high potentials for scalability, easy to sterilize, readily tempered, good for immobilization of algae, reduced photoinhibition and photo-oxidation	Small illumination surface area, their construction require sophisticated materials, shear stress to algal cultures, decrease of illumination surface area upon scale-up
Flat-plate photobioreactors	Large illumination surface area, suitable for outdoor cultures, good for immobilization of algae, good light path, good biomass productivities, relatively cheap, easy to clean up, readily tempered, low oxygen build-up	Scale-up require many compartments and support materials, difficulty in controlling culture temperature, some degree of wall growth, possibility of hydrodynamic stress to some algal strains
Tubular photobioreactors	Large illumination surface area, suitable for outdoor cultures, fairly good biomass productivities, relatively cheap	Gradients of pH, dissolved oxygen and CO ₂ along the tubes, fouling, some degree of wall growth, requires large land space

Table 1.2: Advantages and limitations of various culture systems for algae [7].

1.2.4 Challenges for Industrial Production

In order to be economically viable, the cost of microalgal biofuel for consumers must be comparable to fossil fuels. This can be achieved through government policies and improvements in production processes [32]. Currently, the two major obstacles that prevent commercial production are (1) the production of biomass and (2) conversion process of biomass to biofuel [32, 33].

First, biomass separation from the culture medium is usually performed by centrifugation, filtration, coagulation-flocculation, and flotation [34]. Lipid extraction from the resulting dry biomass can be achieved by various techniques such as mechanical expulsion, solvent extraction, and supercritical fluid extraction [32, 35]. Finally, the lipids are converted to biodiesel through transesterification with alcohols using catalysts [11, 32]. These processes are energy intensive and require large amounts of additional raw materials and energy. For microalgal biofuel to become feasible at industrial scale, the entire procedure has to be more cost-effective.

Moreover, biomass productivity is severely hampered by low light energy conversion efficiencies in photobioreactor systems [2]. Due to light absorption and scattering by the microorganisms, incident light is rapidly attenuated in the culture resulting in an inhomogeneous light distribution [36]. Indeed, photosynthetic microorganisms require an optimal level of irradiance to achieve their maximum photosynthetic rate [37]. In regions directly exposed to sunlight, the light intensity may be excessively high causing photoinhibition due to photo-oxidative damage to the microorganisms' light-receiving antennas [38, 39]. On the other hand, deeper in the PBR, light intensity may be very low. Then, the cells are unable to carry out photosynthesis resulting in a significant decrease in photosynthetic activities, biomass growth, and lipid production rate [2, 37, 40]. Therefore, PBR designs must be improved so that light can be utilized more efficiently [37].

1.3 Objectives of Present Study

In order to characterize and optimize light transfer in photobioreactors in order to improve biofuel production rates, the radiation characteristics of photosynthetic microorganisms are essential properties. The main objective of the present study is to measure and/or predict these radiation characteristics.

CHAPTER 2

Background and Tasks

This chapter presents the technical background of this study. The basic components of the photosynthesis process in microorganisms are explained. In addition, the fundamentals of radiation transport in photobioreactors and the radiation characteristics of microorganisms are introduced. The chapter concludes by describing the tasks that were carried out in order to achieve the objectives of this study.

2.1 Light Harvesting Pigments

Photosynthesis is the process which converts light energy into chemical energy in plants, green algae, cyanobacteria, and other photosynthetic microorganisms [17]. It begins with the absorption of photons by the photosynthetic apparatus which consists of three major components (i) the reaction center, (ii) the core antenna, and (iii) the peripheral antenna. Photochemical charge separation and electron transport take place in the reaction center [17]. The core antenna contains the photosynthetic pigments chlorophylls or bacteriochlorophylls. It is surrounded by the peripheral antenna which is an assembly of chlorophylls, bacteriochlorophylls, and other accessory pigments such as carotenoids and phycobiliproteins. The peripheral antenna is particularly important in channeling additional photon energy to the reaction center at small light intensities. In microalgae and cyanobacteria, the photosynthetic apparatus is located on the photosynthetic membrane called thylakoid [41].

Different pigment molecules absorb over different spectral bands of the visible and near infrared parts of the spectrum enabling more efficient utilization of solar energy. Figure

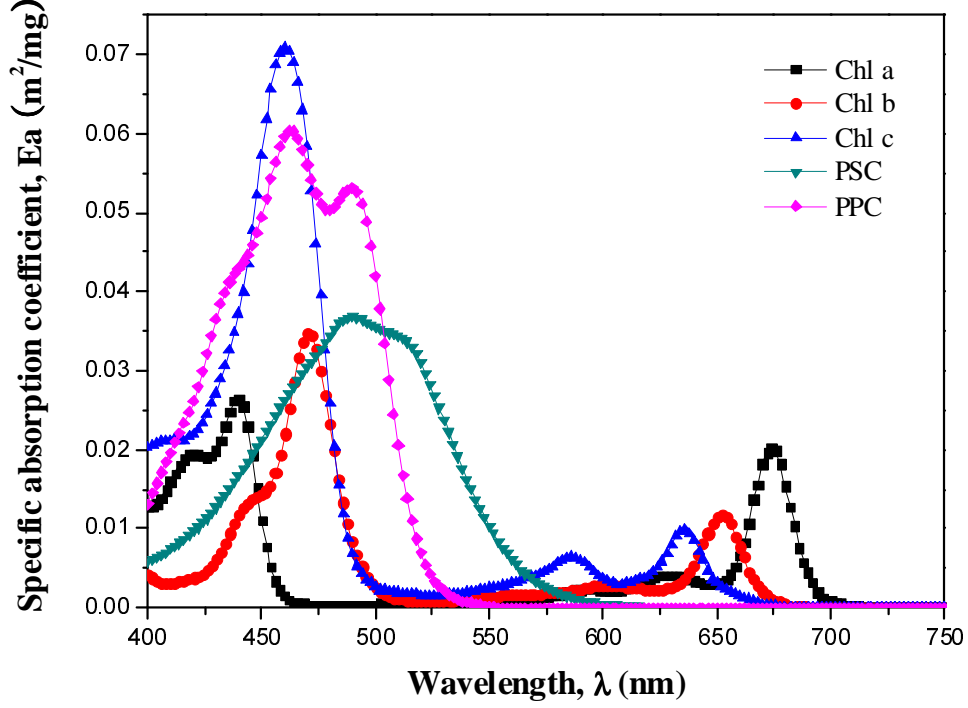


Figure 2.1: *In vivo* specific absorption coefficient Ea (in m^2/mg) of primary pigments chlorophylls a , b , and c and photosynthetic carotenoids (PSC), and photoprotective carotenoids (PPC) over the spectral region from 400 to 750 nm [4].

2.1 shows the *in vivo* specific absorption coefficient Ea (in m^2/mg) of primary pigments chlorophylls a , b , and c as well as accessory pigments such as photosynthetic carotenoids (PSC), and photoprotective carotenoids (PPC) measured over the spectral region from 400 to 750 nm [4]. It indicates that Chlorophyll a (Chl a) absorbs around 435 and 676 nm while Chlorophyll b (Chl b) absorbs around 475 and 650 nm. Since they do not absorb green light ($\lambda \approx 520\text{-}570$ nm) significantly, these microalgae appear green to the human eye. On the other hand, carotenoids are accessory pigments found in all photosynthetic microorganisms. They absorb mainly in the blue part of the spectrum ($400 \text{ nm} \leq \lambda \leq 550$ nm) [17]. Carotenoids serve two major functions (i) shielding the photosynthetic apparatus from photo-oxidation under large light intensities and (ii) increasing the solar light utilization efficiency by expanding the absorption spectrum of the microorganism.

The intracellular pigments such as chlorophylls and carotenoids are typically extracted by using organic solvents which penetrates through the cell membrane and dissolves the lipids to extract pigments [42, 43]. Methanol, acetone, and ethanol are usually used as the organic solvents in the pigments extraction process [44, 45].

2.2 Radiation Transfer Through Microalgae Suspensions

To design photobioreactors with more efficient light utilization, it is necessary to be able to predict the light distribution within PBRs. Light transfer in a homogeneous absorbing, scattering, and non-emitting suspension is governed by the radiative transfer equation (RTE) written as [46]

$$\hat{\mathbf{s}} \cdot \nabla I_\lambda(\mathbf{r}, \hat{\mathbf{s}}) = -\kappa_\lambda I_\lambda(\mathbf{r}, \hat{\mathbf{s}}) - \sigma_{s\lambda} I_\lambda(\mathbf{r}, \hat{\mathbf{s}}) + \frac{\sigma_{s\lambda}}{4\pi} \int_{4\pi} I_\lambda(\mathbf{r}, \hat{\mathbf{s}}) \Phi_\lambda(\hat{\mathbf{s}}_i, \hat{\mathbf{s}}) d\Omega_i \quad (2.1)$$

where I_λ is the spectral radiation intensity about the direction $\hat{\mathbf{s}}$ at location \mathbf{r} in $\text{W}/\text{m}^2 \cdot \text{sr} \cdot \text{nm}$, κ_λ (m^{-1}) is the spectral absorption coefficient, $\sigma_{s\lambda}$ (m^{-1}) is the spectral scattering coefficient, $\Phi_\lambda(\hat{\mathbf{s}}_i, \hat{\mathbf{s}})$ represents the scattering phase function which is the probability that radiation propagating in the solid angle $d\Omega_i$ direction around $\hat{\mathbf{s}}_i$ is scattered into the solid angle $d\Omega$ along the direction $\hat{\mathbf{s}}$ and is normalized such that

$$\frac{1}{4\pi} \int_{4\pi} \Phi_\lambda(\hat{\mathbf{s}}_i, \hat{\mathbf{s}}) d\Omega_i = 1 \quad (2.2)$$

The first and second term on the right-hand side of Equation (2.1) represents the attenuation by absorption and out-scattering respectively while the last term corresponds to the augmentation of radiation due to in-scattering. In addition, β_λ ($=\sigma_{s\lambda} + \kappa_\lambda$) is the so-called spectral extinction coefficient. The Henyey-Greenstein asymmetry factor is defined as [2]

$$g_\lambda = \frac{1}{4\pi} \int_{4\pi} \Phi_\lambda(\theta) \cos\theta d\theta \quad (2.3)$$

For an isotropically scattering medium g_λ is equal to zero while it approaches unity for strongly forward scattering media. The effective absorption coefficient κ_λ of a microorganism

suspension with a size distribution can be related to the absorption cross-section as [46]

$$\kappa_\lambda = \int_0^\infty C_{abs,\lambda}(d_s)N(d_s)dd_s = \bar{C}_{abs,\lambda}N_T \quad (2.4)$$

where $C_{abs,\lambda}(d_s)$ is the effective absorption cross-section (in m^2) of a single scatterer of diameter d_s while $N(d_s)$ is the number of cells per unit volume of suspension having diameter between d_s and $d_s + dd_s$. The average absorption cross-section is $\bar{C}_{abs,\lambda}$ (in m^2). Similarly, the scattering coefficient of the microorganism suspension can be expressed as [47],

$$\sigma_{s,\lambda} = \int_0^\infty C_{sca,\lambda}(d_s)N(d_s)dd_s = \bar{C}_{sca,\lambda}N_T \quad (2.5)$$

where $C_{sca,\lambda}(d_s)$ is the effective scattering cross-section (in m^2) of a single scatterer and $\bar{C}_{sca,\lambda}$ is the average scattering cross-section (in m^2). The cell density is denoted by N_T and defined as the total number of cells per m^3 of suspension. The average absorption and scattering coefficients can also be expressed in average mass absorption $\bar{A}_{abs,\lambda}$ and scattering $\bar{S}_{sca,\lambda}$ cross-sections (in m^2/kg) respectively as [48]

$$\bar{A}_{abs,\lambda} = \kappa_\lambda/X \quad \text{and} \quad \bar{S}_{sca,\lambda} = \sigma_{s,\lambda}/X \quad (2.6)$$

where X is the microorganism mass concentration expressed in kilogram of dry cell weight per cubic meter of liquid medium. The average absorption and scattering cross-sections $\bar{C}_{abs,\lambda}$ and $\bar{C}_{sca,\lambda}$ are related to the average mass absorption and scattering cross-sections $\bar{A}_{abs,\lambda}$ and $\bar{S}_{sca,\lambda}$ according to [49],

$$\bar{C}_{abs,\lambda} = \bar{A}_{abs,\lambda}V_{32}\rho_{dm}(1 - x_w) \quad \text{and} \quad \bar{C}_{sca,\lambda} = \bar{S}_{sca,\lambda}V_{32}\rho_{dm}(1 - x_w) \quad (2.7)$$

where ρ_{dm} is the dry mass density of microorganism in kg/m^3 , V_{32} is the mean particle volume in m^3 , and x_w is the volume fraction of water in the cell.

Pottier *et al.* [49] derived an analytical solution to the RTE using the generalized two-flux approximation considering one-dimensional light transfer through a well-mixed algal suspension in a vertical flat-plate PBR of thickness L . The front window ($z = 0$) was assumed

to be transparent and exposed to irradiance $G_{in,\lambda}$ incident at an angle θ_c with respect to the direction normal to the PBR window. The back surface ($z = L$) was diffusely reflecting with reflectance ρ_λ . The local spectral fluence rate $G_\lambda(z)$ in the PBR, corresponding to the total intensity impinging at location z from all directions, i.e., $G_\lambda(\mathbf{r}) = \int_{4\pi} I_\lambda(\hat{\mathbf{s}}, \mathbf{r}) d\Omega$, was expressed as [49]

$$\frac{G_\lambda(z)}{G_{in,\lambda}} = 2\sec\theta_c \frac{[\rho_\lambda(1 + \alpha_\lambda)e^{-\delta_\lambda L} - (1 - \alpha_\lambda)e^{-\delta_\lambda L}]e^{\delta_\lambda z} + [(1 + \alpha_\lambda)e^{\delta_\lambda L} - \rho_\lambda(1 - \alpha_\lambda)e^{\delta_\lambda L}]e^{-\delta_\lambda z}}{(1 + \alpha_\lambda)^2 e^{\delta_\lambda L} - (1 - \alpha_\lambda)^2 e^{-\delta_\lambda L} - \rho_\lambda(1 - \alpha_\lambda^2)e^{\delta_\lambda L} + \rho_\lambda(1 - \alpha_\lambda^2)e^{-\delta_\lambda L}} \quad (2.8)$$

where α_λ and δ_λ are expressed as [49]

$$\alpha_\lambda = \sqrt{\frac{\bar{C}_{abs,\lambda}}{\bar{C}_{abs,\lambda} + 2b_\lambda \bar{C}_{sca,\lambda}}} \quad \delta_\lambda = N_T \sec\theta_c \sqrt{\bar{C}_{abs,\lambda}(\bar{C}_{abs,\lambda} + 2b_\lambda \bar{C}_{sca,\lambda})} \quad (2.9)$$

The backward scattering ratio b_λ for an axisymmetric phase function is defined as [49]

$$b_\lambda = \frac{1}{2} \int_{\pi/2}^{\pi} \Phi_{T,\lambda}(\theta) \sin\theta d\theta \quad (2.10)$$

where θ is the scattering angle between directions $\hat{\mathbf{s}}_i$ and $\hat{\mathbf{s}}$.

The average fluence rate G_{ave} can be defined as the volume- and PAR-averaged local fluence rate $G_\lambda(z)$ per unit surface area of PBR expressed as [2]

$$G_{ave} = \frac{1}{L} \int_{400}^{700} \int_0^L G_\lambda(z) dz d\lambda \quad (2.11)$$

The average radiant power absorbed per cell present in the PBR over the PAR region denoted by, A_{ave} (in $\mu\text{mol/s/cell}$) was defined as [50]

$$A_{ave} = \frac{1}{L} \int_0^L \int_{400}^{700} \bar{C}_{abs,\lambda} G_\lambda(z) d\lambda dz \quad (2.12)$$

This quantity (or $A_{ave}N_T$) enables the formulation of models coupling radiant light transfer and microalgae metabolism and growth kinetics in PBRs [50].

2.3 Radiation Characteristics of Microalgae

A large body of literature exists on predicting and measuring the absorption and scattering coefficients, efficiency factors, or cross-sections and the scattering phase function of microor-

ganism suspensions [2, 51–54].

2.3.1 Theoretical Prediction

Bidigare *et al.* [4] used a predictive approach to determine the absorption coefficient in various species of phytoplankton. The cell was modeled as a homogeneous particle in which only the pigments in the cell contributed to the absorption coefficient in the photosynthetically active radiation (PAR) region between 400 and 700 nm. Then, the absorption coefficient (in 1/m) was expressed as [55]

$$\kappa_\lambda = \sum_{i=1}^N Ea_i C_i \quad (2.13)$$

where Ea_i (in m^2/kg) is the *in vivo* specific spectral absorption coefficient of pigment i (Figure 2.1) and C_i are their mass concentrations (in kg/m^3).

Pottier *et al.* [49] adopted a simpler approach to retrieve the refraction and absorption indices of *C.reinhardtii*. They measured the normal hemispherical transmittance of a suspension of *C.reinhardtii* at 820 nm where they do not absorb. The corresponding refraction index was found to be 1.527 and assumed to be constant over the PAR. Then, the authors estimated the spectral absorption index k_λ according to [49]

$$k_\lambda = \frac{\kappa_\lambda \lambda}{4\pi} = \frac{\lambda}{4\pi} \rho_{dm} \frac{1 - x_w}{x_w} \sum_{i=1}^N Ea_i w_i \quad (2.14)$$

where pigment mass fractions w_i were estimated experimentally.

Moreover, Quirantes and Bernard [56] modeled algal cells as two-layer particles with an inner core and an external coating. The coating was assumed to be non-absorbing and had a refraction index of 1.36 representing cellular cytoplasm. The inner core, representing the organelles and chloroplasts, was absorbing and featured a larger refraction index than the outer coating representing. Its value was selected such that the volume-averaged complex index of refraction of the composite particle was equal to that of an equivalent homogeneous scatterer with complex index of refraction of $1.40 + i0.005$, considered to be typical of algal cells [57–59]. First, the extinction and absorption efficiency factors of homogeneous spheres

and coated spheres were calculated using the Aden-Kerker theory [60] and the modified anomalous diffraction approximation (ADA) [61], respectively. The heterogeneous geometry of the coated spheres was found to increase the back-scattering efficiency by a factor as high as 50 but had negligible effects on the absorption efficiency factor and weak effects on the scattering efficiency factor when compared with those of a homogeneous sphere with the same complex index of refraction. These results were consistent with previous studies using volume-averaged equivalent complex indices of refraction to compare homogeneous and heterogeneous multi-layered spheres [62, 63]. In addition, Quirantes and Bernard [56] considered three different geometries with the same size parameter and equivalent complex refractive index namely (i) off-centered coated spheres, (ii) concentric spheroids, and (iii) concentric spheres. The T-matrix method [64] was used to compute the efficiency factors of the aspherical and non-concentric composite cells. The absorption and scattering efficiency factors showed little dependency on particle shape. These results suggest that heterogeneous microorganism cells can be treated as homogeneous with some effective complex index of refraction. This approach has been widely used in the ocean optics community [51, 54].

2.3.2 Experimental Measurements

Recently, Berberoğlu and co-workers [48, 65] experimentally measured the radiation characteristics of several H_2 producing microorganisms namely (a) purple non-sulfur bacteria *R.sphaeroides* [48], (b) cyanobacteria *A.variabilis* [48], and (c) green algae *Chlamydomonas reinhardtii* strain CC125 and its truncated chlorophyll antenna transformants *tla1*, *tlaX*, and *tla1-CW⁺* [65]. The authors also measured the radiation characteristics of the lipid producing microalgae *C. littorale*, *B. braunii*, and *Chlorella sp.* [5]. Except for the purple bacteria *R.sphaeroides* which absorbs in the near infrared, the absorption coefficients of these microorganisms vanish beyond 750 nm when only scattering contributes to extinction. For example, the wild strain *C.reinhardtii* CC125 absorbs mainly in the spectral region from 300 to 700 nm with absorption peaks at 435 and 676 nm corresponding to absorption peaks of *in vivo* chlorophyll *a*. It also has additional absorption peaks at 475 and 650 nm corresponding

to absorption by chlorophyll *b*. Berberoğlu *et al.* [65] also showed that the genetically engineered strains of *C.reinhardtii* have less chlorophyll pigments than the wild strain and thus have smaller absorption cross-sections. In particular, the mutant *tlaX* featured a significant reduction in chlorophyll *b* concentration. For all mutants, the reduction in their absorption cross-section was accompanied by an increase in their scattering cross-section.

2.4 Effective Optical Properties of Microorganisms

Assuming the microorganism cells to be homogeneous, one can define their effective complex index of refraction as $m_\lambda = n_\lambda + ik_\lambda$ where n_λ and k_λ are the effective refraction and absorption indices, respectively. Their refraction index n_λ can be measured directly using photometric immersion refractometry and flow cytometry [57, 66–70]. However, these experimental measurements are complicated by the polydispersion of the cells and by light absorption. On the other hand and to the best of my knowledge, no method has been reported in the literature to directly measure the absorption index k_λ of microbial particles in suspension.

2.4.1 Direct Experimental Measurements

First, photometric immersion refractometry consists of suspending the cells in a medium of known refraction index and measuring the transmittance T_λ or the optical density (OD) of the suspension defined as $OD_\lambda = -\log T_\lambda$ [66, 67] at a non-absorbing wavelength. For example an aqueous solution of bovine serum albumin (BSA) can be used as the immersion medium as it is not toxic to microorganisms. Solutions with different refraction indices can be prepared by varying the BSA concentration [71]. The OD of the suspension is then measured as a function of BSA concentration. The refraction index of the microbial cells at the wavelength considered is taken as that of the BSA solution corresponding to the minimum OD.

Flow cytometry can also be used to directly measure the refraction index n_λ of microalgae [69, 70]. Collimated laser radiation is directed at a stream of saline solution containing

microbial particles. The latter are assumed to be homogeneous spheres despite their potentially irregular morphologies. The intensities of forward scattered light (typically at an angle of 1-19° with respect to the incident beam direction), side scattered light (54-126°), and chlorophyll fluorescence (660-700 nm) are measured [69]. The system is calibrated using standard suspensions consisting of polydisperse spherical particles of known refraction index such as oil globules and glass beads. For every individual cell, different intensities of the forward and side scattered light are measured depending on their size, shape, and refraction index. The refraction index is found by fitting the experimental measurements and comparing with standards suspensions.

Finally, the abundance of refraction index data for various species of phytoplankton has been used to correlate the refraction index n_λ to the intracellular carbon concentration in the form [54]

$$n_\lambda = n_{0,\lambda} + n_{1,\lambda}C_c \quad (2.15)$$

where $n_{0,\lambda}$ and $n_{1,\lambda}$ are constants determined by experimental procedures and C_c is the intracellular carbon concentration (in kg/m³). For example, DuRand and Olson [72] reported $n_{0,\lambda} = 1.02$ and $n_{1,\lambda} = 0.000117$ for *Nannochloris sp.* at 665 nm. Unfortunately, most of the above methods measured the refraction index at a single wavelength. It then has to be assumed constant over the PAR for spectral calculations of light transfer in the suspension and estimation of the average fluence rate available in PBRs and necessary in growth kinetic models [49, 54, 73, 74].

2.4.2 Model-Based Measurements

Despite their heterogeneous morphologies, microalgae have typically been treated as homogeneous with some effective refraction and absorption indices. Stramski and Mobley [51] experimentally measured the size distributions of various marine microbial particles and their spectral radiation characteristics in the PAR region (400 to 700 nm). The experimental data were used as input to an inverse method developed by Bricaud and Morel [57] to

predict the complex refractive index of the particles under the assumptions that the particles were homogeneous and spherical. First, the absorption index was determined based on the anomalous diffraction approximation describing the absorption coefficient as a monotonic function of the absorption thickness parameter defined as $p' = 4\chi k_\lambda$ [61, 75] where k_λ is the absorption index of the particle and $\chi = \pi d_s n_2 / \lambda$ is the size parameter previously defined. For any given wavelength and particle size distribution, the absorption index was uniquely related to the absorption coefficient. Thus, for a given wavelength, the absorption index k_λ was varied iteratively until the calculated absorption coefficient matched its experimental value. Calculations were repeated for each wavelength to obtain the spectral absorption index. On the other hand, the refraction index n_λ was derived through an inverse method described by Stramski *et al.* [76]. Here, the Lorentz-Mie theory [60] was used instead of the anomalous diffraction approximation. The experimental data and the previously retrieved absorption indices were used as input parameters into the Lorentz-Mie theory code [60]. The refraction index was varied iteratively until the calculated extinction coefficient matched its experimental value. It was found that the measured microbial particles had absorption index ranging between 0 and 0.01 and refraction index between 1.38 and 1.42. The refraction index was found to vary by less than 5% in the PAR region for all microorganism species considered.

2.5 Tasks

The present study aims to measure and/or predict radiation characteristics of photosynthetic microorganisms. The following describes the tasks taken to achieve this objective.

Task 1. **Experimental measurements of radiation characteristics of photosynthetic microorganisms**

In order to effectively model light transfer in photobioreactors, the spectral radiation characteristics of photosynthetic microorganisms are necessary inputs to the radiative transfer equation (RTE). This study presents experimental measurements of the

absorption and scattering cross-sections and scattering phase functions of several photosynthetic microorganisms of different morphologies. Furthermore, it illustrates the direct connection between the cross-sections and the concentrations of cellular pigments. Finally, it assesses the dependence of these cross-sections on the microorganisms growth conditions.

Task 2. **Retrieving the effective spectral complex index of refraction of photosynthetic microorganisms**

Obtaining the radiation characteristics of photosynthetic microorganisms through experimental measurements may not always be feasible due to the high cost in equipment and time involved. Alternatively, these radiation characteristics can be predicted if the spectral complex index of refraction and size distribution are known. This study developed different equivalent scattering particles that can approximate the various morphologies of biofuel producing photosynthetic microorganisms. Based on these approximations, inverse methods were implemented to retrieve the spectral complex index of refraction from experimental measurements of photosynthetic microorganisms.

2.6 Organization of this document

Chapter 3 presents the spectral optical properties of several unicellular spheroidal microalgae. Chapter 4 presents the temporal evolution of the scattering and absorbing cross-sections of *Nannochloropsis oculata* in response to light and nitrogen availability. Chapter 5 presents the radiation characteristics and optical properties of filamentous cyanobacterium *Anabaena cylindrica*. Chapter 6 establishes an approximate method of predicting the radiation characteristics of microorganisms resembling bispheres, quadspheres, and rings of spheres. Chapter 7 presents the radiation characteristics and optical properties of dumbbell-shaped cyanobacterium *Synechocystis sp.*. Finally, Chapter 8 summarizes the main contributions of the present study.

CHAPTER 3

Spectral optical properties of selected photosynthetic microalgae producing biofuels

This chapter presents the spectral complex index of refraction of *Botryococcus braunii*, *Chlorella sp.*, and *Chlorococcum littorale* between 400 and 750 nm. These results were retrieved from experimentally measured average absorption and scattering cross-sections. The unicellular green algae cells were treated as homogeneous polydisperse spheres with equivalent diameter such that their surface area was identical to that of their approximated spheroidal shape. The inverse method used in the retrieval process was developed by combining Lorentz-Mie theory as the forward method and genetic algorithm. The method and/or the reported optical properties can be used in various applications from ocean remote sensing, carbon cycle study, as well as photobiological carbon dioxide mitigation and biofuel production.

3.1 Introduction

Solar radiation is the energy source driving the metabolic activity of photosynthetic microorganisms. As light penetrates in the photobioreactor, it is absorbed and scattered by the microorganisms. Light transfer in photobioreactors is governed by the radiative transfer equation (RTE). The latter is an energy balance on the radiative energy traveling along a particular direction \hat{s} . The absorption and scattering coefficients of microalgae together with the scattering phase function are major parameters needed to solve the RTE for simulating, designing, scaling-up, optimizing, and controlling photobioreactors [77]. These characteris-

tics are strongly dependent on wavelength and vary from one species to another. They can be determined either experimentally [48, 65] or theoretically based on electromagnetic wave theory [49]. Theoretical predictions often assume that the scatterers have relatively simple shape (e.g., spherical) and ignore their heterogeneous nature by attributing them a uniform effective complex index of refraction. Pottier *et al.* [49] recognized that for complex microorganisms shapes (e.g., cylinders and spheroids), advanced numerical tools are required to predict their absorption and scattering coefficients and scattering phase function collectively called radiation characteristics. On the other hand, experimental measurements account for the actual shape, morphology, and size distribution of the microorganisms. However, experimental setups can be expensive and measurements are time consuming.

In order to design, optimize, and operate photobioreactors for CO₂ fixation and biofuel production, it would be convenient to have the ability to predict the radiation characteristics of microalgae from first principles instead of carrying out costly and time consuming experiments. If the effective spectral real and imaginary parts of the complex index of refraction as well as the microorganisms shape and size distribution are known to within an acceptable level of uncertainties, the absorption and scattering coefficients can be predicted by Lorentz-Mie theory [78], if the microalgae are spherical, or by the T-matrix method [79], if the particles have more complex shapes.

The present study aims to retrieve the spectral real (refraction index) and imaginary (absorption index) parts of the complex index of refraction of microalgae from experimentally measured size distribution as well as absorption and scattering cross-sections [5, 65].

3.1.1 *B. braunii*, *Chlorella sp.*, *C. littorale*

The different microalgae species investigated were selected for different reasons. *B. braunii* grows in freshwater and was chosen for its high lipid content which can be converted into liquid biofuels [80–83]. On the other hand, *Chlorella sp.* is a unicellular green algae with high oil content and fast growth rate under large CO₂ concentrations [83–85]. *C. littorale* is

also of interest because it is a marine microalgae that can tolerate high CO₂ concentrations and can grow to very large cell density [86, 87].

3.2 Analysis

3.2.1 Assumptions

In the present study, the different microalgae were assumed to be spherical. This assumption simplifies the calculations of their radiation characteristics by using the Lorentz-Mie theory instead of the T-matrix method and its validity for the microalgae of interest will be discussed later. Moreover, despite their heterogeneous structure, microalgae were treated as homogeneous with some effective refraction and absorption indices. Note that n_λ was treated as wavelength-dependent over the PAR region, unlike what previous studies have often assumed [49].

3.2.2 Equivalent diameter and size distribution

The different microalgae were treated as homogeneous spheres with an equivalent diameter such that their surface area was identical to that of their actual spheroidal shape assumed to be axisymmetric [56, 88, 89]. The polar radius of an axisymmetric spheroid in the spherical coordinate system is given by [90]

$$r(\theta) = \frac{a}{2} \left(\sin^2\theta + \frac{a^2}{b^2} \cos^2\theta \right)^{-1/2} \quad (3.1)$$

where θ is the polar angle, while a and b are the major and minor diameters, respectively. The spheroid aspect ratio is defined as $\epsilon = a/b$. Note that ϵ is always greater than 1.0 since a is the major diameter [90]. The equivalent diameter of the sphere having the same surface area as the spheroid is given by [90]

$$d_s = \frac{1}{2} \left(2a^2 + 2ab \frac{\sin^{-1}e}{e} \right)^{1/2} \quad \text{where} \quad e = \frac{(\epsilon^2 - 1)^{1/2}}{\epsilon} \quad (3.2)$$

Moreover, the number frequency of equivalent diameter d_s denoted by $f(d_s)$ is defined

as,

$$f(d_s) = \frac{N(d_s)}{\int_o^{\infty} N(d_s) dd_s} = \frac{N(d_s)}{N_T} \quad (3.3)$$

where $N(d_s)$ is the number of cells per unit volume of suspension having diameter between d_s and $d_s + dd_s$. The denominator on the right-hand side of Equation (3.3) is the total cell concentration N_T expressed in total number of cells per m^3 of suspension.

Berberoglu *et al.* [5] reported the size distribution for the minor and major diameters $N(a)$ and $N(b)$ for *B. braunii*, *Chlorella sp.*, and *C. littorale*. Their average circularity is defined as $c = 4\pi \times A_S/P^2$ where A_S and P are the cell's surface area and perimeter. The authors used the image analysis software ImageJ [91] to measure their minor and major diameters assuming the cells to be 2D ellipses. Then, the surface area and perimeter of axisymmetric spheroids were calculated as $A_S = \pi ab/4$ and $P = 2\pi\sqrt{2(a^2 + b^2)}$, respectively. The circularity for *B. braunii*, *Chlorella sp.*, and *C. littorale* was equal to 0.961, 0.965, and 0.975 while their average aspect ratio ϵ was 1.333, 1.301, and 1.212, respectively.

Finally, Figure 3.1 shows the number frequency $f(d_s)$ of the equivalent diameter d_s for *B. braunii*, *Chlorella sp.*, and *C. littorale*. It was calculated from experimentally measured major and minor diameters using Equation (3.2). Depending on the species, the number of bins was 60 or 70 with d_s between 2 and 20 μm .

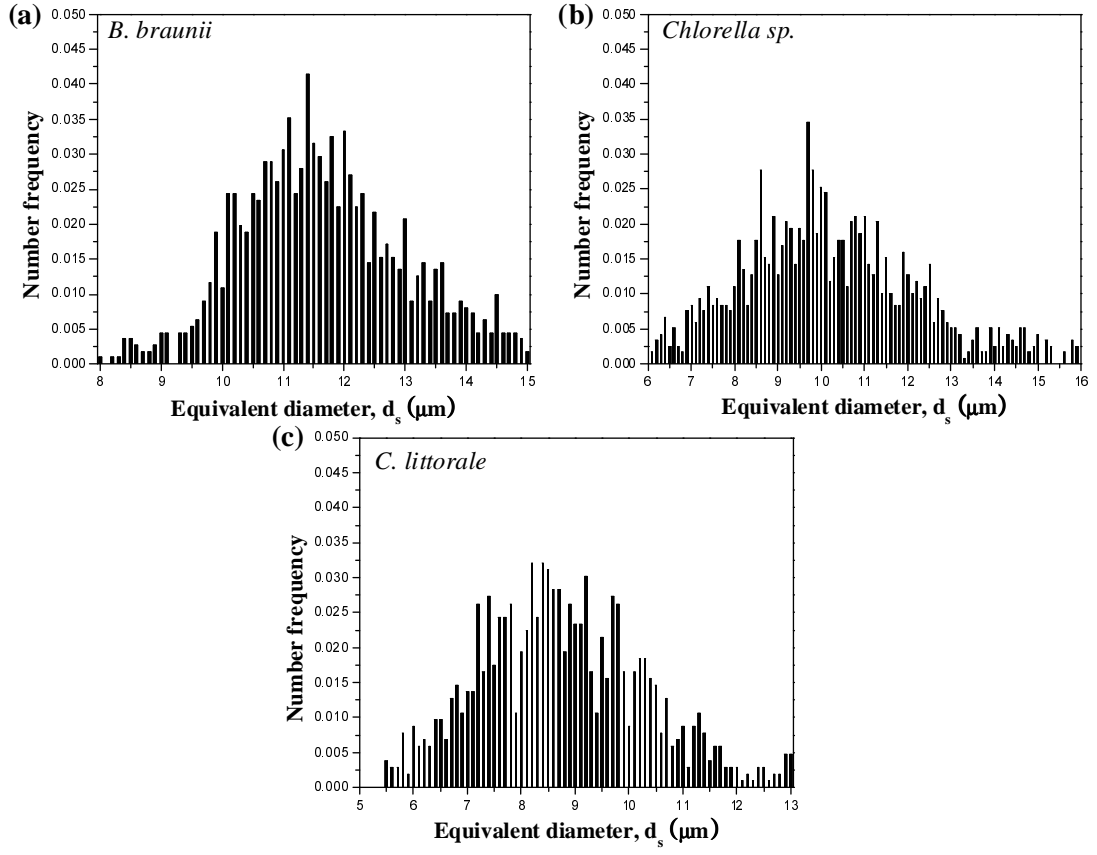


Figure 3.1: Number frequency $f(d_s)$ of the equivalent sphere diameter of (a) *B. braunii* ($c=0.961$, $\epsilon=1.333$), (b) *Chlorella sp.* ($c=0.965$, $\epsilon=1.301$), and (c) *C. littorale* ($c=0.975$, $\epsilon=1.212$). The equivalent diameter was estimated from Equation (3.2) and major and minor diameter distributions reported in Figure 2 in Ref. [5].

3.2.3 Prediction of the Radiation Characteristics of Microalgae

The Lorentz-Mie theory predicts the absorption and scattering cross-sections denoted by $C_{abs,\lambda}(d_s)$ and $C_{sca,\lambda}(d_s)$ (expressed in m^2) of an individual spherical cell of diameter d_s with complex index of refraction $n_\lambda + ik_\lambda$ submerged in phosphate buffered saline (PBS) solution with refraction index n_{PBS} . Then, the absorption coefficient κ_λ of a microorganism suspension with size distribution $N(d_s)$ is expressed as [92],

$$\kappa_\lambda = \int_0^\infty C_{abs,\lambda}(d_s)N(d_s)dd_s = \bar{C}_{abs,\lambda}N_T \quad (3.4)$$

Similarly, the effective scattering coefficient of the microorganisms $\sigma_{s,\lambda}$ can be written as [47],

$$\sigma_{s,\lambda} = \int_0^\infty C_{sca,\lambda}(d_s)N(d_s)dd_s = \bar{C}_{sca,\lambda}N_T \quad (3.5)$$

Here, $\bar{C}_{abs,\lambda}$ and $\bar{C}_{sca,\lambda}$ are the average absorption and scattering cross-sections of the microalgae in suspension (in m^2), respectively. These average cross-sections can effectively be measured for typically polydisperse microalgae population. In fact, Berberoğlu *et al.* [5] measured the average absorption and scattering cross-sections $\bar{C}_{abs,\lambda}$ and $\bar{C}_{sca,\lambda}$ for *B. braunii*, *Chlorella sp.*, and *C. littorale*. Thus, the predictions from Lorentz-Mie theory and Equations (3.4) and (3.5) could be directly compared with experimental data.

3.2.4 Optimization Algorithm

Figure 3.2 shows the schematic diagram of the procedure used to simultaneously retrieve the spectral refraction index n_λ and the absorption index k_λ that was developed by Lee *et al.* [93]. The Lorentz-Mie theory [78] was employed in the forward model to calculate the spectral average absorption and scattering cross-sections $\bar{C}_{abs,\lambda}$ and $\bar{C}_{sca,\lambda}$ over the PAR.

Various optimization algorithms can be used to efficiently and simultaneously determine n_λ and k_λ . The objective is to find the values of these parameters that minimize the difference between the predicted and experimentally measured absorption and scattering cross-sections of the microalgal suspension in the least-square sense. Genetic algorithm can find a global

minimum of an objective function using the concept of evolution theory [94]. A given set of input parameters [e.g., (n_λ, k_λ)] is called an individual and each parameter is called a gene. The numerical procedure starts with a randomly generated population consisting of numerous individuals. The objective function (or fitness function) is calculated for each individual of the population and estimates some difference between experimental measurements and model predictions. Individuals with the largest value of the objective function are dismissed. Those with the smallest objective function are selected to form a new population. Breeding of the new generation consists of producing new individuals by recombination and random mutation of the genes of an arbitrary pair of individuals. The fitness function is evaluated for each individual and the procedure is repeated generation after generation until the objective function falls below a given convergence criterion. This method tends to be slow but it is robust and eventually converges to the global minimum [95].

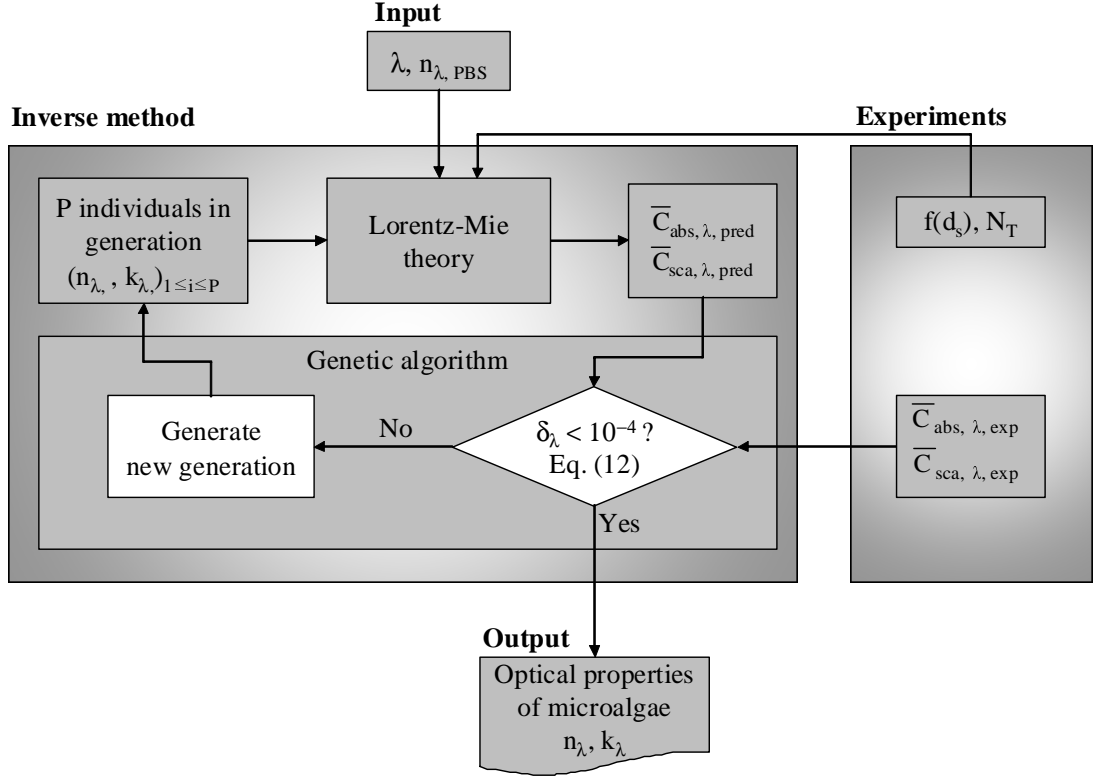


Figure 3.2: Block diagram of the procedure used to retrieve the refractive index n_λ and absorption index k_λ from the absorption and scattering cross-sections $\bar{C}_{abs,\lambda}$ and $\bar{C}_{sca,\lambda}$ at a given wavelength λ for number frequency $f(d_s)$. We used $N=120$ individuals per generation for a maximum of 50 generations. n_λ and k_λ were allowed to range from 1.33 to 1.53 and from 10^{-5} to 0.01, respectively.

In the present study, genetic algorithm was implemented using the general purpose function optimization code PIKAIA [96–98]. Here, the spectral refractive index n_λ was assumed to range from 1.33 to 1.53 based on the literature [49,99]. On the other hand, the absorption index k_λ was allowed to range from 10^{-5} to 0.01. For each wavelength, the objective function δ_λ was defined as,

$$\delta_\lambda = \left(\frac{\bar{C}_{abs,\lambda,pred} - \bar{C}_{abs,\lambda,exp}}{\bar{C}_{abs,\lambda,exp}} \right)^2 + \left(\frac{\bar{C}_{sca,\lambda,pred} - \bar{C}_{sca,\lambda,exp}}{\bar{C}_{sca,\lambda,exp}} \right)^2 \quad (3.6)$$

The genetic algorithm used a maximum of 50 generations with population of $P=120$ indi-

viduals. The convergence criteria was set as $\delta_\lambda < 10^{-4}$.

3.2.5 Experimental Uncertainties

Experimentally, the absorption and scattering cross-sections for each species were measured for three different microalgae concentrations. The maximum experimental uncertainties, with 95% interval confidence, associated with the absorption and scattering cross-sections for *B. braunii*, *Chlorella sp.*, and *C. littorale* were 21%, 15%, and 15%, respectively. These experimental uncertainties propagated in the retrieved values of n_λ and k_λ . Thus, for all species, n_λ and k_λ were retrieved at wavelengths 435 and 676 nm, corresponding to Chl *a* absorption peaks, from the cross-sections $\bar{C}_{abs,\lambda} \pm \Delta\bar{C}_{abs,\lambda}$ and $\bar{C}_{sca,\lambda} \pm \Delta\bar{C}_{sca,\lambda}$ where $\Delta\bar{C}_{abs,\lambda}$ and $\Delta\bar{C}_{sca,\lambda}$ were equal to two standard deviations.

3.3 Results and Discussions

3.3.1 Validation: Retrieving n_λ and d_s of Monodisperse Latex Particles

Berberoglu *et al.* [65] measured the scattering cross-section, between 400 and 800 nm, of monodisperse polystyrene latex spheres 5 μm in diameter in suspension in PBS solution. They used the same experimental procedure and analysis as that used to measure the radiation characteristics of the different microalgae considered in the present study. For validation purposes, the previously described inverse procedure and associated algorithm were used to retrieve the spectral refraction index as well as the diameter of spherical polystyrene latex particles using the measured scattering cross-section [65].

First, the absorption index of PBS in the visible was reported to be that of water [100] which is less than 4.0×10^{-8} [101]. The absorption index of polystyrene was reported to be less than 5.0×10^{-3} [102] between 400 and 700 nm. Thus, in the present study, the absorption index of both polystyrene and PBS were taken as $k = 0.0$ used as input parameters in the Lorentz-Mie theory. On the other hand, the refraction index of both PBS and polystyrene

were modeled by the Cauchy dispersion relation expressed as [103]

$$n_\lambda = A + \frac{B}{\lambda^2} + \frac{C}{\lambda^4} \quad (3.7)$$

For PBS, the parameters A_{PBS} , B_{PBS} , and C_{PBS} were taken as $A_{PBS} = 1.32711$, $B_{PBS} = 2.6 \times 10^{-3} \mu\text{m}^2$, and $C_{PBS} = 5.0 \times 10^{-5} \mu\text{m}^4$ when λ was expressed in μm [100]. Then, our inverse method simultaneously retrieved the particle diameter d_s and the parameters A , B , and C using the objective function

$$\delta_\lambda = \sum_{i=1}^9 \left(\frac{\bar{C}_{sca,\lambda_i,pred} - \bar{C}_{sca,\lambda_i,exp}}{\bar{C}_{sca,\lambda_i,exp}} \right)^2 \quad (3.8)$$

where the nine wavelengths λ_i were uniformly distributed between 400 and 700 nm. The parameters were found to be respectively $d_s = 5.01 \mu\text{m}$, $A = 1.5555$, $B = 3.911 \times 10^{-3} \mu\text{m}^2$, and $C = 3.867 \times 10^{-4} \mu\text{m}^4$. First, the polystyrene sphere diameter was retrieved very accurately. The values of parameters A , B , and C should be compared with those reported by Ma *et al.* [102] as $A = 1.5725$, $B = 3.108 \times 10^{-3} \mu\text{m}^2$, and $C = 3.4779 \times 10^{-4}$. Comparison (not shown) of the refraction index of polystyrene retrieved here and that reported by Ma *et al.* [102] indicated that the relative error was less than 1.2% for all wavelengths between 400 and 800 nm. This is in excellent agreement and confirms the validity of the methodology and the proper implementation of the genetic algorithm.

3.3.2 Retrieved Spectral Complex Index of Refraction of Microalgae

This section presents the retrieved effective refraction and absorption indices of *B. braunii*, *Chlorella sp.*, and *C. littorale* between 400 to 750 nm.

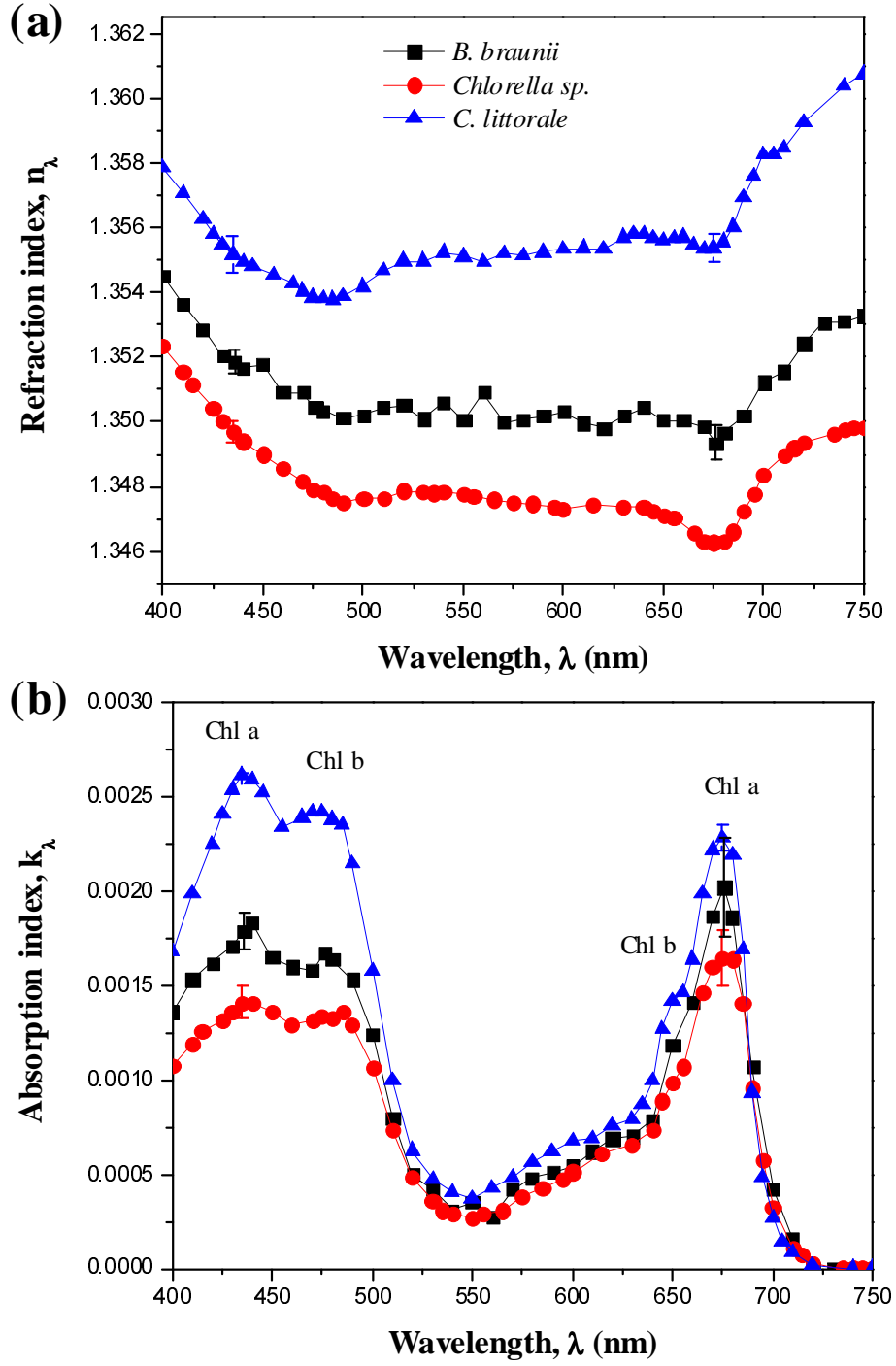


Figure 3.3: Comparison of the retrieved refractive and absorption indices between 400 and 750 nm for *B. braunii*, *Chlorella sp.*, and *C. littorale* using their number frequency $f(d_s)$.

Figures 3.3(a) shows the retrieved effective refraction and absorption indices for *B. braunii*, *Chlorella sp.*, and *C. littorale* between 400 and 750 nm from the measured absorption and scattering cross-sections. Their refraction index n_λ varied slightly between 1.345 and 1.36. Figure 3.3(a) indicates that *C. littorale* had the largest refraction index followed by *B. braunii* and *Chlorella sp.* This can be attributed to differences in their composition and in particular their carbohydrates and proteins content. Indeed, Aas [104] derived the refraction index of a phytoplankton cells from their metabolite composition by treating them as a “mixture” of various constituents. The author reported the refraction index of the major cell constituents including carbohydrates and proteins which have the largest refraction index in the PAR equal to 1.55 and 1.53, respectively. In addition, the dry mass fractions of carbohydrates and proteins were reported to be (a) 25% and 53% for *C. littorale* [87], (b) 17% and 32% for *B. braunii* [105], and (c) 19% and 6% for *Chlorella sp.* [106]. Assuming that the water volume fraction was similar for all three species, *C. littorale* feature the largest concentrations of carbohydrates and proteins followed by *B. braunii* and lastly *Chlorella sp.* The differences in these reported carbohydrates and proteins mass fractions could explain the differences observed in the retrieved refraction indices of these species.

Figure 3.3(b) indicates that *C. littorale* had the largest absorption index k_λ while *B. braunii* and *Chlorella sp.* featured similar absorption indices across the PAR. Here also, k_λ features absorption peaks at 435, 475, and 676 nm corresponding to the absorption peaks of *in vivo* Chl *a* and Chl *b*. It is interesting to note that the absorption cross-section of *B. braunii* was larger than those of *C. littorale* and *Chlorella sp.* which were similar [5] despite the fact that *C. littorale* were much smaller than *B. braunii*, and *Chlorella sp.* However, the dry mass fraction of Chl *a+b* was (a) 1.9% in *C. littorale* [87], (b) 0.22-0.56% in *B. braunii* [107], and (c) 0.4-1.41% in *Chlorella sp.* [106]. This may explain why *C. littorale* had the largest absorption index k_λ and *B. braunii* and *Chlorella sp.* were found to have similar k_λ .

The average relative and maximum errors between experimental measurements and Lorentz-Mie theory predictions using the reported values for n_λ and k_λ were respectively (i) 0.4%

and 3% for the absorption cross-sections and (ii) less than 0.5% and 2% for the scattering cross-sections of *B. braunii*, *Chlorella sp.*, and *C. littorale* between 400 and 750 nm.

3.3.3 Discussion

3.3.3.1 Retrieved Optical Properties

Figure 3.3(a) indicate that the refraction index n_λ of all microorganisms features a small dip around 676 nm corresponding to a peak in k_λ caused by Chl *a* absorption. Such a dip was also observed around the same wavelength for various phytoplankton species as illustrated in Figures 6.14 and 6.20 in Ref. [54]. This can be attributed to oscillator resonance around 676 nm. It can also be predicted by optical constant theory such as the Lorentz model [60] or the Helmholtz-Kettler theory [54]. Figure 3.3 also show the error bars associated with the retrieved values of n_λ and k_λ resulting from the propagation of the errors in the measured $\bar{C}_{abs,\lambda}$ and $\bar{C}_{sca,\lambda}$. The relative error, corresponding to 95% confidence interval, associated with n_λ and k_λ was less than 0.1% and 7%, respectively for all the species considered. The absorption index was more sensitive to the experimental uncertainties than the refraction index. Nevertheless, the error propagation from the experimental measurements of $\bar{C}_{abs,\lambda}$ and $\bar{C}_{sca,\lambda}$ to the retrieved complex index of refraction was acceptable.

It is also important to note that the good agreement between measured and predicted cross-sections $\bar{C}_{abs,\lambda}$ and $\bar{C}_{sca,\lambda}$ reported for all species considered could not be obtained when the refraction index n_λ of the microalgae was assumed to be constant over the PAR. In other words, despite the fact that n_λ varies slightly over the PAR, it should not be treated as constant in predicting the microalgae absorption and scattering cross-sections.

3.3.3.2 Compatibility with T-Matrix Method

The above analysis and results rely on the assumptions that the different microalgae can be treated as spherical. However, their circularity and aspect ratio were not exactly unity [5, 65]. To assess the validity and consequences of this assumption, the average absorption

and scattering cross-sections $\bar{C}_{abs,\lambda}$ and $\bar{C}_{sca,\lambda}$ for *B. braunii* measured experimentally were compared with those predicted by the T-matrix method using the retrieved values of n_λ and k_λ . *B. braunii* was of particular interest because it featured the largest average aspect ratio of 1.333 and thus, was the most likely species to show large differences between experimental measurements and predictions by the T-matrix method. The predictions used (i) the average aspect ratio $\epsilon=1.333$ for *B. braunii*, (ii) its equivalent diameter distribution $f(d_s)$ shown in Figure 3.1, and (iii) its refraction and absorption indices retrieved using Lorentz-Mie theory shown in Figure 3.3. The results show that accounting for the non-sphericity of microalgae via the T-matrix method had relatively small effect on both $\bar{C}_{abs,\lambda}$ and $\bar{C}_{sca,\lambda}$ for both species. In fact, the maximum relative difference between T-matrix predictions and experimental data for both $\bar{C}_{abs,\lambda}$ and $\bar{C}_{sca,\lambda}$ was 3.9% for *B. braunii*. Similar or better results were obtained for the other species since their average aspect ratio was closer to unity when Lorentz-Mie theory is valid.

Overall, the effective refraction and absorption indices n_λ and k_λ retrieved over the PAR for all species considered in the present study can be used in the Lorentz-Mie theory or in the T-matrix method along with their size distribution to accurately predict their radiation characteristics.

3.4 Conclusion

This chapter presented and used a methodology to retrieve the spectral refraction and absorption indices of various biofuel producing microalgae from experimentally measured average absorption and scattering cross-sections between 400 and 750 nm. The microalgae were treated as spherical particles with equivalent diameter distributions calculated from experimentally measured major and minor diameter distributions. An inverse method was developed combining Lorentz-Mie theory as the forward method and genetic algorithm. The retrieved refraction and absorption indices were continuous function of wavelength with apparent absorption peaks corresponding to those of *in vivo* Chl *a* and *b*. These optical

properties can be used to predict the radiation characteristics of the species considered using Lorentz-Mie theory or the T-matrix method for a given size distribution and average aspect ratio.

CHAPTER 4

Time-Dependent Radiation Characteristics of *Nannochloropsis Oculata* During Batch Culture

This chapter reports the temporal evolution of the scattering and absorbing cross-sections of marine eustigmatophycease *Nannochloropsis oculata* grown in a flat-plate photobioreactor (PBR). The cross-sections were found to vary significantly with time in response to changes in light and nutrients availability. These variations were interpreted in terms of up- and down-regulations of pigments and other intracellular components. Finally, this study demonstrates that light transfer in the PBR could be predicted using constant radiation characteristics measured during the exponential growth phase with reasonable accuracy provided that the cultures were not nitrogen limited. These results will be useful in the design and operation of PBRs for biofuel production at both small and large scales.

4.1 Introduction

Microalgae are typically suspended in growth medium and cultivated in open pond systems or closed photobioreactors (PBRs) [83]. Batch operation is often preferred over continuous operation for industrial scale PBRs for their simplicity, flexibility, and low cost [108]. To maximize biomass productivity, microalgae strains are usually selected for their rapid growth rate and their ability to tolerate high biomass concentration [33]. To achieve large PBR productivity, photosynthetic microorganisms require an optimal irradiance. At high biomass concentrations, light penetration in the PBR can become severely limiting [2]. Then, a large fraction of the PBR volume may receive insufficient energy to carry out photosynthesis

leading to a significant decrease in biomass productivity. Similarly, excessive irradiance results in photoinhibition which also severely hampers growth rates [109]. To counteract these non-optimal light conditions, photosynthetic microorganisms are able to photoacclimate by either increasing or decreasing the number and size of their photosynthetic units [110]. This enables control over the energy input driving photosynthesis in the cells. Moreover, upon exposure to large irradiance, the decrease in cellular chlorophyll concentration is facilitated by dilution due to cell division [111]. By contrast, under small irradiance, the cells should increase their chlorophyll concentrations at a fast enough rate to compensate for dilution due to cell division. Therefore, microorganisms adapt faster to large irradiance than to small irradiance [111]. Overall, proper light distribution in the PBR is essential for the economic viability of large scale microalgae cultivation systems.

Most cell photosynthetic pigments absorb light in the so-called photosynthetically active radiation (PAR) region from 400 to 700 nm [112]. In addition, the refractive index mismatch between cells and the growth medium causes incident light to be scattered [113]. The absorption and scattering properties of microalgae are species-specific and can be obtained either through experimental measurements [5, 114, 115] or from model predictions based on electromagnetic wave theory [49, 51, 56, 116, 117]. These properties are usually assumed to be time-invariant despite changes in size and composition as the microalgae adapt to changing growth conditions [2, 5, 49–51, 99, 114–116, 118, 119]. Moreover, in order to enhance lipid accumulation, microalgae are deprived of nitrogen through sudden or progressive starvation [120]. As a result, the microalgae culture changes color from green to brown.

Overall, it is important to consider the impact of photoacclimation and nutrient limitation or starvation (particularly nitrogen) on light transfer in PBRs. Changes in growth conditions are typically encountered during the course of batch operation. The goal of this study is to measure the temporal evolution of the radiation characteristics of microalgae during batch growth and to provide physiological interpretation. The results will be used to assess the impact on light transfer in PBRs. The marine eustigmatophycease *Nannochloropsis oculata* was chosen as a model organism for its high lipid content and high biomass productivity

[83, 120].

4.1.1 *Nannochloropsis oculata*

N. oculata microalgae consist of spheroidal cells approximately 2-3 μm in diameter. They possess the pigments Chlorophyll (Chl) *a* and carotenoids. Chl *a* is a crucial pigment in the photosynthetic process [27]. It absorbs mainly blue and red photons and transfer charges by resonance energy transfer to the reaction centers. On the other hand, carotenoids serve as accessory pigments that can be either photosynthetic (PSC) or photoprotective (PPC). Photosynthetic carotenoids absorb green and yellow light and thus broaden the microalgae absorption spectrum [17]. Photoprotective carotenoids prevents photodamage to light harvesting apparatus by converting excess light energy into heat [17]. More specifically, the *in vivo* absorption peaks of Chl *a* are centered around 435, 630, and 676 nm while carotenoids absorb most strongly between 400 and 550 nm [112].

The present study reports the temporal evolution of the absorption and scattering cross-sections of *N. oculata* during batch growth. The impact of physiological adaptations on the microalgae absorption and scattering cross-sections during the different phases of their growth were investigated. The results were used to assess the evolution of light transfer in flat plate PBRs operated in batch mode and to evaluate the validity of the commonly made assumption that microalgae radiation characteristics remain constant during their growth.

4.2 Materials and Methods

4.2.1 Cultivation and sample preparation

The microalgae species *N. oculata* UTEX LB 2164 was purchased from UTEX Austin, TX. It was cultivated in artificial sea water medium in 250 ml culture bottles fitted with vented caps and exposed to a continuous luminous flux of 2800-3000 lux provided by fluorescent light bulbs (GroLux by Sylvania, USA). The artificial seawater medium had the following

composition (per liter of distilled water): NaCl 18 g, $\text{MgSO}_4 \cdot 7\text{H}_2\text{O}$ 2.6 g, KCl 0.6 g, NaNO_3 1 g, $\text{CaCl}_2 \cdot 2\text{H}_2\text{O}$ 0.3 g, KH_2PO_4 0.05 g, NH_4Cl 0.027 g, $\text{Na}_2\text{EDTA} \cdot 2\text{H}_2\text{O}$ 0.03 g, H_3BO_3 0.0114 g, $\text{FeCl}_3 \cdot 6\text{H}_2\text{O}$ 2.11 mg, $\text{MnSO}_4 \cdot \text{H}_2\text{O}$ 1.64 mg, $\text{ZnSO}_4 \cdot 7\text{H}_2\text{O}$ 0.22 mg, $\text{CoCl}_2 \cdot 6\text{H}_2\text{O}$ 0.048 mg, and vitamin B_{12} 0.135 mg.

After 11 days of growth under continuous fluorescent light, 10 ml of the culture was transferred into a 2 cm thick PMMA flat plate PBR. The culture was then diluted with 240 ml of growth medium and the batch experiment started. The PBR was exposed to an illuminance of 7,500 or 10,000 lux (222 or 296 mol $\mu\text{mol photon/m}^2\text{s}$) from red LEDs (C503B-RAN Cree, USA) with peak wavelength at 630 nm and spectral bandwidth of 30 nm. The culture was continuously sparged with 50 cm^3/min of air with 2 vol.% of CO_2 passed through a glass fiber filter of pore size 0.3 μm (HEPA-Vent by Whatman, USA). The entire setup was placed on an orbital shaker operated at 90 rpm to ensure well-mixed conditions and to keep the microorganisms in suspension. The temperature was kept constant at 23°C.

In order to obtain accurate radiation characteristic measurements, the samples taken in the early stages of the batch growth (day 0 to 2) had to be concentrated to achieved higher optical signal-to-noise ratio. Note that the small cell concentration rendered centrifugation of the sample impossible. In addition, absorption and scattering by the growth medium at these low concentrations were not negligible compared with those of *N. oculata*. Thus, prior to optical measurements, 10 mL of the culture suspension was filtered using a 0.45 μm pore size cellulose membrane filters (HAWP-04700 by Millipore, USA). The cells were washed off the filter with 3 mL of phosphate buffer saline (PBS) solution and collected. The growth medium was replaced with non-absorbing PBS solution to achieve the desired microalgae concentration. Upon reaching a sufficiently dense culture, absorption by the growth medium was negligible compared with that of the microalgae and there was no need to concentrate the samples. In fact, samples with high cell concentrations (after day 6) were diluted with PBS to avoid multiple scattering during transmission measurements.

Finally, cell number density N_T of the culture (in $\#/\text{m}^3$) and the distribution of cell diameter $f(d_s)$ based on the equivalent projected-area was measured every 24 hours using

an automatic cell counter (Nexcelom Cellometer Auto M10). To do so, 20 μL of a well mixed culture was pipetted into a disposable haemocytometer (Nexcelom CHT4-SD100). The device counted the number of cells present in the known volume of the haemocytometer through the use of 2D micrographs. Each cell density measurement reported corresponded to the average cell count of two samples, each counted twice.

4.2.2 Radiation characteristics

The average absorption and scattering cross-sections of *N. oculata* were measured every 24 hours for up to 18 days. The following assumptions were made in the data analysis: (1) the microalgae suspension was well mixed and randomly oriented, (2) single scattering prevailed thanks to the low cell densities considered, and (3) the scattering phase function was assumed to be time-invariant and constant over the PAR region. Kandilian et al. [121] measured, with a polar nephelometer, the scattering phase function at 633 nm for *N. oculata* grown under red LEDs in artificial sea water medium. The backward scattering ratio b_λ was reported to be 0.0019. They also retrieved the complex index of refraction and verified that the scattering phase function was nearly independent of wavelength over the PAR region. The growth conditions and measured diameters of *N. oculata* cells reported in their study were similar to that in the present study. Therefore, these prior measurements were adopted.

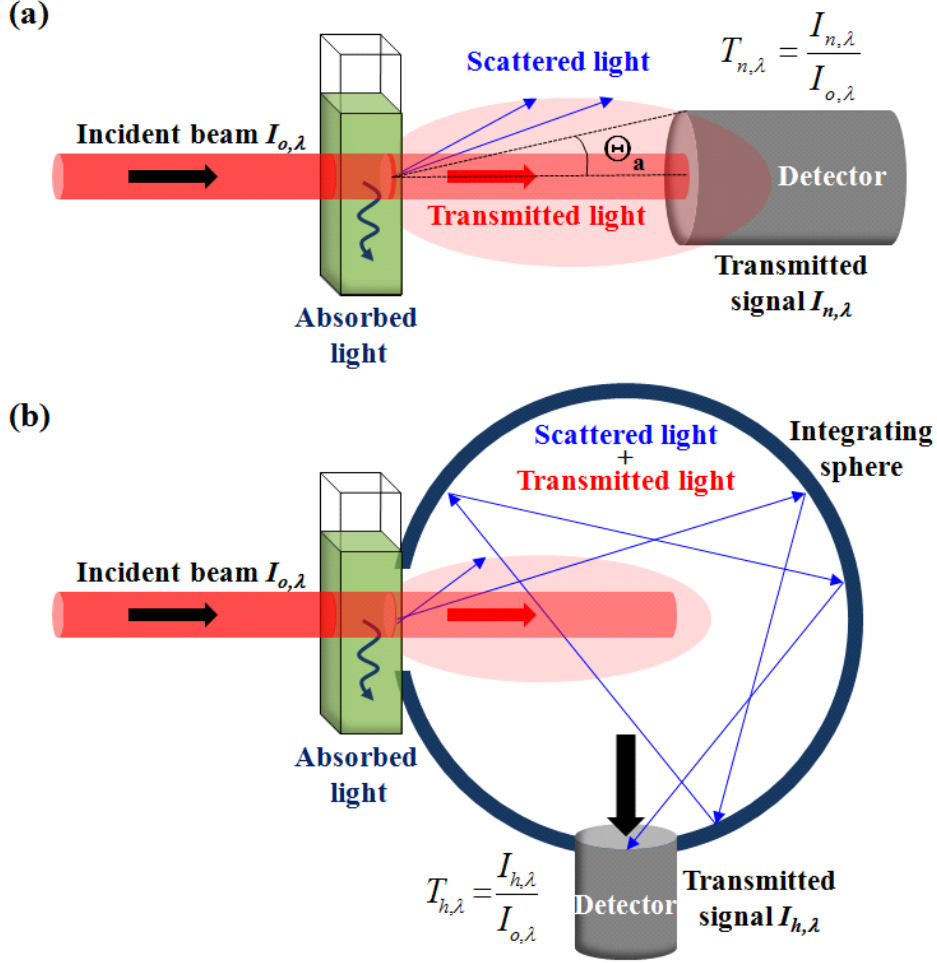


Figure 4.1: Schematic of experimental setup used to determine (a) the extinction coefficient β_λ from normal-normal spectral transmittance and (b) the absorption coefficient κ_λ from normal-hemispherical spectral transmittance.

The extinction coefficient of the microalgae suspension β_λ was obtained from normal-normal transmittance measurements, denoted by $T_{n,\lambda}$, after correcting for forward scattering by the suspension [92]. The measurements were performed in 1 cm pathlength cuvettes using a UV-VIS spectrometer (Shimadzu, USA, Model UV-3103PC) from 400 to 750 nm with 1 nm spectral resolution as illustrated in Figure 7.2a. In order to correct for the effects of reflection and refraction by the cuvette, the measurements were calibrated using the transmittance of the reference medium (i.e., PBS) denoted by $T_{n,\lambda,ref}$. Then, the apparent extinction

coefficient χ_λ was defined as [92, 122]

$$\chi_\lambda = -\frac{1}{t} \ln \left(\frac{T_{n,\lambda}}{T_{n,\lambda,ref}} \right) \quad (4.1)$$

The detector has a finite size and detected a portion of the light scattered in the forward direction. This effect should be corrected for since *N. oculata* scatters light largely in the forward direction [121]. The apparent extinction coefficient can be related to the actual absorption and scattering coefficients by [92, 122],

$$\chi_\lambda = \kappa_\lambda + \sigma_{s,\lambda} - \epsilon_n \sigma_{s,\lambda} \quad (4.2)$$

where ϵ_n represents the fraction of scattered light reaching the detector and is expressed as [123, 124]

$$\epsilon_n = \frac{1}{2} \int_0^{\Theta_a} \Phi_{T,\lambda}(\theta) \sin \theta \, d\theta \quad (4.3)$$

where Θ_a is the half acceptance angle of the detector while the scattering phase function $\Phi_{T,\lambda}$ of *N. oculata* was measured by Kandilian *et al.* [121].

The absorption coefficient κ_λ was obtained from normal-hemispherical transmittance measurements, denoted by $T_{h,\lambda}$, performed with an integrating sphere (ISR-3100 by Shimadzu, USA) at wavelengths from 400 to 750 nm as illustrated in Figure 7.2b [114]. Then, the apparent absorption coefficient $\chi_{h,\lambda}$ can be expressed as

$$\chi_{h,\lambda} = -\frac{1}{t} \ln \left(\frac{T_{h,\lambda}}{T_{h,\lambda,ref}} \right) \quad (4.4)$$

Due to imperfect reflections at the inner surface of the integrating sphere and the geometry of the experimental setup, the detector is unable to capture all the scattered light. In order to correct for these errors, the apparent absorption coefficient can be related to the actual absorption and scattering coefficients by

$$\chi_{h,\lambda} = \kappa_\lambda + (1 - \epsilon_h) \sigma_{s,\lambda} \quad (4.5)$$

where ϵ_h represents the fraction of scattered light detected by the integrating sphere and is assumed to be constant over the PAR region. Davis-Colley [122] noted that there exist

a wavelength λ_o at which microalgae did not absorb radiation. For example, $\lambda_o = 750$ nm for *N. oculata* [121]. Thus, the absorption coefficient at λ_o vanishes ($\kappa_\lambda = 0$) and ϵ_h can be retrieved from Equation (7.14) as according to

$$\epsilon_h = 1 - \frac{\chi_{h,\lambda_o}}{\sigma_{s,\lambda_o}} \quad (4.6)$$

Similarly, the apparent extinction coefficient at wavelength λ_o can be retrieved from Equation (7.12) as

$$\chi_{\lambda_o} = (1 - \epsilon_n)\sigma_{s,\lambda_o} \quad (4.7)$$

Combining Equations (7.12), (7.14), (7.15), and (4.7), the actual absorption coefficient κ_λ can be obtained using the following expression,

$$\kappa_\lambda = \chi_{h,\lambda} - \chi_{h,\lambda_o} \frac{\sigma_{s,\lambda}}{\sigma_{s,\lambda_o}} \quad \text{where} \quad \frac{\sigma_{s,\lambda}}{\sigma_{s,\lambda_o}} = \frac{\chi_\lambda - \chi_{h,\lambda}}{\chi_{\lambda_o} - \chi_{h,\lambda_o}} \quad (4.8)$$

Finally, the actual extinction coefficient β_λ was obtained by substituting κ_λ into Equation (7.12). Then, the scattering coefficient was computed using the definition $\sigma_{s,\lambda} = \beta_\lambda - \kappa_\lambda$.

Note that the samples were manually shaken prior to the transmission measurements so as to prevent sedimentation. Each measurement was performed with two samples of different cell densities. The sample normal-normal and normal-hemispherical transmittances were measured three times and the results were averaged. The absorption and scattering coefficients κ_λ and $\sigma_{s,\lambda}$ were divided by the samples respective cell number density N_T to obtain the average absorption and scattering cross-sections $\bar{C}_{abs,\lambda}$ and $\bar{C}_{sca,\lambda}$ according to Equation (3.4). Van de Hulst [125] suggested that “a simple and conclusive test for the absence of multiple scattering” consists of demonstrating that scattering intensity is directly proportional to the particle concentration. In other words, the spectral cross-sections $\bar{C}_{abs,\lambda}$ and $\bar{C}_{sca,\lambda}$ for different cell densities should collapse onto a single line if single and independent scattering prevailed. This provided further validation of the experimental procedure and data analysis.

4.2.3 Chemical analysis

The pH of each sample was determined with a pH meter (Omega PHB-212). This provided an indirect method for monitoring CO₂ concentrations in the culture. Indeed, dissociation of CO₂ in water causes the solution to become slightly acidic. Therefore, an increase in pH could be interpreted as lower CO₂ concentration in the microalgae culture.

Pigment concentrations were determined spectrophotometrically using the method reported by Wellburn [126]. A 2 ml sample of microalgae culture was centrifuged for 2 minutes at 10,000 rpm (6,500 g) and the supernatant discarded. Then, 3 ml of methanol was added to the cell pellet. The sample was vortexed for 1 minute followed by sonication for 4 minutes. This ensured that the microalgae cell walls were broken down. The sample was left in a dark room for 24 hours before being centrifuged to remove cell debris. The supernatant was extracted and transferred into 1 cm pathlength polystyrene cuvettes for normal-normal transmittance ($T_{n,\lambda}$) measurements at 480, 666, and 750 nm. The corresponding optical density (OD) was defined as $OD_\lambda = -\ln T_{n,\lambda}$. Pigment extraction was performed in duplicates and OD measurements in triplicates. Chl *a* concentration C_{chla} (in $\mu\text{g}/\text{m}^3$ of suspension) was determined from the OD measurements according to [126]

$$C_{chla} = 15.65(OD_{666} - OD_{750})v/Vl \quad (4.9)$$

where V is the microalgae sample volume (in m^3), v is the volume of methanol (in m^3), and l is the pathlength of the cuvette (in cm), taken as $V = 2$ ml, $v = 3$ ml, and $l = 1$ cm. Similarly, the total carotenoid concentration C_{x+c} including both PSC and PPC was calculated as [127]

$$C_{x+c} = 4(OD_{480} - OD_{750})v/Vl \quad (4.10)$$

The pigment concentration (in $\mu\text{g}/\text{cell}$) was estimated as the ratio of the mass of pigment mass per unit volume (in $\mu\text{g}/\text{m}^3$) to the cell number density N_T (in $\#/\text{m}^3$). For the culture grown under 10,000 lux, pigment extractions were only conducted after 145 hours in order to preserve culture volume and to investigate the behavior of the pigment concentrations in the later stages of microalgae growth during nitrogen starvation.

4.3 Results and Discussions

4.3.1 Cell growth

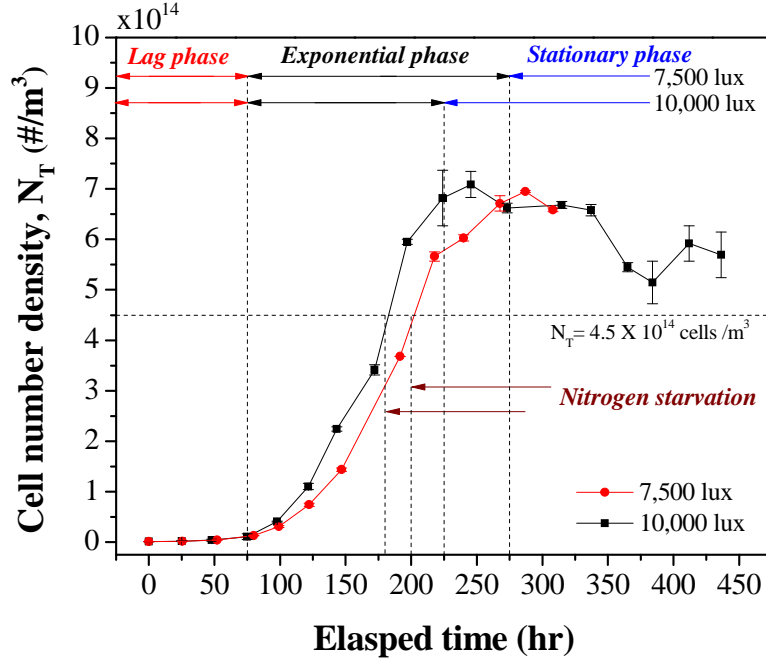


Figure 4.2: Cell number density evolution with respect to growth times for *N. oculata* batch cultures grown under 7,500 and 10,000 lux of red light. Lag, exponential, and stationary phases and onset of nitrogen starvation are also shown.

Figure 4.2 shows the temporal evolution of the cell number density N_T for microalgae cultures grown under 7,500 and 10,000 lux. Each data point represents the arithmetic mean of the measurements and the error bars correspond to one standard deviation. The growth curves exhibited the typical microalgal growth phases namely (i) the lag phase, (ii) the exponential phase, and (iii) the stationary phase. For both incident irradiance, the lag phase was characterized by slow initial growth rates and occurred approximately between 0 and 50-75 hours. It can be attributed to the microalgae's adaptation to drastically different growth conditions after their transfer from the culture bottle to the PBR [128]. The exponential phase occurred immediately after the lag phase and was characterized by large growth rates.

N. oculata cultures grew faster under 10,000 lux than under 7,500 lux. The stationary phase occurred after approximately 225 and 275 hours for cultures grown under 10,000 and 7,500 lux, respectively. It could be due to insufficient light, nutrients, and/or CO₂. The cultures grown under 7,500 and 10,000 lux reached about the same maximum cell density of 6.8×10^{14} cells/m³. It is important to note that the large fluctuations in number density N_T during the stationary phase was due to the formation of microalgae colonies that adhered to the inner surfaces of the PBR. However, subsequent measurements of the radiation characteristics remain correct because these colonies were not collected during sampling. Note also that the equivalent cell diameter d_s was $2.63 \mu\text{m} \pm 0.5 \mu\text{m}$ and did not vary significantly with time.

Moreover, the pH of the culture remained between 7.6 and 8.2 and did not increase significantly during the microalgae growth. Chiu *et al.* [129] reported that *N. oculata* culture grown in continuous mode maintained a pH of 7.8 when aerated with air enriched with 2 vol.% of CO₂. Despite the differences between batch and continuous modes, the pH was nearly similar. The slight increase in pH was caused by the growth of the microalgae and the corresponding increase in CO₂ uptake. These observations suggest that light and CO₂ availability were not limiting factors [129,130]. Thus, nutrient starvation was responsible for the stationary phase.

Elemental analysis similar to that reported by Kandilian *et al.* [121] for the same microalgae species grown in the Erdshreibers medium was performed in the present study for artificial sea water medium. It predicted that the culture experienced nitrogen starvation at dry biomass concentrations of 1.72 g/L. This dry biomass concentration can be converted into cell number densities by treating *N. oculata* cells as spheres with an average diameter of $2.63 \mu\text{m}$, water volume fraction taken as 0.7 [131], and dry biomass density taken as 1350 kg/m³ [116]. Then, nitrogen starvation was expected to occur at $N_T = 4.5 \times 10^{14}$ cells/m³. The cultures grown under 7,500 and 10,000 lux reached this concentration after 200 and 180 hours, respectively. These values show that the microalgae were actually nutrient limited midway through their exponential phase but continued growing to more than twice their concentrations before reaching the stationary phase.

4.3.2 Mass absorption and scattering cross-sections

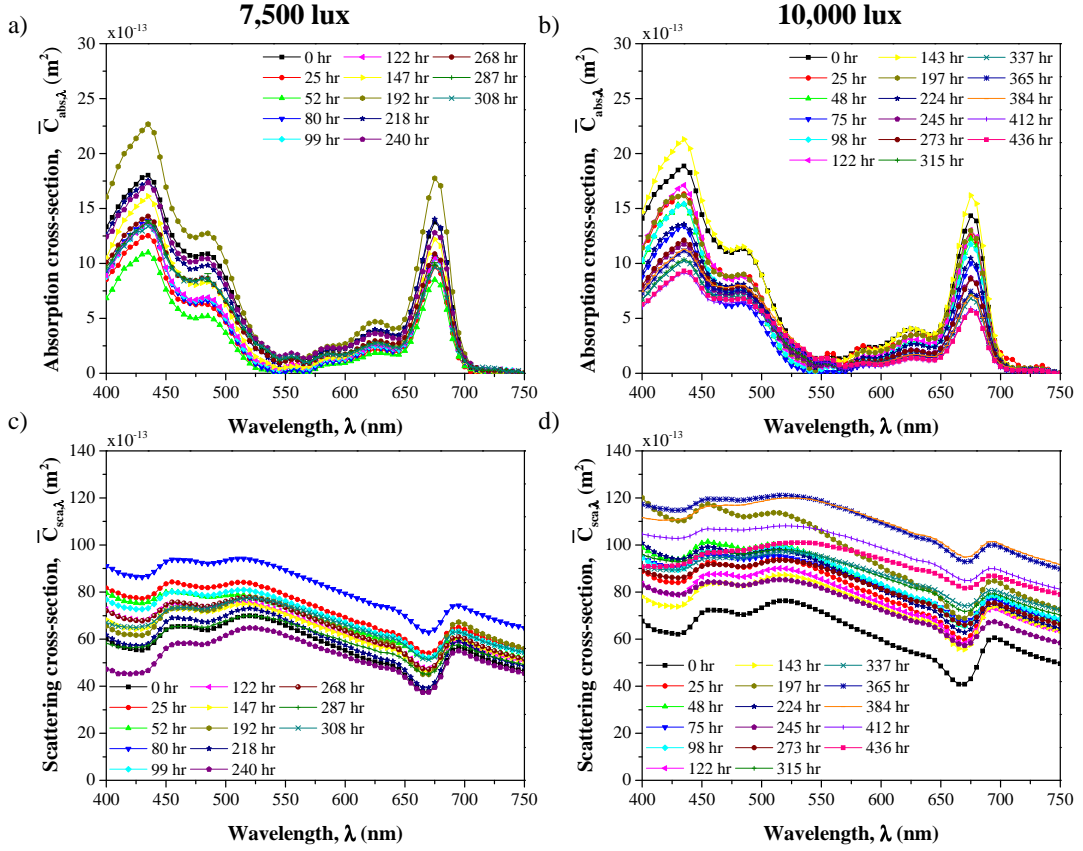


Figure 4.3: (a) and (b) Average absorption cross-section $\bar{C}_{abs,\lambda}$ and (c) and (d) average scattering cross-section $\bar{C}_{sca,\lambda}$ in the spectral range from 400 to 750 nm for *N. oculata* grown under 7,500 and 10,000 lux, respectively.

Figures 4.3a and 4.3b present the average absorption cross-sections $\bar{C}_{abs,\lambda}$ of *N. oculata* grown under 7,500 and 10,000 lux, respectively, in the spectral range from 400 to 750 nm at different times during their growth. The average absorption cross-section $\bar{C}_{abs,\lambda}$ displayed peaks at 435, 630, and 676 nm corresponding to *in vivo* absorption peaks of Chl *a* and at 485 nm corresponding to that of carotenoids. Similarly, Figures 4.3c and 4.3d present the average scattering cross-sections $\bar{C}_{sca,\lambda}$ of *N. oculata* grown under 7,500 and 10,000 lux, respectively. The cross-sections $\bar{C}_{sca,\lambda}$ and $\bar{C}_{abs,\lambda}$ measured at time 0 hour were similar

for the two incident irradiances considered. This confirms that the initial conditions and experimental measurements were consistent. The absorption cross-section $\bar{C}_{abs,\lambda}$ feature similar values and trends for both incident irradiances. For a given incident irradiance, $\bar{C}_{abs,\lambda}$ at wavelength λ in the PAR region varied significantly during the course of the experiments. For example, the relative difference between the minimum and maximum values of $\bar{C}_{abs,676}$ reached up to 226% for culture grown under 10,000 lux. The same relative difference for $\bar{C}_{abs,485}$ reach up to 145% for culture grown under 7,500 lux.

Furthermore, for any given time and wavelength, the scattering cross-section $\bar{C}_{sca,\lambda}$ for *N. oculata* grown under 10,000 lux was systematically larger than those grown under 7,500 lux while trends in their temporal evolution were similar. The scattering cross-section of a cell depends on its size and on the refractive index mismatch between the cell and the surrounding medium. The effective refractive index of the microalgae depends on their water content and their chemical composition [113, 131]. The major cell constituents, namely, proteins, carbohydrates, and lipids do not absorb in the PAR region and have refractive indices larger than that of water. In addition, carbohydrates and proteins have larger refractive indices than lipids [131]. Carbohydrates and proteins concentrations in *N. oculata* was reported to increase at the expense of lipids when grown under larger incident irradiance [132]. This may explain why $\bar{C}_{sca,\lambda}$ was larger for microalgae grown under 10,000 lux than that under 7,500 lux. In addition, carbohydrates, proteins, and lipids have index of refraction nearly constant over the PAR region [131] while the cell size distribution remains nearly unchanged over time. This could be the reason why $\bar{C}_{sca,\lambda}$ increased or decreased almost uniformly across the PAR over time.

It is also worth noting that dips in the scattering cross-sections $\bar{C}_{sca,\lambda}$ were observed around wavelengths corresponding to the absorption peaks in $\bar{C}_{abs,\lambda}$. This “cross-talk” between absorption and scattering cross-sections can be attributed to resonance behavior in the real part (or refraction index) of the complex index of refraction of the microalgae at wavelengths when the imaginary part (or absorption index) features strong absorption peaks. Such resonance is predicted by the Ketteler-Helmholtz theory [113], among others.

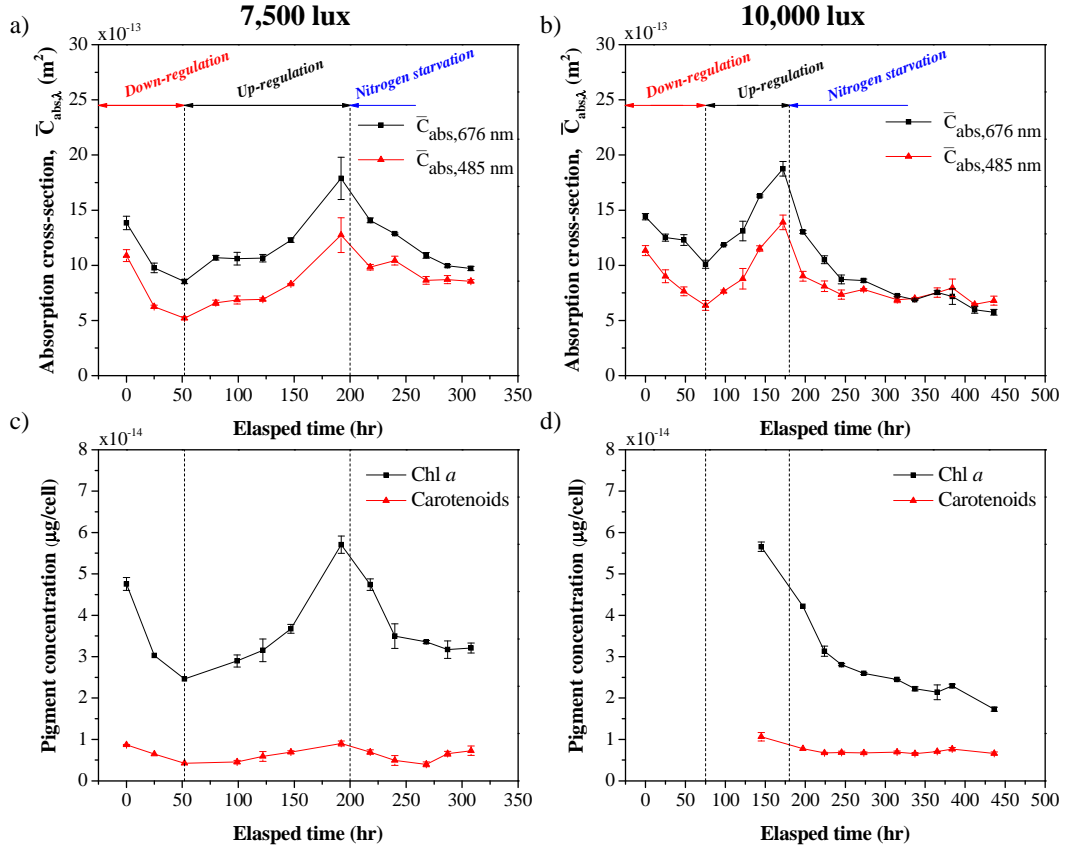


Figure 4.4: (a) and (b) Temporal evolutions of average absorption cross-section at 485 and 676 nm and (c) and (d) pigment concentrations (Chl *a* and carotenoids) for *N. oculata* grown under 7,500 and 10,000 lux, respectively.

To illustrate the temporal evolution of the absorption cross-section, Figures 4.4a and 4.4b plot $\bar{C}_{abs,\lambda}$ at wavelengths 485 nm and 676 nm with respect to time. These wavelengths correspond to carotenoids and Chl *a* absorption peaks, respectively. Similarly, Figures 4.4c and 4.4d show the measured Chl *a* and total carotenoids (PSC + PPC) concentrations as functions of time. Each data point represents the arithmetic mean of multiple measurements and the error bars correspond to one standard deviation. It is evident that the trends in the absorption peaks $\bar{C}_{abs,676}$ and $\bar{C}_{abs,485}$ closely follow the trends in Chl *a* and PSC+PPC concentrations, respectively. In fact, $\bar{C}_{abs,676}$ and $\bar{C}_{abs,485}$ and the corresponding pigment concentration reach their maximum and minimum at the same times. The initial down-regulation

of pigment was caused by exposure to excessive fluence rates when the suspensions featured relatively small cell number densities. It contributed to reducing the energy absorbed per cell to prevent photodamage to their light-harvesting antenna. It is interesting to note that the time frame during which pigment concentrations decreased closely coincided with the lag phase observed in the growth curves between 0 and 50-75 hours (Figure 4.2).

Moreover, Figures 4.4c and 4.4d indicate that Chl *a* and carotenoids concentrations increased between times 50 and 200 hours for the culture grown under 7,500 lux and between 75 and 180 hours for those grown under 10,000 lux. This was due to up-regulation of pigments by microalgae to avoid photolimitation. Indeed, due to rapid cell division in the exponential growth phase, the local fluence rate in the PBR decreased. To compensate, the microalgae synthesized additional photosynthetic pigments in order to absorb more light.

Finally, nitrogen starvation causes reduction in pigment synthesis rates [133]. As predicted from elemental analysis [121], the cultures grown under 7,500 and 10,000 lux became nitrogen limited after about 200 and 180 hours, respectively (Figure 4.2). Interestingly, Figures 4.4c and 4.4d show that pigment concentrations decreased sharply around the same times. In fact, the culture's color changed from green to brown during nitrogen starvation due to the increase in the ratio of carotenoids to Chl *a*.

4.3.3 Average fluence rate and radiant power absorbed

As previously mentioned, past studies typically measured the radiation characteristics only once during the microorganisms' exponential growth phase [5, 51, 99, 114, 115]. Similarly, simulations of coupled light transfer and growth kinetics typically assume that radiation characteristics remain constant throughout the microalgae growth [49, 118, 119]. However, the spectral absorption cross-section $\bar{C}_{abs,\lambda}$ of *N. oculata* varied significantly during batch growth and reached (i) its minimum at the beginning of the exponential phase and (ii) its maximum immediately before nitrogen starvation. Here, the two-flux approximation given by Equation (2.8) was used to evaluate the temporal evolution of the average fluence rate

G_{ave} and the average radiant power absorbed per cell A_{ave} given by Equations (2.8) and (2.12), respectively. The incident radiation $G_{in,\lambda}$ was normal to the front surface of the PBR ($\theta_c = 0^\circ$) and the back surface was treated as transparent ($\rho_\lambda = 0$).

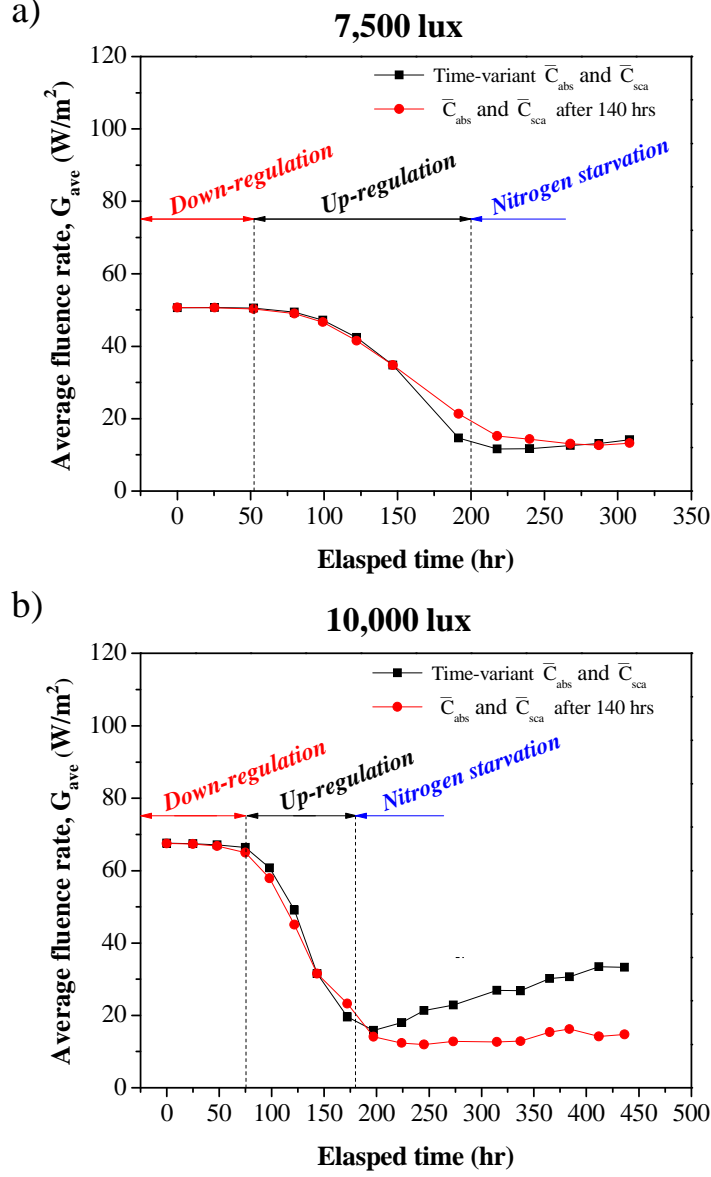


Figure 4.5: Evolution of the average fluence rate in the flat-plate PBR as a function of time for cultures grown under (a) 7,500 lux and (b) 10,000 lux predicted using Equation (2.8) to (2.11) and (i) time-dependent $\bar{C}_{abs,\lambda}$ and $\bar{C}_{sca,\lambda}$ and (ii) $\bar{C}_{abs,\lambda}$ and $\bar{C}_{sca,\lambda}$ measured after ~ 140 hours during the exponential phase.

Figures 4.5a and 4.5b show the evolution of the average fluence rate G_{ave} with respect to time for the cultures grown under 7,500 and 10,000 lux, respectively. It was predicted

using Equations (2.8) to (2.11) along with (i) the measured time-dependent cross-sections $\bar{C}_{abs,\lambda}$ and $\bar{C}_{sca,\lambda}$ (Figure 4.3) and (ii) the values of $\bar{C}_{abs,\lambda}$ and $\bar{C}_{sca,\lambda}$ measured after about 140 hours during the exponential growth phase. Predictions of G_{ave} using the measured time-dependent cross-sections $\bar{C}_{abs,\lambda}$ and $\bar{C}_{sca,\lambda}$ represents the most accurate estimate of the average fluence rate. During the lag phase or the pigment down-regulation period, G_{ave} was almost equal to G_{in} due to very low microalgae concentrations in both cultures. During the exponential growth phase, G_{ave} rapidly decreased as the microalgae simultaneously increased their number density N_T and up-regulated their pigments. Upon nitrogen starvation, G_{ave} started increasing due to the sharp decrease in pigment concentrations even though the microalgae cells continued growing. Here, G_{ave} predicted using $\bar{C}_{abs,\lambda}$ and $\bar{C}_{sca,\lambda}$ measured after ~ 140 hours was adequate if the microorganisms were not in the nitrogen starvation phase when pigment concentrations decreased sharply. During the pigment down-regulation and up-regulation phases, the relative difference in G_{ave} predicted using $\bar{C}_{abs/sca,\lambda}(t)$ and $\bar{C}_{abs/sca,\lambda}(\sim 140 \text{ h})$ was less than 2% and 8% for incident irradiance of 7,500 and 10,000 lux, respectively. However, it reached 45% and 57% in the nitrogen starvation phase, respectively. Therefore, in the latter phase, radiation characteristics should be measured as a function of time to predict the rapid increase in fluence rate.

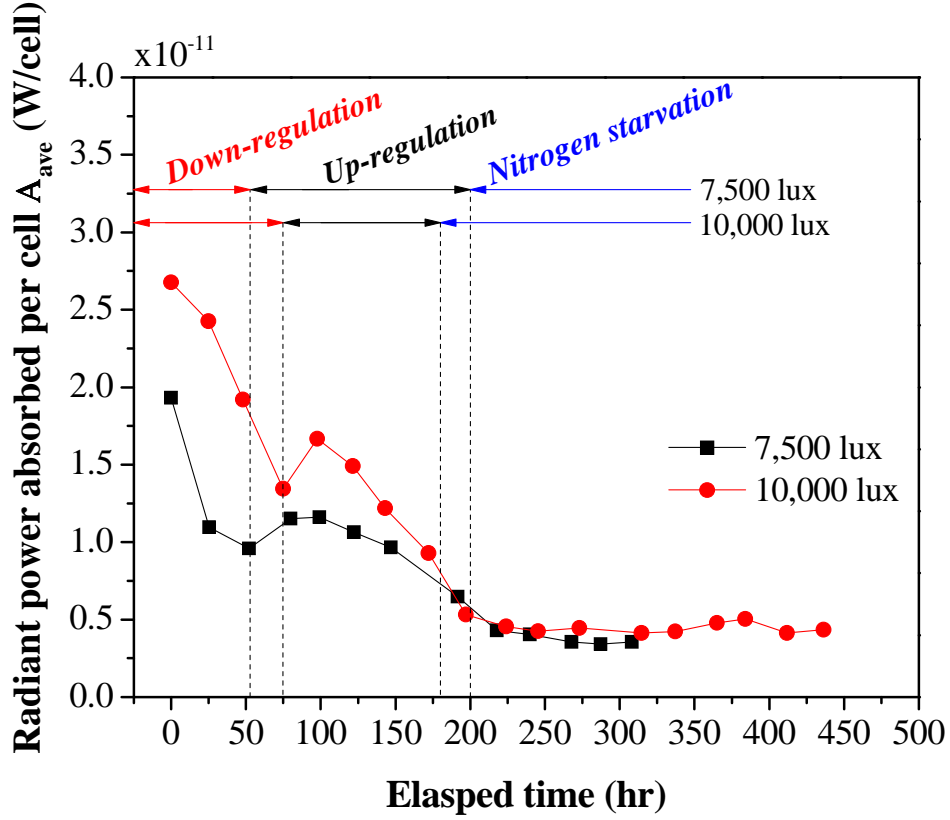


Figure 4.6: Evolution of the average radiant power absorbed per microalgae cell A_{ave} [Equation (2.12)] for cultures grown under 7,500 and 10,000 lux.

Figure 4.6 shows the temporal evolution of the average radiant power absorbed per microalgae cell A_{ave} for cultures grown under 7,500 and 10,000 lux predicted using Equation (2.12). For both incident irradiances of 7,500 and 10,000 lux, A_{ave} decreased rapidly during the down-regulation phase. This was due to the sharp decrease in pigment concentrations in response to excessive average fluence rate in the PBR. More interestingly, in the up-regulation phase, A_{ave} featured an initial increase followed by a subsequent decrease for both incident irradiances. This can be attributed to the fact that the increase in pigment concentrations (Figures 4.4c and 4.4d) initially compensated for the decrease in fluence rate. However, it could not compensate for the rapid cell growth that further decreased the fluence rate and for the pigment dilution through cell division, as previously mentioned.

4.4 Chapter summary

This chapter presented the temporal evolution of the average scattering and absorbing cross-sections from 400 to 750 nm for *N. oculata* grown in batch cultures under 7,500 and 10,000 lux of red light at 630 nm. These cross-sections were found to vary significantly with time in response to changes in fluence rate and nutrients availability. Their evolution was interpreted in terms of up and down-regulation of pigments and cell components in response to changing growth conditions. The observed changes in the absorption and scattering cross-sections in response to the growth conditions are likely to be representative of other microalgae species by virtue of the fact that most species have similar pigments (e.g. Chl *a*) and are able to photoacclimate [110, 111]. In addition, the impact on the average radiant power absorbed per cells and on the average fluence rate in the PBR were discussed. The average fluence rate in the PBR can be predicted reasonably well using radiation characteristics measured during the exponential growth phase provided the microalgae are not nitrogen limited. In the case of nitrogen limitations, the radiation characteristics should be measured as a function of time.

CHAPTER 5

Radiation Characteristics and Optical Properties of Filamentous Cyanobacterium *Anabaena Cylindrica*

This chapter presents experimental measurements of the spectral absorption and scattering cross-sections and the spectral complex index of refraction of filamentous cyanobacterium *Anabaena cylindrica* from 400 to 750 nm at four different times during its batch growth. Its filaments, consisting of long chains of polydisperse cells, were modeled as infinitely long and randomly oriented volume-equivalent cylinders. The spectral complex index of refraction were retrieved using an inverse method based on genetic algorithm. The absorption peaks of Chl *a* and PCCN concentrations were found to vary in response to light and nitrogen availability. These results can be used for predicting and optimizing light transfer in photobioreactors for wastewater treatment and ammonia or biofuel production.

5.1 Introduction

Photobioreactors can be optimized to increase ammonia, hydrogen, and/or lipid production rates through light transfer modeling coupled with growth kinetics [2,118]. To do so, spectral radiation characteristics are necessary parameters. However, measuring them can be costly and time consuming. Instead, they could be numerically predicted more easily based on the microorganism size distribution and complex index of refraction. This approach has been applied to spherical single cell microorganisms based on Lorenz-Mie theory [134]. However, some cyanobacteria are filamentous and cannot be treated as spherical. The goal of this chapter is to develop an inverse method to retrieve the spectral real (refraction index)

and imaginary (absorption index) parts of the complex index of refraction of filamentous cyanobacteria. *A. cylindrica* was chosen as a model organisms and its radiation characteristics were measured.

5.1.1 *Anaebena cylindrica*

The freshwater cyanobacterium *Anabaena cylindrica* belongs to a genus known for its ability to fix nitrogen and produce ammonia using the enzyme nitrogenase contained in differentiated cells called heterocysts [135–137]. The *Anabaena* genus has been used to remove nitrates and phosphates from contaminated waters as well as to produce fertilizers by photosynthesis and fixation of atmospheric nitrogen [138]. In addition, despite its low lipid content of about 5 dry wt.% [33], *A. cylindrica* has also been considered for biodiesel production due to its large cell size and its filamentous morphology requiring less energy intensive harvesting methods, such as filtration, to separate the biomass from the growth medium.

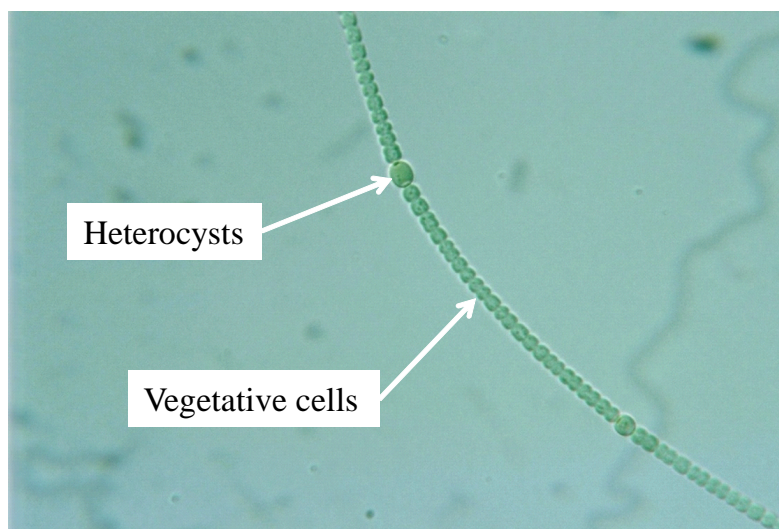


Figure 5.1: Micrograph image of *A.cylindrica* showing vegetative cells and heterocysts 2.5-3 μm in diameter. Reproduced with permission from Prof. Yuuji Tsukii, Hosei University, Protist Information Server <http://protist.i.hosei.ac.jp>.

Figure 5.1 shows a micrograph of the heterocystous filamentous *A. cylindrica* consisting of connected and nearly spherical vegetative cells and fewer and larger heterocysts 2-4 μm in diameter. Filaments' length varies widely but typically exceeds 100 μm . In response to nitrogen limitation, *A. cylindrica* increases its heterocyst differentiation rate and nitrogenase activity [133]. It also adapts its pigment concentrations. *A. cylindrica* possesses the pigments chlorophyll *a* (Chl *a*) and accessory pigments phycocyanin (PCCN) and carotenoids [139]. They enable it to absorb over different spectral bands of the PAR region for a more efficient utilization of solar energy. In fact, the *in vivo* absorption peaks of these pigments are distinct with Chl *a* absorbing most strongly around 436 and 676 nm [4], PCCN around 630 nm [140], and photosynthetic (PSC) and photoprotective (PPC) carotenoids between 400 and 550 nm [4].

5.1.2 Radiation characteristics of photosynthetic microorganisms

The radiation characteristics of photosynthetic microorganisms in suspension can be obtained either through experimental measurements [5, 114, 115] or numerical simulations [49, 51, 56]. Most efforts have focused on quasi-spherical cells such as the green microalgae *C. reinhardtii* [49, 115]. Pilon and co-workers experimentally measured the radiation characteristics of several photosynthetic H_2 producing microorganisms [114, 115] and of lipid producing green microalgae [5, 121]. The absorption κ_λ and scattering $\sigma_{s,\lambda}$ coefficients of these microorganisms were normalized either by their cell number densities N_T in ($\#/ \text{m}^3$) [5] or by their dry mass concentrations X [114, 115] according to Equation (2.6). The cell number density N_T of single-cell microorganisms can be easily measured. However, filamentous cyanobacteria consist of long chains of cells. Defining their number density N_T becomes difficult as both the number of cells and filaments must be considered for an accurate characterization of their morphology. Therefore, the absorption κ_λ and scattering $\sigma_{s,\lambda}$ coefficients of filamentous cyanobacteria should be normalized by their dry mass concentration X , as performed for *Anaebena variabilis* [114].

Moreover, microorganisms are typically modeled as scattering particles with time-invariant

radiation characteristics [2, 118, 119]. The latter are often measured only once during the entire growth typically during the exponential phase [5, 51, 99, 114, 115]. However, microalgae and cyanobacteria undergo changes in pigment concentration as well as changes in their lipid, protein, and carbohydrate content in response to photoadaptation [110] or nutrient limitation [111]. These changes in the cell composition may strongly affect their radiation characteristics [54].

The present study aims to retrieve the spectral effective complex index of refraction of cyanobacterium *A. cylindrica* by treating its filaments of vegetative cells and heterocysts as infinitely long and randomly oriented cylinders. To do so, the scattering phase function $\Phi_{T,\lambda}(\hat{\mathbf{s}}_i, \hat{\mathbf{s}})$ as well as the average mass absorption $\bar{A}_{abs,\lambda}$ and scattering $\bar{S}_{sca,\lambda}$ cross-sections were measured from 400 to 750 nm at different times during batch growth.

5.2 Materials and Methods

5.2.1 Cultivation and sample preparation

Heterocystous filamentous cyanobacterium *Anabaena cylindrica* Lemmermann UTEX B1611 was purchased from UTEX Austin, TX. It was cultivated in BG-11(-N) medium in 250 ml culture bottles fitted with vented caps and exposed to a continuous luminous flux of 2,800-3,000 lux (85-91 $\mu\text{mol photon/m}^2\cdot\text{s}$) provided by fluorescent light bulbs (GroLux by Sylvania, USA). The BG-11(-N) medium had the following composition (per liter of distilled water): K_2HPO_4 40 mg, $\text{MgSO}_4\cdot 7\text{H}_2\text{O}$ 7.5 mg, $\text{CaCl}_2\cdot 2\text{H}_2\text{O}$ 36 mg, citric acid $\cdot\text{H}_2\text{O}$ 6 mg, ferric ammonium citrate 6 mg, $\text{Na}_2\text{EDTA}\cdot 2\text{H}_2\text{O}$ 6 mg, H_3BO_3 2.86 mg, $\text{MnCl}_2\cdot 4\text{H}_2\text{O}$ 1.81 mg, $\text{ZnSO}_4\cdot 7\text{H}_2\text{O}$ 0.22 mg, $\text{Na}_2\text{MoO}_4\cdot 2\text{H}_2\text{O}$ 0.39 mg, $\text{CuSO}_4\cdot 5\text{H}_2\text{O}$ 0.079 mg, and $\text{Co}(\text{NO}_3)_2\cdot 6\text{H}_2\text{O}$ 0.0049 mg. This medium was recommended by UTEX and similar irradiance has been used in Ref. [137].

Nutrient availability in the medium can be estimated by elemental analysis [121]. The complete elemental composition of *A. cylindrica* was not available in the literature. However,

the elemental composition does not vary significantly between species of the same genus [141,142]. The nitrogen content of *A. cylindrica* was reported to be 5 to 10.8 % by percentage of dry weight [143] while the cyanobacterium *Anabaena flos-aquae* was reported to have 1 dry wt. % of K and 0.8 dry wt. % of P [144]. These values suggest that the culture of *A. cylindrica* in BG-11(-N) medium would be limited in P and K at mass concentrations of 0.825 and 1.583 kg/m³, respectively. On the other hand, the medium contained only traces of nitrates. It remains unclear whether the culture was nitrogen deficient, i.e., whether the rate of nitrogen uptake exceeded the rate of nitrogen-fixation.

The culture bottles were placed on an orbital shaker operated at 70 rpm to ensure sufficient mixing to keep the microorganisms in suspension. Samples of 3 ml were collected from the culture after 6, 9, 12, and 14 days of growth to measure their radiation characteristics. These time intervals were selected to allow for sufficient cyanobacteria growth between measurements. Note that the culture started forming colonies after 15 days of batch growth after which experiments ended. To eliminate possible absorption and scattering by the growth medium, the suspension samples were centrifuged at 2,000 rpm (1,300 g) for 10 minutes, washed twice with phosphate buffer saline (PBS) solution, and suspended in PBS [114, 115, 121]. Smaller volumes of PBS were used to replace the growth medium in order to obtain larger biomass concentrations in the samples than in the culture. This was performed to obtain higher signal-to-noise ratio in the transmission measurements.

A calibration curve relating the optical density (OD) of the suspension at 750 nm to the dry mass concentration X was obtained prior to performing the radiation characteristics measurements. The optical density was measured for five different mass concentrations of *A. cylindrica* in disposable polystyrene cuvettes with 1 cm pathlength using a UV-VIS spectrophotometer (Shimadzu, USA, Model UV-3103PC) [114, 115, 121]. The dry mass concentrations were obtained by filtering the cells with 0.45 μ m pore size cellulose membrane filters (HAWP-04700 by Millipore, USA) followed by overnight drying at 60°C in a vacuum oven [121]. The dried filters with the dry cells were weighed immediately after being removed from the oven using a precision balance (model AT261 by Delta Range Factory, USA) with a

0.01 mg precision [121]. The mass concentration was related to the optical density according to

$$X = 0.816OD_{750} \quad (5.1)$$

with a coefficient of determination $R^2 = 0.96$.

5.2.2 Cell morphology

Micrographs of *A. cylindrica* filaments were captured with a Leica LMIL microscope (Leica Microsystems, IL, USA) connected to a CCD camera (Spot Insight Model 4.2, MI, USA). The cells constituting the filamentous cyanobacterium were assumed to be spherical. We considered N_f filaments and measured the diameter $(d_{s,i,j})_{1 \leq j \leq N_c}$ of N_c cells for each filament “ i ”. The cell diameter was manually measured using the image analysis software ImageJ and taken as the maximum width across the cell in the direction perpendicular to the filament axis. For each of the four samples, at least 80 different *A. cylindrica* filaments were selected at random and the diameters of more than 14 cells per filament were measured, i.e., $N_f = 80$ and $N_c = 14$. Approximately 13 vegetative cells and 1 heterocysts were chosen randomly from each filament. This heterocyst frequency, defined as the ratio of the number of heterocysts to the total number of cells, was representative of the population of *A. cylindrica* in the samples.

As previously discussed, *A. cylindrica* filaments can be treated, as a first order approximation, as infinitely long cylinders given (i) their large size parameter $\chi_s \geq 10$, (ii) their filamentous morphology, (iii) the quasi-sphericity of their heterocysts and vegetative cells, and (iv) their relatively narrow size distribution. The diameter $d_{c,eq,i}$ of the volume-equivalent cylinder of filament “ i ” can be expressed in terms of individual cell diameters as

$$d_{c,eq,i}^2 = \frac{\sum_{j=1}^{N_c} \frac{2}{3} d_{s,i,j}^3}{\sum_{j=1}^{N_c} d_{s,i,j}} \quad \text{with} \quad i = 1, 2, \dots, N_f \quad (5.2)$$

These measurements led to the cylinder size distribution $f(d_{c,eq})$ defined as the number of

equivalent cylinders having diameters between $d_{c,eq}$ and $d_{c,eq} + dd_{c,eq}$.

5.2.3 Radiation characteristics measurements

5.2.3.1 Assumptions

The following assumptions were made in measuring the average mass absorption and scattering cross-sections and the scattering phase function of *A. cylindrica*: (1) the microorganisms were well mixed and randomly oriented, (2) single scattering prevailed due to the low biomass concentrations considered, (3) the scattering phase function had azimuthal symmetry and was only a function of polar angle θ , (4) the scattering phase function was assumed to be constant over the PAR region [115], and (5) the scattering cross-section of the cyanobacteria at 750 nm remains constant throughout the growth phase. The latter assumption constitutes the basis for measuring the temporal evolution of mass concentration X from OD measurements and Equation (5.1).

5.2.3.2 Scattering phase function

The scattering phase function was measured with a polar nephelometer at 633 nm. The experimental setup, data analysis, and validation with latex microspheres and glass fibers were reported in detail by Berberoğlu *et al.* [114, 115] and need not be repeated. Due to obstruction from the probe, scattering angles θ beyond 170° in the backward direction were not reported.

5.2.3.3 Absorption and scattering coefficients

Normal-normal transmittance measurements were performed in 1 cm pathlength cuvettes using a UV-VIS spectrophotometer (Shimadzu, USA, Model UV-3103PC) from 400 to 750 nm with 1 nm spectral resolution. The extinction coefficient of the suspension β_λ was obtained from these measurements after correcting for forward scattering by the suspension [115].

Indeed, *A. cylindrica* scatters radiation mainly in the forward direction due to its large size parameter. A fraction of this forwardly scattered radiation was collected by the detector through its finite acceptance angle. It can be estimated from the previously measured scattering phase function and subtracted from the measured transmitted signal [115,124].

The absorption coefficient κ_λ was determined from normal-hemispherical transmittance measurements performed with an integrating sphere (ISR-3100 by Shimadzu, USA) and the above mentioned spectrophotometer at wavelengths from 400 to 750 nm [114]. However, imperfect reflections in the integrating sphere and the geometry of the setup prevented a portion of the scattered radiation from being collected by the detector. Thus, the measurements were corrected based on the fact that *A. cylindrica* does not absorb at 750 nm [145] to obtain the absorption coefficient of the suspension κ_λ according to the procedure described in Ref. [115,124]. Finally, the scattering coefficient was obtained from $\sigma_{s,\lambda} = \beta_\lambda - \kappa_\lambda$.

Absorption and scattering coefficients were normalized by the mass concentration X estimated from OD measurements at 750 nm to obtain the average mass absorption and scattering cross-sections $\bar{A}_{abs,\lambda}$ and $\bar{S}_{sca,\lambda}$ according to Equation (2.6). Measurements were performed for three different mass concentrations on day 6, 9, 12, and 14. This was meant to assess experimental repeatability as well as to estimate the experimental uncertainties associated with $\bar{A}_{abs,\lambda}$ and $\bar{S}_{sca,\lambda}$.

5.2.4 Effective optical properties of filamentous cyanobacteria

The average absorption and scattering cross-sections $\bar{C}'_{abs,\lambda}$ and $\bar{C}'_{sca,\lambda}$ per unit length of filament (in m²/m) can be determined from the measured average mass absorption and scattering cross-sections $\bar{A}_{abs,\lambda}$ and $\bar{S}_{sca,\lambda}$ using the following relationships adapted to filamentous

cyanobacteria from Ref. [49],

$$\bar{C}'_{abs,\lambda} = \bar{A}_{abs,\lambda} \rho_{dm} (1 - x_w) \left(\frac{\pi}{6N_f} \sum_{i=1}^{N_f} \sum_{j=1}^{N_c} d_{s,i,j}^2 \right) \quad (5.3)$$

and

$$\bar{C}'_{sca,\lambda} = \bar{S}_{sca,\lambda} \rho_{dm} (1 - x_w) \left(\frac{\pi}{6N_f} \sum_{i=1}^{N_f} \sum_{j=1}^{N_c} d_{s,i,j}^2 \right)$$

Here, ρ_{dm} is the dry mass density of microorganism taken as 1350 kg/m³ [116]. The average volume fraction of water in the cells, denoted by x_w , was taken as either 0.75 or 0.85 considered to be the limits of its observed range [116]. The last term in parenthesis represents the average volume per unit length of the filaments of *A. cylindrica*.

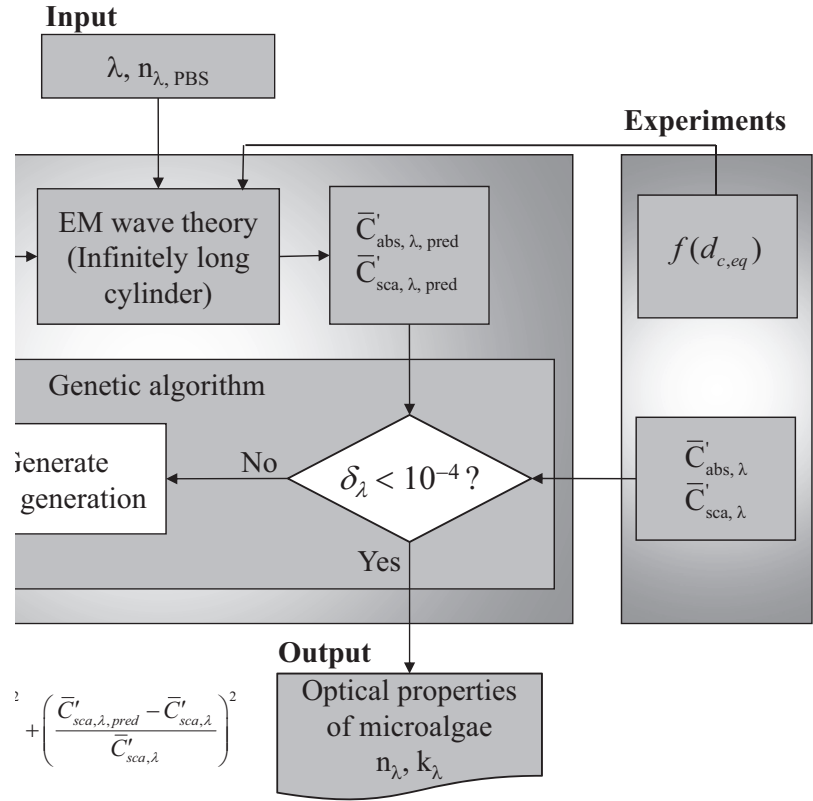


Figure 5.2: Block diagram of the procedure used to retrieve the refractive index n_{λ} and absorption index k_{λ} from the measured absorption and scattering cross-sections per unit length $\bar{C}'_{abs,\lambda}$ and $\bar{C}'_{sca,\lambda}$ at a given wavelength λ for volume-equivalent diameter distribution $f(d_{c,eq})$. Here, P=100 individuals per generation for a maximum of 500 generations.

The approach developed by Lee *et al.* [146] for spherical polydisperse scatterers was extended to retrieve the spectral refraction index n_λ and absorption index k_λ of filamentous cyanobacteria. Filaments were assumed to be randomly oriented, homogeneous, and infinitely long cylinders with volume-equivalent diameter distribution $f(d_{c,eq})$. Figure 7.2 presents the schematic diagram used to retrieve n_λ and k_λ of *A. cylindrica* from (i) the wavelength, (ii) the spectral refraction index $n_{\lambda,PBS}$ of the surrounding PBS medium reported in Ref. [100], (iii) the volume-equivalent cylinder diameter distribution $f(d_{c,eq})$ of *A. cylindrica*, and (iv) the average absorption and scattering cross-sections per unit length $\bar{C}'_{abs,\lambda}$ and $\bar{C}'_{sca,\lambda}$ determined from experimental measurements of $\bar{A}_{abs,\lambda}$ and $\bar{S}_{sca,\lambda}$ using Equation (5.3). The electromagnetic wave theory predicting the absorption and scattering cross-sections of infinitely long cylinders [60, 147] was used as the forward method. The objective function δ_λ for each wavelength was defined as the sum of squared relative errors between the predicted average cross-sections denoted by $\bar{C}'_{abs,\lambda,pred}$ and $\bar{C}'_{sca,\lambda,pred}$ and those measured experimentally $\bar{C}'_{abs,\lambda}$ and $\bar{C}'_{sca,\lambda}$ [Equation (5.3)], i.e.,

$$\delta_\lambda = \left(\frac{\bar{C}'_{abs,\lambda,pred} - \bar{C}'_{abs,\lambda}}{\bar{C}'_{abs,\lambda}} \right)^2 + \left(\frac{\bar{C}'_{sca,\lambda,pred} - \bar{C}'_{sca,\lambda}}{\bar{C}'_{sca,\lambda}} \right)^2 \quad (5.4)$$

The genetic algorithm PIKAIA [96] was employed to find the pair (n_λ, k_λ) that minimizes δ_λ . PIKAIA was used with 500 generations and a population of 100 individuals per generation. The refraction and absorption indices n_λ and k_λ were retrieved at 71 individual wavelengths between 400 and 750 nm.

5.3 Results and Discussions

Four samplings were performed on the 6th, 9th, 12th, and 14th day of *A. cylindrica* grown in batch mode. The corresponding mass concentrations were $X_1 = 0.086$ kg/m³, $X_2 = 0.108$ kg/m³, $X_3 = 0.151$ kg/m³, and $X_4 = 0.171$ kg/m³, respectively. Results from duplicate experiments fell within one another's experimental uncertainty. After 15 days of growth, the cyanobacterium culture started forming colonies and individual filaments could not be

suspended as independent and randomly oriented scatterers.

Moreover, based on the previous elemental analysis, the biomass concentrations leading to P and K limitation were never reached as the mass concentration did not exceed $X_4 = 0.171 \text{ kg/m}^3$. Thus, the cultures did not suffer from limitations in P or K. Note that Brownell and Nicholas [148] achieved *A. cylindrica* mass concentrations ranging from 0.4 to 1.1 kg/m^3 after 13 days of growth in nitrate deficient medium. These mass concentrations were significantly larger than the concentration reached in the present study. The difference can be attributed to the fact that the cyanobacteria in Ref. [148] were grown under irradiance of 7,000 lux instead of 3,000 lux in the present study.

5.3.1 Size distribution and heterocyst frequency

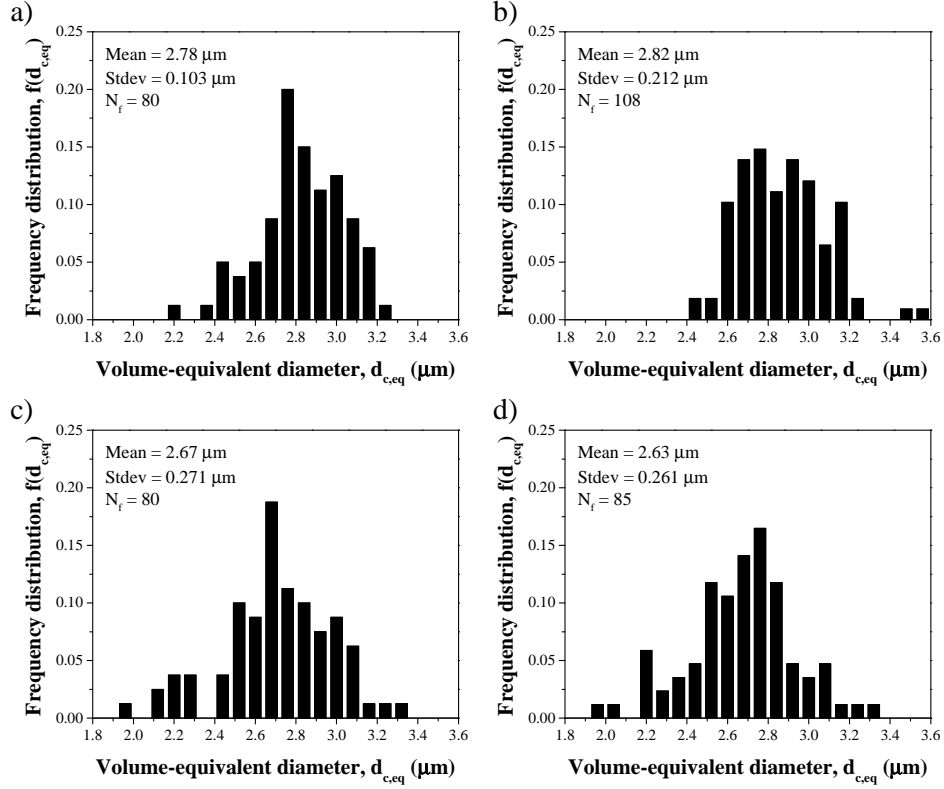


Figure 5.3: Histograms of volume-equivalent diameter distribution $f(d_{c,eq})$ of *A. cylindrica* filaments for Samples 1, 2, 3, and 4 at concentrations (a) $X_1 = 0.086 \text{ kg/m}^3$, (b) $X_2 = 0.108 \text{ kg/m}^3$, (c) $X_3 = 0.151 \text{ kg/m}^3$, and (d) $X_4 = 0.171 \text{ kg/m}^3$ obtained from more than 1120 cells for each sample.

The volume-equivalent diameter distribution $f(d_{c,eq})$ of *A. cylindrica* was estimated based on Equation (5.2) from more than $N_f \times N_c = 1120$ cells for each sample. Figures 5.3a through 5.3d show histograms of the volume-equivalent diameter distributions $f(d_{c,eq})$ with bin size of $0.8 \mu\text{m}$ for Samples 1, 2, 3, and 4 and the mean diameter and standard deviation computed from diameter measurements of both vegetative cells and heterocysts. It is evident that the diameter distribution did not vary significantly from one sample to another. The mean diameter of the four samples fell within one standard deviation of one another and was equal to $2.7 \mu\text{m}$.

Nitrogen limitation can affect the heterocyst frequency of *A. cylindrica* and therefore the size distribution since heterocysts tend to be larger than vegetative cells. Here, the heterocyst frequency was measured as 4.0%, 4.4%, 4.9%, and 5.1% for Sample 1, 2, 3, and 4, respectively. This increase in heterocyst frequency and the composition of BG-11(N) medium suggests that the culture suffered from nitrogen limitation from the beginning of the growth. However, this was not sufficient to affect the size distribution $f(d_{c,eq})$.

5.3.2 Scattering phase function

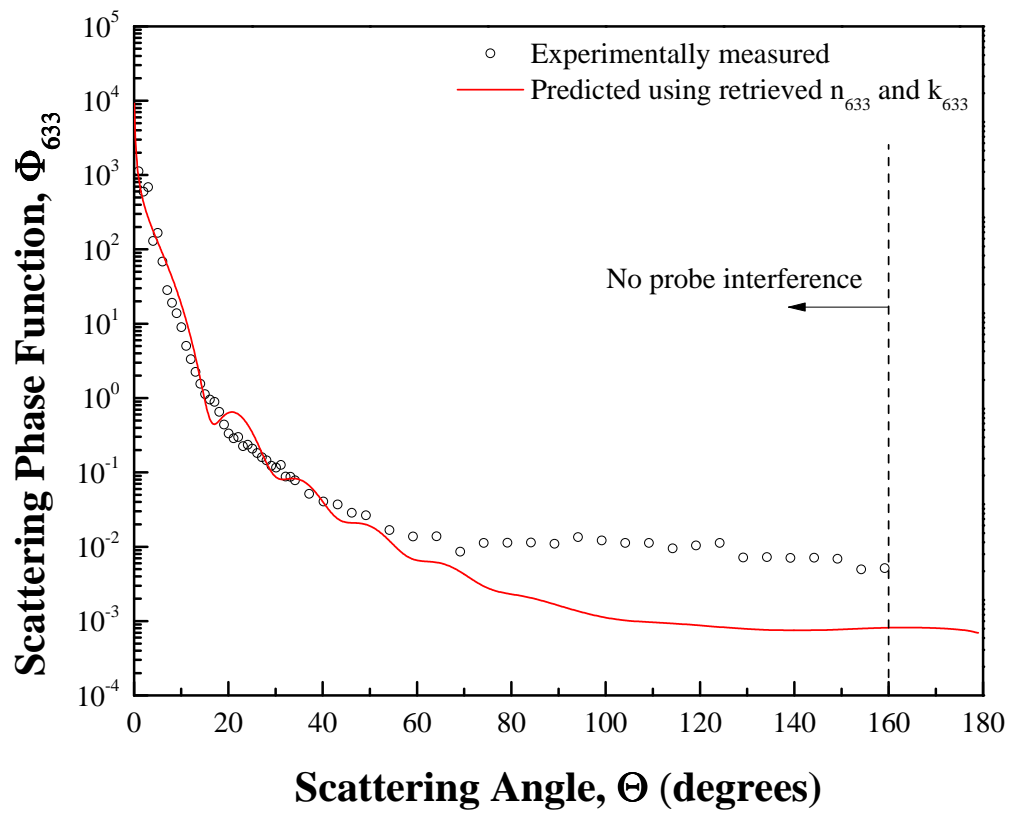


Figure 5.4: Scattering phase function of *A. cylindrica* at 633 nm measured experimentally using a polar nephelometer and predicted using the retrieved values of n_{633} and k_{633} for Sample 3 with $x_w = 0.75$.

Figure 7.9 shows the experimentally measured scattering phase function of *A. cylindrica* at 633 nm. Scattering by the microorganisms was strongly in the forward direction. For the sake of completeness and for comparison with the literature, the asymmetry factor was estimated to be $g_{633} = 0.985$ [Equation (2.10)]. This large value was expected due to the large diameter and length of *A. cylindrica* filaments compared with the wavelength of light in the PAR region resulting in large size parameter χ_s in excess of 10. Note that the asymmetry factor for *A. variabilis* was reported as $g_{633} = 0.975$ [114].

5.3.3 Mass absorption and scattering cross-sections

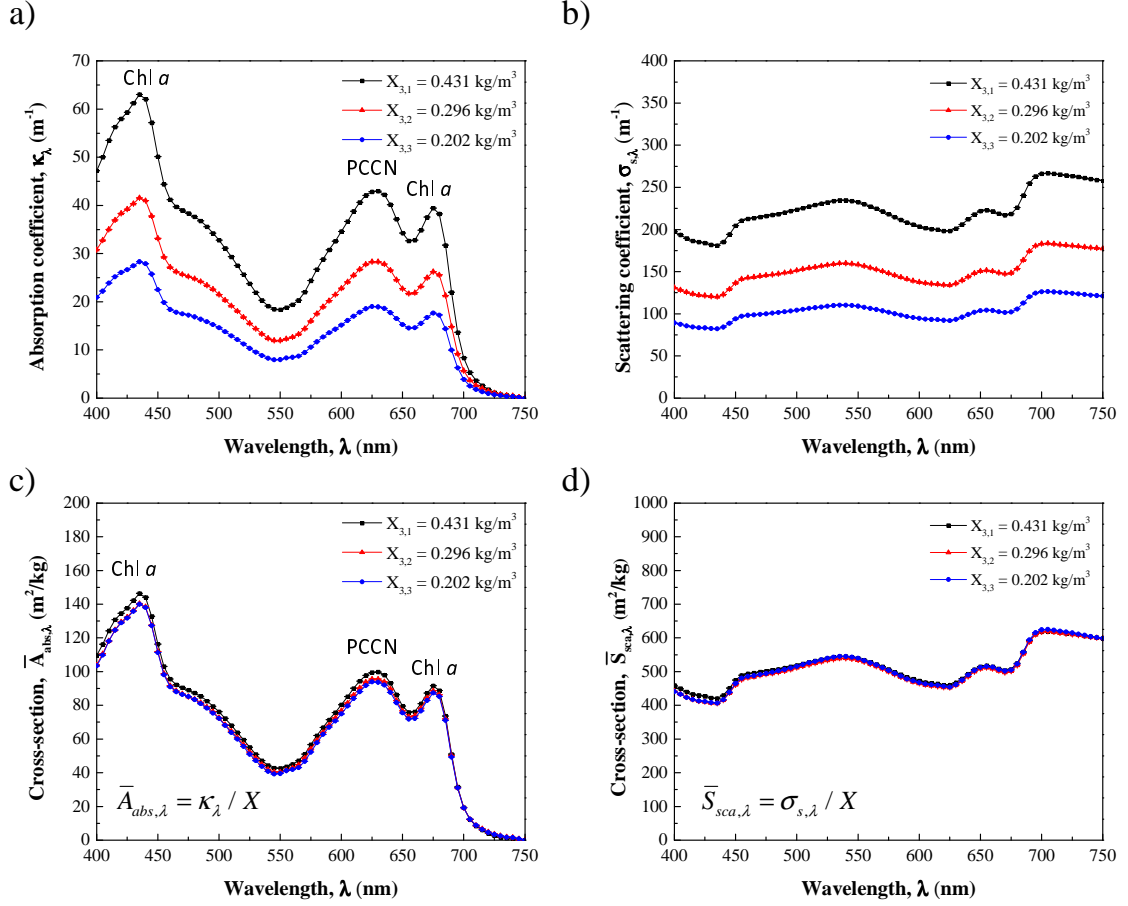


Figure 5.5: (a) Absorption coefficient κ_λ , (b) scattering coefficient $\sigma_{s,\lambda}$, (c) average mass absorption cross-section $\bar{A}_{abs,\lambda} = \kappa_\lambda / X$, and (d) average mass scattering cross-section $\bar{S}_{sca,\lambda} = \sigma_{s,\lambda} / X$ from 400 to 750 nm of *A. cylindrica* in Sample 3 for mass concentrations $X_{3,1} = 0.431$, $X_{3,2} = 0.296$, and $X_{3,3} = 0.202$ kg/m³.

Figures 5.5a and 5.5b respectively show the spectral absorption κ_λ and scattering $\sigma_{s,\lambda}$ coefficients measured in the spectral range from 400 to 750 nm for Sample 3 collected after 12 days of growth for mass concentrations $X_{3,1} = 0.431$ kg/m³, $X_{3,2} = 0.296$ kg/m³, and $X_{3,3} = 0.202$ kg/m³. These concentrations were achieved by suspending the cells in PBS from sample concentration $X_3 = 0.151$ kg/m³. Each data point represents the arithmetic mean of κ_λ and $\sigma_{s,\lambda}$ measured three times for each concentration $(X_{3,i})_{1 \leq i \leq 3}$ and the error bars corre-

spond to 95% confidence interval. It is evident that the scattering and absorption coefficients increased with increasing mass concentrations. In addition, *A. cylindrica* absorbed mainly in the spectral region from 400 to 700 nm with peaks (i) at 436 and 676 nm corresponding to absorption by Chl *a* [4], (ii) at 630 nm corresponding to PCCN [140], and (iii) a shoulder around 480 nm corresponding to absorption by PSC and PPC [4]. Small dips were observed in the scattering coefficient $\sigma_{s,\lambda}$ around wavelengths corresponding to the absorption peaks.

Figures 5.5c and 5.5d show the average mass absorption $\bar{A}_{abs,\lambda}$ and scattering $\bar{S}_{sca,\lambda}$ cross-sections in the spectral range from 400 to 750 nm after normalizing κ_λ and $\sigma_{s,\lambda}$ by their respective mass concentrations $(X_{3,i})_{1 \leq i \leq 3}$ according to Equation (2.6). It is evident that the three datasets collapsed on a single line. Van de Hulst [125] recommended that a “simple and conclusive test for the absence of multiple scattering” consists of verifying that the scattering intensity is directly proportional to particle concentration. Therefore, the experimental measurements confirm that single and independent scattering prevailed (Assumption 2) and that absorption and scattering were linear processes, as suggested by Equation (2.6). In addition, scattering dominated over absorption at all wavelengths between 400 and 750 nm. Similar results were obtained for the absorption and scattering coefficients κ_λ and $\sigma_{s,\lambda}$ and for the average mass absorption and scattering cross-sections $\bar{A}_{abs,\lambda}$ and $\bar{S}_{sca,\lambda}$ measured at other times during the growth.

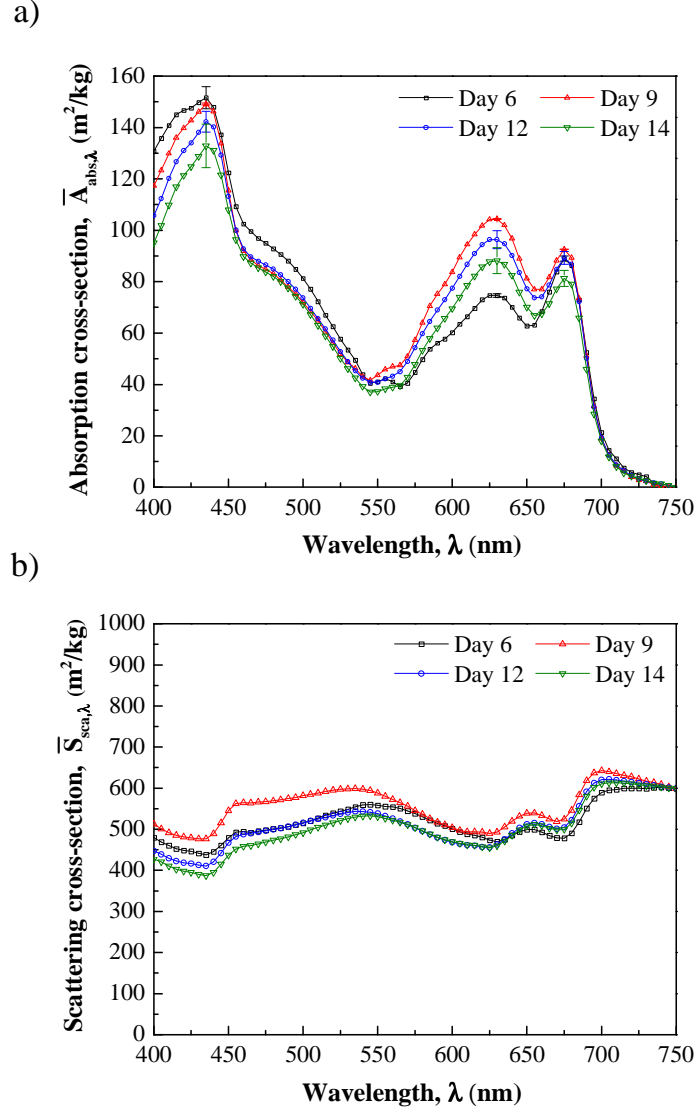


Figure 5.6: Average mass (a) absorption $\bar{A}_{abs,\lambda}$ and (b) scattering cross-sections $\bar{S}_{sca,\lambda}$ from 400 to 750 nm of *A. cylindrica* for Samples 1, 2, 3, and 4 collected after day 6, 9, 12, and 14, respectively.

Figure 5.6 presents the average (a) mass absorption $\bar{A}_{abs,\lambda}$ and (b) scattering $\bar{S}_{sca,\lambda}$ cross-sections over the PAR region for Samples 1 to 4 collected after 6, 9, 12, and 14 days during batch culture. From day 6 (Sample 1) to day 9 (Sample 2), the absorption cross-section at 480 nm $\bar{A}_{abs,480}$ decreased but did not change significantly afterwards. Simultaneously, both

$\bar{A}_{abs,630}$ and $\bar{A}_{abs,676}$ increased. This can be attributed to the adaptation of the microorganisms to the decreasing average fluence rate in the culture bottle caused by increasing biomass concentrations. As a response, they decrease their PPC concentration and increase their Chl *a* and PCCN concentrations [110]. After day 9, the absorption cross-section $\bar{A}_{abs,630}$ corresponding to phycocyanin decreased significantly while $\bar{A}_{abs,676}$ decreased slightly. The sharp decrease in $\bar{A}_{abs,630}$ can be attributed to the selective degradation of phycocyanin caused by the nitrogen deficient conditions prevailing after 9 days. In fact, phycocyanin degradation has been suggested as a mechanism to provide endogenously amino acids for the maintenance and synthesis of nitrogenase [149, 150]. This degradation was found to be selective and did not affect significantly the cells' Chl *a* content in other cyanobacteria including (i) unicellular [150] and (ii) filamentous non-heterocystous [151]. Finally, note that the absorption peak at 436 nm was affected by both Chl *a* and carotenoids and decreased continuously from day 6 to 14. This can be explained by the successive decrease in carotenoid concentration between day 6 and 9 and in Chl *a* concentration from day 9 to 14.

Moreover, the average mass scattering cross-sections for all samples were identical at 750 nm. This was due to Assumption 5 stating that $\bar{S}_{sca,750}$ remained constant during the growth. Hence, the same mass calibration curve [Equation (5.1)] was used to determine X for all samples. This method of estimating the mass concentration of photosynthetic microorganisms has been widely used [152]. However, the cells of the cyanobacterium undergo compositional and morphological changes during its growth phase which may cause $\bar{S}_{sca,\lambda}$ to vary over time. Overall, the relative difference in $\bar{S}_{sca,\lambda}$ among the four samples was less than 13 % over the entire PAR region. This relatively small difference suggests that assuming $\bar{S}_{sca,750}$ to be constant did not introduce significant errors in the measurements of X with respect to time from OD measurements at 750 nm. In other words, changes in cell composition and heterocyst frequency were not sufficient to affect significantly the scattering cross-section.

Finally, Berberoğlu *et al.* [114] reported the mass absorption and scattering cross-sections of filamentous *Anabaena variabilis* grown in ATCC medium 616 under 2,000-3,000 lux of

fluorescent white light. Comparatively, *A. cylindrica* featured values of $\bar{A}_{abs,\lambda}$ and $\bar{S}_{sca,\lambda}$ that were approximately twice smaller than those of *A. variabilis* for all wavelengths in the PAR region. This is likely due to the fact that *A. variabilis* had larger cell diameter around 5 μm compared with 2.7 μm for *A. cylindrica*. It could also be due to different pigment concentrations even though both species are filamentous cyanobacteria from the same genus.

5.3.4 Effective optical properties

5.3.4.1 Validation of the inverse method

The scattering cross-sections of 99% silica glass fibers more than 1 mm long supplied by OMEGA Engineering, Inc., USA (Part No: XS-K-24SLE) were measured between 400 and 725 nm using the same experimental setup and procedure as those used to measure $\bar{C}'_{abs,\lambda}$ and $\bar{C}'_{sca,\lambda}$ for *A. cylindrica*. The fiber size distribution was also measured using 113 fibers and varied between 4-8 μm in diameter with mean diameter of 5.88 μm and standard deviation 0.65 μm . Note that in the visible part of the spectrum, the absorption index of silica glass is less than 2×10^{-7} and was taken as $k_\lambda = 0$ [153]. The real part of the complex index of refraction n_λ of the glass fibers was retrieved over the PAR region using the inverse method previously described. The results were compared with predictions from the following three-term Sellmeier equation, valid between 0.21 and 6.7 μm [153, 154],

$$n_\lambda^2 = 1 + \frac{0.6961663\lambda^2}{\lambda^2 - (0.0684043)^2} + \frac{0.4079426\lambda^2}{\lambda^2 - (0.1162414)^2} + \frac{0.8974794\lambda^2}{\lambda^2 - (9.896161)^2} \quad (5.5)$$

where λ is expressed in μms . The maximum and average relative differences over the PAR region were 4% and 2%, respectively (see Supplementary Materials). These results validate both the experimental and theoretical methods used in this study.

5.3.4.2 *A. cylindrica*

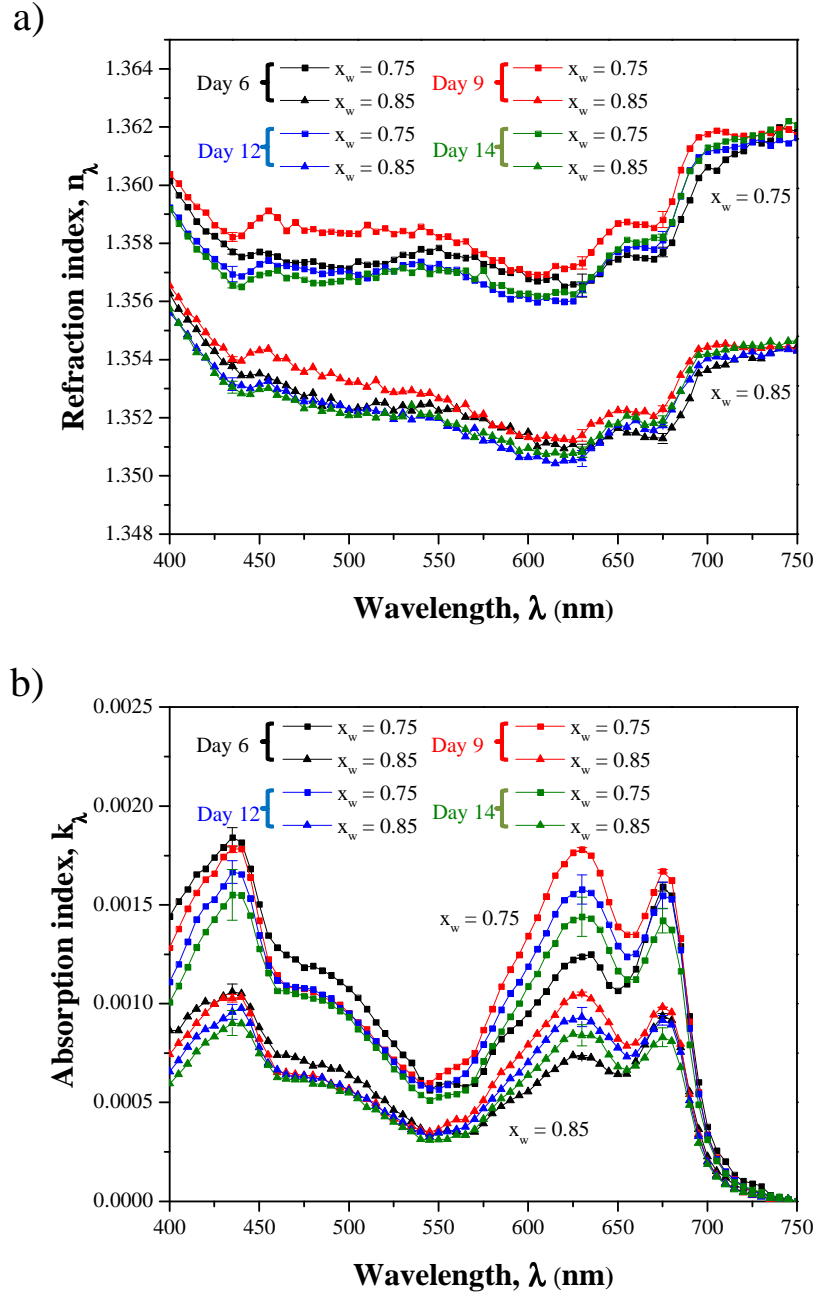


Figure 5.7: Retrieved (a) refractive n_λ and (b) absorption k_λ indices between 400 to 750 nm for *A.cylindrica* assuming water mass fraction to be $x_w = 0.75$ or 0.85 for Samples 1, 2, 3, and 4 collected after day 6, 9, 12, and 14, respectively.

Figure 7.11 shows (a) the refraction index n_λ and (b) the absorption index k_λ of *A. cylindrica* between 400 and 750 nm for Samples 1, 2, 3, and 4 retrieved from (i) the measured average mass absorption and scattering cross-sections, (ii) the volume-equivalent cylinder diameter distribution $f(d_{c,eq})$, and (iii) for water mass fractions x_w equal to 0.75 or 0.85. The error bars were estimated from error propagation analysis at wavelengths 436, 630, and 676 nm.

First, it is worth noting that n_λ and k_λ , retrieved for each of the 71 individual wavelength considered, were continuous functions of wavelengths. Second, k_λ featured peaks at 436, 630, and 676 nm corresponding to *in vivo* absorption peaks Chl *a* and PPCN, the pigments of *A. cylindrica* [4, 139]. Third, the values retrieved for n_λ and k_λ were within the ranges of those found for microalgae [99, 146] and other cyanobacteria previously reported in the literature [54, 99]. These results could not have been guessed *a priori* as they were not intrinsic consequences of the inverse method which retrieved n_λ and k_λ for each wavelength independently. This further brings confidence in the inverse method.

The refraction index n_λ retrieved did not vary significantly with time. In addition, the values obtained with $x_w = 0.75$ were less than 1% larger than that obtained with $x_w = 0.85$ for all samples and across the PAR region. In other words, n_λ was not sensitive to water mass fraction x_w . Small dips in n_λ were observed around wavelengths corresponding to absorption peaks in k_λ . This can be attributed to oscillator resonances predicted from optical constant theory such as the Lorenz model [60] or the Ketteler-Helmholtz theory [54], for example. By contrast, the absorption index k_λ displayed large sensitivity to the chosen value of x_w .

Finally, the scattering phase function $\Phi_{T,\lambda}(\hat{\mathbf{s}}_i, \hat{\mathbf{s}})$ in the PAR region was computed by (i) treating *A. cylindrica* as infinitely long and randomly oriented cylinders with volume-equivalent size distribution and (ii) using the values of n_λ and k_λ retrieved assuming water mass fraction x_w of 0.75 and 0.85. The associated asymmetry factor at 633 nm for samples 1-4 was found to range between 0.983 and 0.985. These results are in good agreement with the value of 0.985 obtained experimentally, as illustrated in Figure 7.9. Note that at scattering angle Θ larger than 60° , the experimentally measured phase function showed

significant differences with the predicted phase function. This may be attributed to the fact that filamentous *A. cylindrica* were treated as infinitely long cylinders. In fact, similar differences in the phase functions of linear chains of spheres and volume-equivalent infinitely long cylinders with large size parameters can be observed in data reported by Lee and Pilon [134]. Note also that, for the microorganism considered, the size parameter is large, scattering is strongly forward, and only a small amount of energy is contained in the radiation scattered in scattering angles beyond 60° . The asymmetry factor and the scattering phase function varied very slightly from one sample to another and with the choice of water mass fraction x_w . In fact, they depended mainly on the size distribution and on the index of refraction which remained nearly constant during the course of the experiments. Finally, the predicted scattering phase function was practically independent of wavelength over the PAR region. These results confirmed Assumption 4 used to retrieve the absorption and scattering cross-sections.

5.4 Chapter summary

This chapter presented the mass absorption and scattering cross-sections and the complex index of refraction of *A. cylindrica* from 400 to 750 nm at different times during batch growth in nitrate-free medium under 3,000 lux of white fluorescent light. An inverse method was developed to retrieve the real and imaginary parts of the complex index of refraction from the measured scattering phase function and average mass scattering and absorbing cross-sections. It treated *A. cylindrica* filaments as homogeneous, randomly oriented, and infinitely long volume-equivalent cylinders. *A. cylindrica* scattered mainly in the forward direction due to its large size parameter. The absorption index and absorption cross-section showed distinct absorption peaks at 436 and 676 nm corresponding to chlorophyll *a* and at 480 and 630 nm corresponding to carotenoids and phycocyanin, respectively. Absorption peaks corresponding to Chl *a* and PCCN increased and those of PPC decreased from day 6 to 9 due to photoacclimation in response to low fluence rate in the PBR caused by increas-

ing biomass concentration. The absorption peaks corresponding to PCCN concentrations decreased sharply after day 9. This was attributed to degradation of phycocyanin as an endogenous nitrogen source to maintain and to synthesize nitrogenase enzyme during nitrogen starvation. This interpretation was corroborated by the simultaneous increase in heterocyst frequency. Finally, unlike the refraction index n_λ , k_λ varied during batch culture and was very sensitive to the water mass fraction x_w used in the inverse method. The results can be used to predict and optimize light distribution in photobioreactors growing *A. cylindrica* for wastewater treatment, ammonia, or hydrogen production. The methodology can also be applied to a wide range of scattering suspensions containing cylindrical scatterers.

CHAPTER 6

Absorption and scattering by bispheres, quadspheres, and circular rings of spheres and their equivalent coated spheres

This chapter demonstrated that the radiation characteristics of randomly oriented and optically soft bispheres, quadspheres, and circular rings of spheres, with either monodisperse or polydisperse monomers, can be approximated by an equivalent coated sphere with identical volume and average projected area. These results provide a rapid and accurate way of predicting the radiation characteristics of bispheres, quadspheres, and rings of spheres representative of various unicellular and multicellular cyanobacteria considered for producing food supplements, biofuels, and fertilizers. They could also be used in inverse methods for retrieving the monomers' optical properties, morphology, and/or concentration.

6.1 Introduction

While most diatoms and green microalgae exist in unicellular forms, cyanobacteria can be either unicellular or multicellular [128, 155]. For example, *Synechocystis sp.* is a unicellular cyanobacterium with a dumbbell shape. It was the first photosynthetic organism whose entire genome was sequenced [156]. It has been used as a model organism to study photosynthesis, pigment synthesis, carbon and nitrogen assimilation, lipid production, and other metabolic processes [156–159]. Figure 7.1a shows a micrograph of a population of free-floating *Synechocystis sp.* cells about 3 to 5 μm in length. Figure 7.1b shows a micrograph of *Synechocystis sp.* immediately after cell division into two morphologically identical daugh-

ter cells [160]. On the other hand, certain multicellular cyanobacteria such as *Anabaenopsis elenkinii* and *circularis* develop specialized cells called heterocysts that contain nitrogenase enzymes used for the biocatalytic reduction of atmospheric nitrogen into ammonia [161]. This special ability to fix atmospheric nitrogen makes these cyanobacteria potential producers of fertilizers [162]. In addition, they are capable of producing hydrogen under certain conditions [163,164]. Figures 7.1c and 7.1d show the micrographs of *A. elenkinii* and *circularis*, respectively. The cyanobacterium *A. elenkinii* consists of spheroidal vegetative cells with 4-5 μm minor diameter and 5-7 μm major diameter and nearly spherical heterocysts 3-4 μm in diameter. By contrast, the cyanobacterium *A. circularis* consists of aspherical vegetative cells and spherical heterocysts about 8-10 μm in diameter. These cells are arranged in a nearly circular ring and number between 10 and 25 cells per ring. The cultivation of photosynthetic microorganisms in photobioreactors (PBRs) exposed to sunlight has been studied extensively due to the above-mentioned applications. Photosynthetic microorganisms absorb photons in the photosynthetically active radiation (PAR) region ranging from 400 to 700 nm thanks to photosynthetic pigments such as chlorophylls and carotenoids [112]. They also scatter light due to the refractive index mismatch between the cells and the surrounding growth medium [113]. The economic viability of large-scale cultivation can be severely reduced by poor light penetration in dense microorganism cultures [2]. In order to design and operate PBRs with optimum light availability, it is essential to accurately predict light transfer in the culture [2,50]. To do so, the spectral radiation characteristics of the photosynthetic microorganisms are necessary. They can be measured experimentally [2,114] or predicted numerically [49,56,165]. Experimental measurements can faithfully capture the effect of the microorganisms' size, shape, and polydispersity. However, they require expensive equipment and can be time consuming. Radiation characteristics of spherical photosynthetic microorganisms can be easily determined from the Lorenz-Mie theory [78]. Similarly, solutions of Maxwell's equations have also been developed for coated spheres [166] and infinitely long cylinders [125,167,168]. The radiation characteristics of particles with more complex and irregular shapes can be predicted numerically using (i) the T-matrix method [169–172], (ii) the

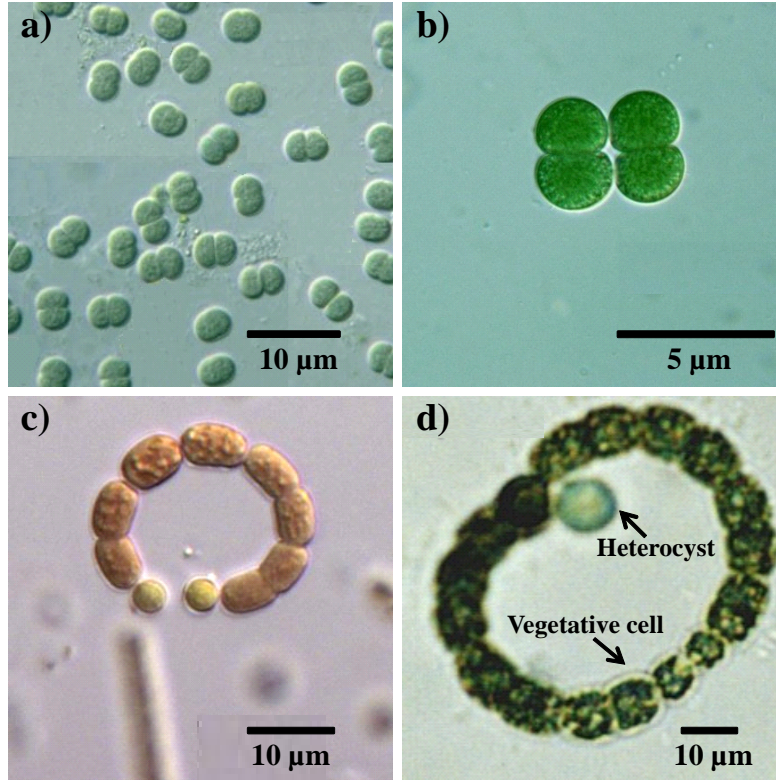


Figure 6.1: Micrographs of cyanobacteria: (a) free floating *Synechocystis* sp., (b) *Synechocystis* sp. immediately after cell division, (c) *Anabaenopsis elenkinii*, and (d) *Anabaenopsis circularis*. Reproduced with permission from (a), (b) Prof. Yuuji Tsukii (Hosei University), (c) Dr. Seija Hällfors (University of Jyväskylä Biology Department) and (d) Dr. Roger Burks (University of California at Riverside), Prof. Mark Schneegurt (Wichita State University), and Cyanosite.

discrete-dipole approximation [173], and (iii) the finite-difference time-domain method [174], for example. However, numerical predictions can be complicated by the diverse and sometimes complex microorganism morphology. In addition, their large size compared with the radiation wavelength and their polydispersity require time-consuming and resource-intensive computations [175]. Finally, inverse methods used to retrieve the complex index of refraction and/or the morphology and/or the concentration of the microorganisms from experimental measurements require numerous iterations of an already time-consuming forward

problem [56, 176–178].

The present study aims to identify particles of simple shape with radiation characteristics equivalent to those of *Synechocystis sp.*, *A. elenkinii* and *circularis* and other microorganisms with similar morphologies. Such equivalent particle approximation could be computationally advantageous and practical for predicting light transfer in PBRs and for remote sensing applications provided that it can achieve an acceptable degree of accuracy [117, 176].

6.2 Background

6.2.1 Scattering matrix

The four Stokes parameters, I , Q , U , and V , forming the Stokes vector, are used to describe an electromagnetic wave in terms of its intensity, degree of polarization, and ellipsometric characteristics [171]. Upon single scattering by a particle of arbitrary shape and orientation, the Stokes vector of the incident radiation represented by $\mathbf{I}_{inc}(\hat{s}_i) = (I_{inc}, Q_{inc}, U_{inc}, V_{inc})^T$, is transformed into the Stokes vector of the scattered radiation at location \mathbf{r} , denoted by $\mathbf{I}_{sca}(\mathbf{r}, \hat{s}) = (I_{sca}, Q_{sca}, U_{sca}, V_{sca})^T$. These vectors are related by the 4×4 Mueller matrix $[\mathbf{Z}(\Theta)]$ according to [172]

$$\mathbf{I}_{sca}(\mathbf{r}, \hat{s}) = \frac{1}{r^2} [\mathbf{Z}(\Theta)] \mathbf{I}_{inc}(\hat{s}_i) \quad (6.1)$$

where r is the norm of the location vector \mathbf{r} . The scattering angle, denoted by Θ , corresponds to the angle between the incident and scattered directions, \hat{s}_i and \hat{s} , respectively.

For randomly oriented particles with a plane of symmetry, it is more convenient to use the normalized (or Stokes) scattering matrix $[\mathbf{F}(\Theta)]$ given by [171]

$$[\mathbf{F}(\Theta)] = \frac{4\pi}{C_{sca}} [\mathbf{Z}(\Theta)] \quad (6.2)$$

where C_{sca} is the scattering cross-section of the particle. When multiplied by the incident monochromatic energy flux, C_{sca} represents the total monochromatic power removed from the incident electromagnetic (EM) wave due to scattering [171]. Similarly, the absorption cross-section C_{abs} can be defined such that its product with the incident monochromatic

energy flux represents the total monochromatic power absorbed by the particle [171]. The overall extinction of the incident EM wave is due to both absorption and scattering and the extinction cross-section can be defined as $C_{ext} = C_{abs} + C_{sca}$.

The normalized scattering matrix $[\mathbf{F}(\Theta)]$ for a scattering particle with a plane of symmetry is a 4×4 matrix containing eight nonzero elements and six independent elements given by [171, 179]

$$[\mathbf{F}(\Theta)] = \begin{bmatrix} F_{11}(\Theta) & F_{12}(\Theta) & 0 & 0 \\ F_{12}(\Theta) & F_{22}(\Theta) & 0 & 0 \\ 0 & 0 & F_{33}(\Theta) & F_{34}(\Theta) \\ 0 & 0 & -F_{34}(\Theta) & F_{44}(\Theta) \end{bmatrix}$$

The element $F_{11}(\Theta)$ represents the scattering phase function normalized according to [171]

$$\frac{1}{4\pi} \int_{4\pi} F_{11}(\Theta) d\Omega = 1 \quad (6.3)$$

where Ω is the solid angle around the scattering angle Θ . The asymmetry factor is defined as [92]

$$g = \frac{1}{4\pi} \int_{4\pi} F_{11}(\Theta) \cos\Theta d\Omega \quad (6.4)$$

It is equal to 0 for isotropic scattering and -1 and 1 for purely backward and forward scattering, respectively [2]. The ratio $-F_{12}(\Theta)/F_{11}(\Theta)$ represents the degree of linear polarization of the scattered radiation when the particle is exposed to unpolarized incident radiation [180]. The ratio $F_{22}(\Theta)/F_{11}(\Theta)$ can be interpreted as a measure of the particle's deviation from a sphere [180]. The ratio $F_{34}(\Theta)/F_{11}(\Theta)$ indicates the amount of obliquely polarized light at 45° [180]. For spherical scatterers, $F_{22}(\Theta) = F_{11}(\Theta)$ and $F_{33}(\Theta) = F_{44}(\Theta)$ [180].

6.2.2 Heterogeneous and spheroidal particles

Despite the heterogeneous nature of photosynthetic microorganism cells, they have often been treated as homogeneous with some effective complex index of refraction [56, 113, 177, 181]. This assumption was validated by Quirantes and Bernard [56] who modeled single cell microalgae as coated spheres or coated spheroids to account for their complex intracellular

structures. These coated particles had core to particle volume ratios ranging from 0.4 to 1 and size parameters based on outer diameter up to a maximum value of 30. The outer coating was assumed to be non-absorbing and represented the cellular cytoplasm. By contrast, the inner core, representing the organelles and chloroplasts, was absorbing and featured a larger refractive index than the outer coating. The authors found that light absorption and scattering efficiency factors of a homogeneous sphere with volume-averaged complex index of refraction were similar to those of the coated sphere [56].

Moreover, Lee *et al.* [177] showed that the radiation characteristics of spheroidal unicellular microalgae were similar to those of spheres with identical surface area provided that their aspect ratio was less than 1.33. These observations suggest that typical microorganisms' cells, such as those shown in Figure 7.1, can be treated as homogeneous spheres with an effective complex index of refraction.

6.2.3 Aggregates of spherical monomers

The development of the superposition T-matrix method to predict absorption and scattering of electromagnetic waves by multi-sphere clusters was first motivated by the study of the interaction between radiation and carbonaceous soot particles modeled as aggregates of connected spheres (or monomers) a few nanometers in diameter [170]. It has also been used for a wide variety of applications [182] ranging from plasmon resonance in aggregates of gold [183] and silver [184] nanoparticles to the interpretation of solar radiation scattered by cometary dust [185] and filamentous cyanobacteria [117].

The method is based on the superposition solutions of Maxwell's equations where the electromagnetic (EM) field scattered by the entire aggregate of monomers is the sum of the EM fields scattered by each of the constituent monomer [186]. The EM field incident onto a monomer takes into account not only the incident EM field but also the scattered fields from all the other monomers of the aggregate [186]. The interacting fields is transformed into a system of sphere-centered equations for the scattering coefficients and inverted to

obtain the T-matrix [186]. Using an analytical rotation transformation rule to integrate the incident EM field over every propagation direction and polarization, the scattering $\langle C_{sca} \rangle$ and extinction $\langle C_{ext} \rangle$ cross-sections and scattering matrix elements of a randomly oriented aggregate of spheres can be obtained from operations on the T-matrix [186].

6.2.4 Equivalent scattering particles

Several studies have used equivalent particles with simple geometries and some effective complex index of refraction to approximate the radiation characteristics of nonspherical particles and aggregates of spherical monomers. Mengüç *et al.* [187] approximated irregularly-shaped pulverized coal particles as volume equivalent spheres in order to retrieve their effective complex index of refraction from experimental radiation characteristics measurements. The coal particles were assumed to be spherical and their mean diameters were measured using scanning electron microscopy so as to compute their volumes. Liou and Takano [188] compared the absorption and scattering cross-sections and asymmetry factor of cubes, hexagonal ice crystals, and irregular convex and concave particles with size parameters larger than 30 with those predicted by Lorenz-Mie theory for their volume or surface area equivalent spheres. The range of complex index of refraction used for the particles was representative of atmospheric particulates, i.e., carbon and water. The authors concluded that nonspherical particles have smaller asymmetry factors than their volume or surface area equivalent spherical counterparts. They also found that volume equivalent spheres had similar absorption cross-sections but smaller scattering cross-sections than the actual nonspherical particles. Kahnert *et al.* [189] computed the extinction and scattering cross-sections, the single-scattering albedo, and the asymmetry factor of ensembles of randomly oriented polyhedral prisms with different number of side facets, aspect ratios, and sizes. The authors compared these radiation characteristics with those of ensembles comprising solely of spheres, spheroids, or finite-length cylinders with the same complex index of refraction and identical volume or surface area distribution. They found that the best approximation was achieved using ensembles of volume equivalent spheres. Yang *et al.* [190] approximated various platonic particles as

equivalent spheres with identical (i) geometric dimension, (ii) surface area, (iii) volume, or (iv) volume-to-surface area ratio. The authors found that the volume equivalent spheres offered the best approximation for the extinction efficiency factor, single-scattering albedo, and scattering matrix elements of platonic particles. However, all these approximations still resulted in significant errors. In addition, the authors recommended that the absorption and scattering cross-sections should be used instead of the efficiency factors due to the difference of geometric cross-sections between the platonic particles and the equivalent spheres. Gordon [181] showed that approximating finite cylinders as volume equivalent spheres resulted in large errors in the scattering efficiency factor but good agreement in the absorption efficiency factor.

Latimer [191] experimentally measured the extinction coefficients at 474 nm of randomly oriented fractal aggregates of 2 to 128 spherical latex particles in water. The author found that the aggregates could be approximated as coated spheres whose core and shell had the same complex index of refraction as water and latex, respectively. The volume of the coating was taken as the total volume of the latex particles constituting the aggregates while the volume of the core was taken as that of “the spaces between the particles” derived from fractal theory. While Latimer’s results showed good agreement between the radiation measurements of the latex particles and the theoretical predictions for the equivalent coated spheres, his choice of using only five discrete bins to represent the entire monomer size distribution may introduce significant errors. Tien and Drolen [192] computed the absorption and scattering cross-sections of soot aggregates consisting of 2 to 136 spherical monodisperse monomers with size parameter ranging from 0.05 to 0.2, refractive index ranging from 1.5 to 2.2, and absorption index ranging from 0 to 2.6. These monomers were aggregated either in straight chains or spheroidal, ellipsoidal, or cube-like clusters. They found that a volume equivalent sphere with the same complex index of refraction as the monomers gave similar absorption and scattering cross-sections as the soot aggregate. Recently, Lee and Pilon [117] showed that the absorption and scattering cross-sections per unit length and asymmetry factor of randomly oriented linear chains of optically soft spheres with size parameter ranging from

0.01 to 10, could be approximated as that of randomly oriented, volume equivalent, and infinitely long cylinders provided that the number of spheres in the chain was sufficiently large. However, this approximation was not valid for the scattering matrix elements.

Light transfer in homogeneous absorbing, scattering, and non-emitting microorganism suspensions, such as those found in photobioreactors (PBRs), is governed by the radiative transfer equation (RTE) [2]. In PBRs, the microorganisms are typically uniformly distributed and randomly oriented thanks to bubble sparging or stirring, for example [193]. The absorption and scattering cross-sections as well as the scattering phase function of these randomly oriented microorganisms are necessary input parameters to solve the RTE [2]. Unfortunately, cyanobacteria such as those showed in Figure 7.1 have very complex morphologies and large size parameters. Accurately predicting their radiation characteristics would require large amounts of time and computational resources. Therefore, the present study aims to demonstrate that photosynthetic microorganisms, such as those shown in Figure 7.1, can be approximated by some equivalent particle with a simple geometry. The effects of the cells' complex index of refraction and polydispersity were also investigated.

6.3 Analysis

6.3.1 Problem statement

First, actual cyanobacteria shown in Figure 7.1 were represented by idealized aggregates of optically soft and homogeneous spherical monomers. Figure 7.2a shows a bisphere consisting of two identical adjoining spheres of radius r_s representing the dumbbell-shape of *Synechocystis sp.* cells (Figure 7.1a). Similarly, Figure 7.2b shows a quadsphere modeling the morphology of *Synechocystis sp.* cells immediately after cell division (Figure 7.1b). Finally, Figures 7.2c and 7.2d show circular rings of spheres with an arbitrary number N_s of monomers representing filamentous cyanobacteria such as *A. elenkinii* and *A. circularis* (Figures 7.1c and 7.1d).

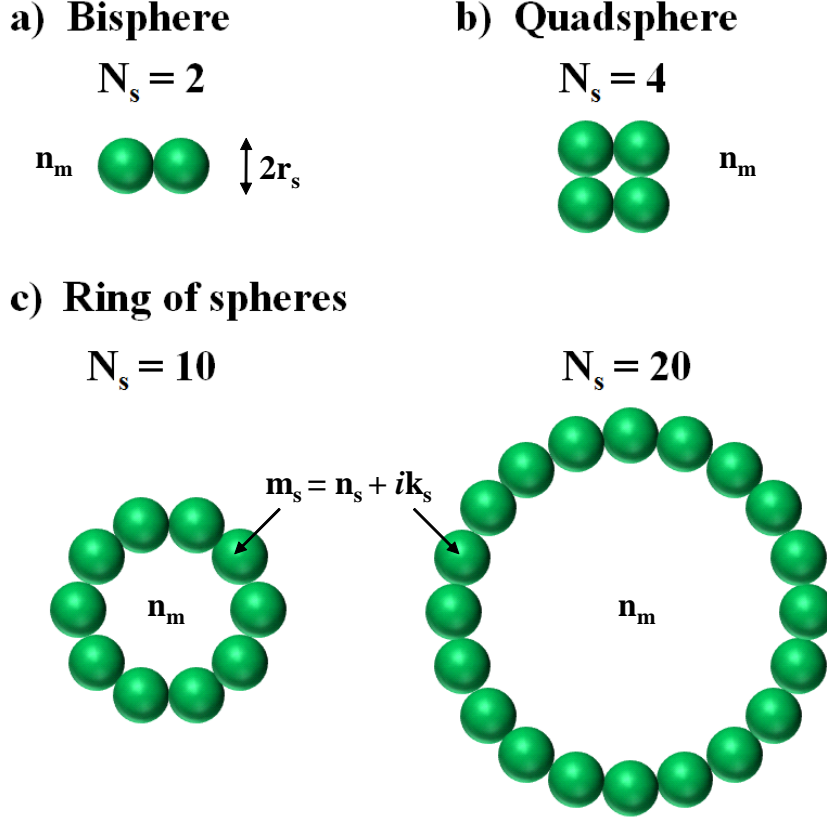


Figure 6.2: Schematic of simulated (a) bispheres, (b) quadspheres, and (c) rings of spheres with $N_s = 5$ and 10 monodisperse monomers of radius r_s and complex index of refraction $m_s = n_s + ik_s$ surrounded by a non-absorbing medium of refraction index n_m . These idealized aggregates are representative of the cyanobacteria shown in Figure 7.1.

Let us consider randomly oriented bispheres, quadspheres, and circular rings of spheres consisting of N_s monodisperse spherical monomers of radius r_s and complex index of refraction $m_s = n_s + ik_s$ where n_s and k_s are the refractive and absorption indices, respectively. The surrounding medium was assumed to be non-absorbing with refraction index $m_m = n_m$. The relative complex index of refraction of the monomers can be defined as $m = n + ik = m_s/n_m$. The size parameter of the monomers constituting the bispheres, quadspheres, and rings of spheres was defined as $\chi_s = 2\pi r_s/\lambda$ where λ is the wavelength of the incident radiation. In general, the radiation characteristics of bispheres, quadspheres, and rings of spheres depend

on (i) the aggregate morphology, (ii) the relative complex refraction index m , and (iii) the monomer number N_s and size parameter χ_s .

Previous studies [117, 181, 188, 189, 192] indicate that the equivalent particle should have the same volume as the aggregate to match their absorption cross-sections. This can be attributed to the fact that absorption is a volumetric phenomenon. On the other hand, scattering is due in part to the complex index of refraction mismatch across the interface between the aggregates' monomers and the surrounding medium. Thus, an equivalent particle with the same surface area as the aggregate could also have similar scattering cross-sections. Alternatively, the projected area is directly proportional to the amount of energy incident on the aggregates for a given aggregate orientation. Hence, matching the average projected area of the equivalent particle with that of the randomly oriented aggregate offers another alternative. The most common approach is to approximate a particle of complex shape or an aggregate of spherical monomers as an equivalent sphere [181, 189, 190]. However, a sphere is defined by a single geometric parameter: its radius. Thus, the equivalent sphere can only match either the volume, the surface area, or the average projected area of the aggregate. On the other hand, a coated sphere is defined by its inner and outer radii. Both can be adjusted to match two geometric characteristics of the aggregates such as its volume and its surface area or its volume and its average projected area.

In order to determine the best equivalent particle, the absorption and scattering cross-sections as well as the scattering matrix elements of the different possible equivalent spheres or coated spheres will be compared systematically with predictions by the superposition T-matrix method for randomly oriented bispheres, quadspheres, and rings of spheres. The monomers had size parameter χ_s ranging from 0.01 to 10, refractive index n_s varying between 1.37 and 2, and absorption index k_s from 0.0053 to 0.133. The surrounding medium was non-absorbing with refractive index $n_m = 1.33$. These values were representative of cyanobacteria suspended in growth medium and exposed to sunlight. The wavelength of incident light was taken as 676 nm corresponding to the absorption peak of Chlorophyll *a* [112]. Finally, the inner core of the equivalent coated sphere was assumed to have the same refractive index

n_m as the surrounding medium while the coating and the equivalent sphere were assumed to have the same complex index of refraction $m_s = n_s + ik_s$ as the monomers.

6.3.2 Methodology

6.3.2.1 Geometric consideration

The radius $r_{v,eq}$ of the volume equivalent sphere with the same volume as that of an aggregate consisting of N_s monomers of radius r_s can be expressed as

$$r_{v,eq} = r_s \sqrt[3]{N_s} \quad (6.5)$$

Similarly, the surface area and volume of coated spheres of outer $r_{s,eq,o}$ and inner $r_{s,eq,i}$ radii are equal to $4\pi r_{s,eq,o}^2$ and $4\pi(r_{s,eq,o}^3 - r_{s,eq,i}^3)/3$, respectively. Thus, the volume and surface area equivalent coated sphere, featuring the same volume and surface area as the aggregate, is such that $r_{s,eq,o}$ and $r_{s,eq,i}$ are given by

$$r_{s,eq,o} = r_s \sqrt{N_s} \quad \text{and} \quad r_{s,eq,i} = r_s \sqrt[3]{N_s^{3/2} - N_s} \quad (6.6)$$

Similarly, the outer $r_{\bar{A}_p,eq,o}$ and inner $r_{\bar{A}_p,eq,i}$ radii of the equivalent coated sphere with identical volume and average projected area \bar{A}_p as the randomly oriented aggregate can be written as

$$r_{\bar{A}_p,eq,o} = \sqrt{\frac{\bar{A}_p}{\pi}} \quad \text{and} \quad r_{\bar{A}_p,eq,i} = \sqrt[3]{\left(\frac{\bar{A}_p}{\pi}\right)^{3/2} - N_s r_s^3} \quad (6.7)$$

A priori, the average projected area \bar{A}_p depends on the number N_s and radius r_s of monomers in the aggregate. Figure 6.3 illustrates the projected area of a bisphere on the x-y plane when viewed along the z-axis. For a given orientation, the projected area $A_{p,b}$ of a bisphere is represented by the area enclosed by two intersecting circles and is given by

$$A_{p,b}(r_s, d) = 2\pi r_s^2 - 2r_s^2 \cos^{-1} \left(\frac{d}{2r_s} \right) + \frac{1}{2} d \sqrt{4r_s^2 - d^2} \quad (6.8)$$

where d is the distance between the centers of the two projected discs. This distance is given by $d = 2r_s \cos \phi$ where ϕ is the angle between the longitudinal axis of the bisphere and the

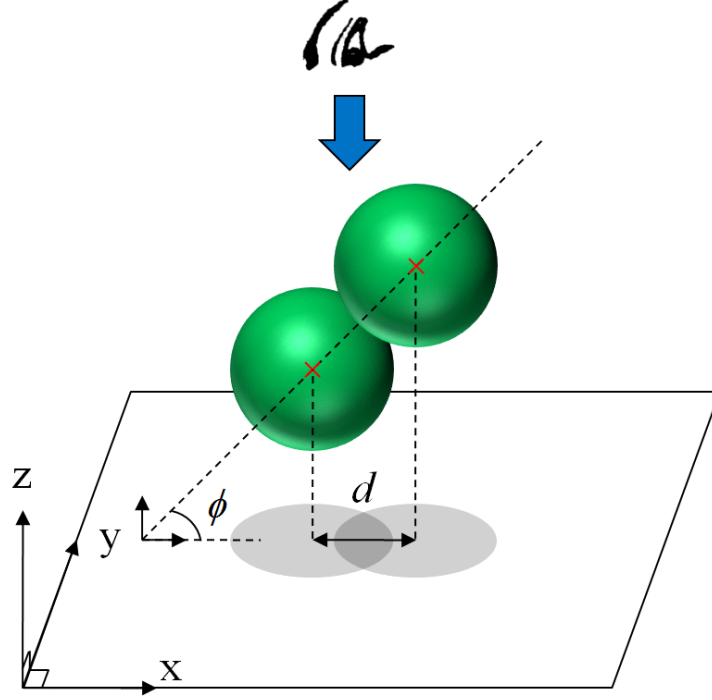


Figure 6.3: Schematic of the projected area of a bisphere onto the x-y plane when viewed along the z-axis.

x-y plane. For example, when the bisphere is viewed along its longitudinal axis, $\phi = \pi/2$ or $-\pi/2$. Then, the distance d between the two projected circles is zero and the projected area $A_{p,b}$ is equal to that of a single sphere πr_s^2 as predicted by Equation (6.8). As bispheres are axisymmetric, the average projected area of a bisphere $\bar{A}_{p,b}$ can be obtained by integrating the expression in Equation (6.8) with respect to ϕ between $-\pi/2$ and $\pi/2$ to yield

$$\bar{A}_{p,b} = \frac{1}{\pi} \int_{-\pi/2}^{\pi/2} A_{p,b}(r, \phi) d\phi \approx 5.35 r_s^2 \quad (6.9)$$

For aggregates with more than two monomers, the average projected area can be calculated numerically by (i) fixing the position of the observer, (ii) rotating the aggregate through numerous orientations around its geometric center, and (iii) computing the different projected area before averaging. The code implementing this procedure was developed and successfully validated with the above expression of $\bar{A}_{p,b}$ for bispheres. For quadspheres and rings of N_s spheres, the average projected area \bar{A}_p was found to be proportional to the square

of the monomer radius r_s such that

$$\bar{A}_p = \alpha(N_s)r_s^2 \quad (6.10)$$

where α is a constant depending on the number of monomers N_s in the aggregate. For quadspheres, $\alpha(4)$ was found to be equal to 9.70 while for a circular ring of N_s monodisperse monomers $\alpha(N_s)$ was such that $\alpha(N_s) = 2.42N_s$ for $N_s \geq 5$. In practice, \bar{A}_p can be measured using image analysis of two-dimensional micrographs of freely suspended microorganisms [194].

6.3.2.2 Radiation characteristics

The absorption $\langle Q_{abs} \rangle$ and scattering $\langle Q_{sca} \rangle$ efficiency factors and the normalized Stokes scattering matrix elements of randomly oriented bispheres, quadspheres, and rings of monodisperse spheres of radius r_s were computed using the superposition T-matrix code described in Ref. [195]. On the other hand, the absorption and scattering efficiency factors and the scattering matrix elements of the different equivalent homogeneous spheres and coated spheres were computed based on Lorenz-Mie theory [78, 166, 196]. The Matlab codes implementing these solutions were obtained from Ref. [196].

The absorption $\langle C_{abs}^a \rangle$ and scattering $\langle C_{sca}^a \rangle$ cross-sections of the randomly oriented aggregates were estimated from the numerically predicted absorption $\langle Q_{abs}^a \rangle$ and scattering $\langle Q_{sca}^a \rangle$ efficiency factors according to

$$\langle C_{abs}^a \rangle = \langle Q_{abs}^a \rangle \pi r_{v,eq}^2 \quad \text{and} \quad \langle C_{sca}^a \rangle = \langle Q_{sca}^a \rangle \pi r_{v,eq}^2 \quad (6.11)$$

where $r_{v,eq}$ is the radius of the volume equivalent sphere given by Equation (6.5) and $\pi r_{v,eq}^2$ represents its projected surface area [195]. Similarly, the cross-sections of the volume equivalent sphere were obtained according to $C_{abs/sca}^s = Q_{abs/sca}^s \pi r_{v,eq}^2$. In the case of the volume and surface area equivalent coated spheres, the cross-sections were estimated based on the outer radius, i.e, $C_{abs/sca,V+S}^{cs} = Q_{abs/sca,V+S}^{cs} \pi r_{s,eq,o}^2$. Finally, the cross-sections of the volume and average projected area equivalent coated sphere were computed based on the average projected area of the aggregates such that $C_{abs/sca,V+\bar{A}_p}^{cs} = Q_{abs/sca,V+\bar{A}_p}^{cs} \bar{A}_p$.

Finally, the relative errors in the absorption and scattering cross-sections and asymmetry factors between the bispheres, quadspheres, and rings of spheres and their equivalent spheres and coated spheres were used to identify the best approximation.

6.4 Results and discussions

6.4.1 Absorption and scattering cross-sections

Figure 6.4 shows the absorption cross-section $\langle C_{abs}^a \rangle$ of randomly oriented (a) bispheres and quadspheres, and (b) circular rings of 10 and 20 spheres as a function of monomer size parameters χ_s ranging from 0.01 to 10. Here, the relative complex index of refraction of the monomers was taken as $m = 1.03 + i0.004$ representative of photosynthetic microorganisms in their growth medium exposed to light in the PAR region [177, 181]. They also plot the absorption cross-section of the corresponding equivalent spheres and coated spheres. Figures 6.4a and 6.4b indicate that the absorption cross-section increased with increasing number of monomers N_s and size parameter χ_s . They also established that $\langle C_{abs}^a \rangle$ was linearly proportional to χ_s^3 . In addition, Figures 6.4c to 6.4f show the relative errors in the absorption cross-section between the aggregates considered and the different equivalent particles as functions of χ_s . As observed in the literature [117, 181, 188, 189], all equivalent spheres and coated spheres featured very similar absorption cross-sections. The relative error in the absorption cross-sections of the bispheres and quadspheres was less than 1.5% for all equivalent particles and size parameter χ_s considered. Similarly, the relative error in the absorption cross-sections of the rings of 10 and 20 spheres and of the equivalent particles was less than 7%. Such good agreement can be attributed to the fact that all equivalent spheres and the shell of the equivalent coated spheres had the same volume as that of the bispheres, quadspheres, and rings of spheres for any given value of χ_s . These observations indicate that self-shading in these aggregates had negligible effect on the absorption cross-sections thanks to the relatively small monomer absorption index $k_s = 0.0053$. Overall, the volume and average projected area equivalent coated spheres provided the best approximation of

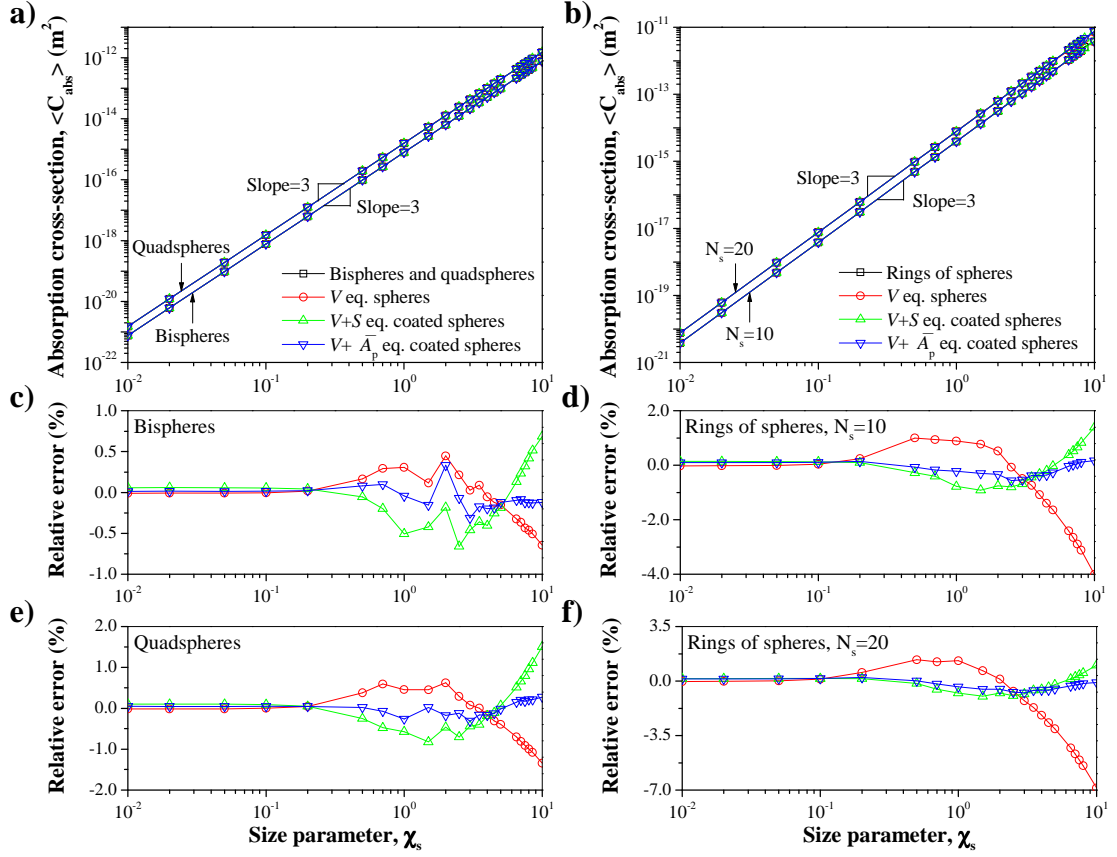


Figure 6.4: Absorption cross-section of randomly oriented (a) bispheres and quadspheres and (b) rings of $N_s = 10$ and 20 spheres and of their corresponding equivalent spheres and coated spheres as a function of monomer size parameter χ_s ranging from 0.01 to 10 for $m = 1.03 + i0.004$. Relative errors in the absorption cross-section between the T-matrix predictions and the equivalent particles for (c) bispheres, (e) quadspheres (d) rings of 10 spheres, and (f) rings of 20 spheres.

the absorption cross-section for all values of χ_s . In fact, the corresponding relative error between the superposition T-matrix prediction and this approximation did not exceed 1% for all aggregates considered.

Figure 6.5 shows the scattering cross-section $\langle C_{sca}^a \rangle$ of randomly oriented (a) bispheres and quadspheres and (b) circular rings of 10 and 20 spheres as a function of χ_s for $m = 1.03 + i0.004$. They also plot the scattering cross-section of the corresponding equivalent

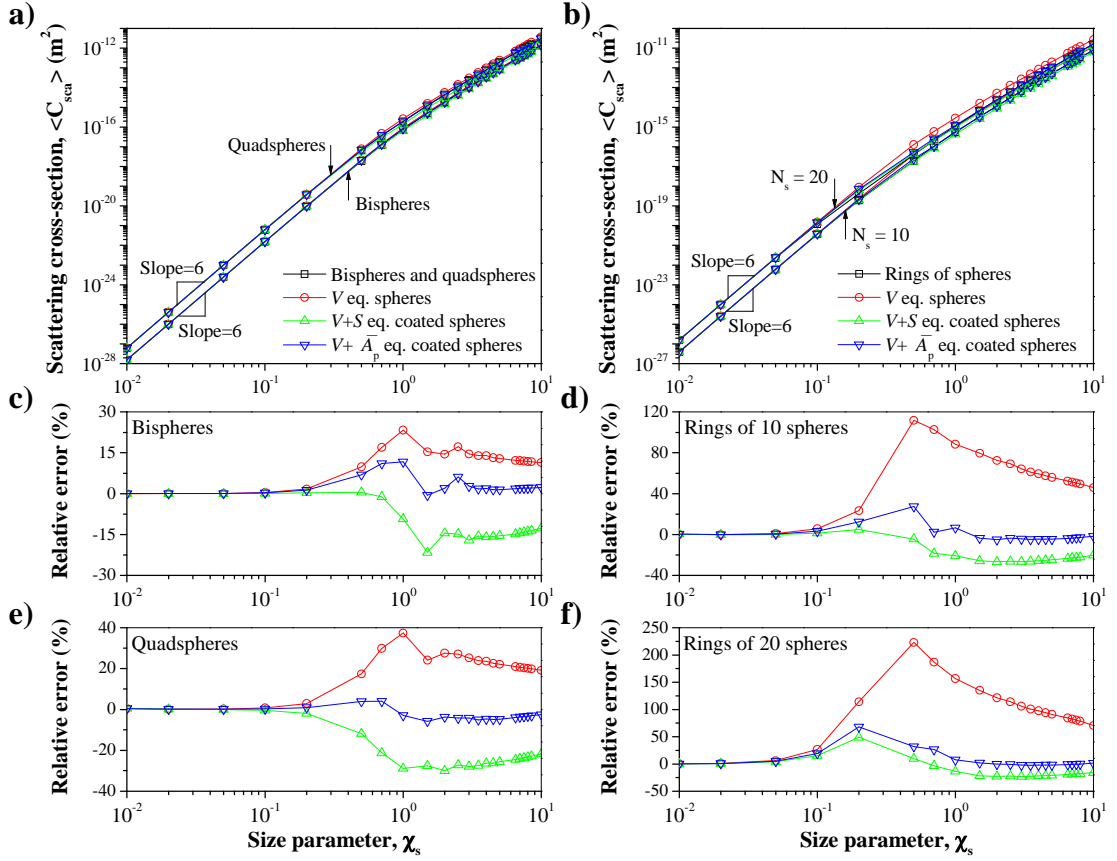


Figure 6.5: Scattering cross-section of randomly oriented (a) bispheres and quadspheres and (b) rings of $N_s = 10$ and 20 spheres and of their corresponding equivalent spheres and coated spheres as a function of monomer size parameter χ_s ranging from 0.01 to 10 for $m = 1.03 + i0.004$. Relative errors in the scattering cross-sections between the T-matrix predictions and the equivalent particles for (c) bispheres, (e) quadspheres, (d) rings of 10 spheres, and (f) rings of 20 spheres.

spheres or coated spheres. Here also, the scattering cross-sections of the aggregates were found to increase with increasing monomer size parameters χ_s and number of monomers N_s . For χ_s less than 0.1, the scattering cross-section was directly proportional to χ_s^6 for all aggregates considered. Figures 6.5c to 6.5f show the relative errors in scattering cross-sections resulting between predictions from the superposition T-matrix and the different equivalent particle approximations. The relative errors in the scattering cross-sections for

all the equivalent particles were found to be less than 5% when χ_s was smaller than 0.1. In this case, the particles were much smaller than the wavelength of the incident EM wave. Each volume element in the aggregate or the equivalent scattering particle scattered light independently of the others [125]. Note that the range of χ_s for which good agreement was observed was smaller for the rings of 10 and 20 spheres because they had larger total volume for the same value of χ_s . As χ_s increased, the size of the aggregate became comparable to the wavelength of the incident EM wave and the relative errors in the scattering cross-sections increased. For χ_s larger than 1, the relative errors in the scattering cross-section between the T-matrix predictions and the volume equivalent spheres and the volume and surface area equivalent coated spheres were excessively large. By contrast, the relative errors corresponding to the volume and average projected area equivalent coated spheres was less than 6%. Thus, both the volume and the average projected area of the aggregate should be preserved by the equivalent particle in order to match the absorption and scattering cross-sections. Again, this cannot be achieved by an equivalent sphere.

Figure 6.6a shows $\langle C_{abs}^a \rangle$ as a function of the product $N_s \chi_s^3$ for bispheres, quadspheres, and rings of 10 and 20 spheres. First, it is interesting to note that the data for $\langle C_{abs}^a \rangle$ for the four types of aggregates collapsed onto a single line. In fact, for all these aggregates, $\langle C_{abs}^a \rangle$ was linearly proportional to $N_s \chi_s^3$ for all monomers size parameters χ_s considered. Similarly, Figure 6.6b shows $\langle C_{sca}^a \rangle$ as a function of the product $N_s^2 \chi_s^6$ for bispheres, quadspheres, and rings of 10 and 20 spheres. It indicates that the data for these different aggregates collapsed also onto a single line and that $\langle C_{sca}^a \rangle$ was proportional to $N_s^2 \chi_s^6$ for $\chi_s \leq 0.1$. These observations are consistent with predictions by the Rayleigh-Debye-Gans approximation valid for fractal aggregates of small and optically soft monomers, i.e., $\chi_s \ll 1$ and $|m - 1| \ll 1$ [197].

Overall, approximating bispheres, quadspheres, and rings of spheres by equivalent coated spheres with identical volume and average projected area provided the best estimates of $\langle C_{abs}^a \rangle$ and $\langle C_{sca}^a \rangle$ for the four types of aggregates of interest for all monomer size parameters χ_s and number of monomers N_s considered. Thus, other equivalent particles will not be considered further.

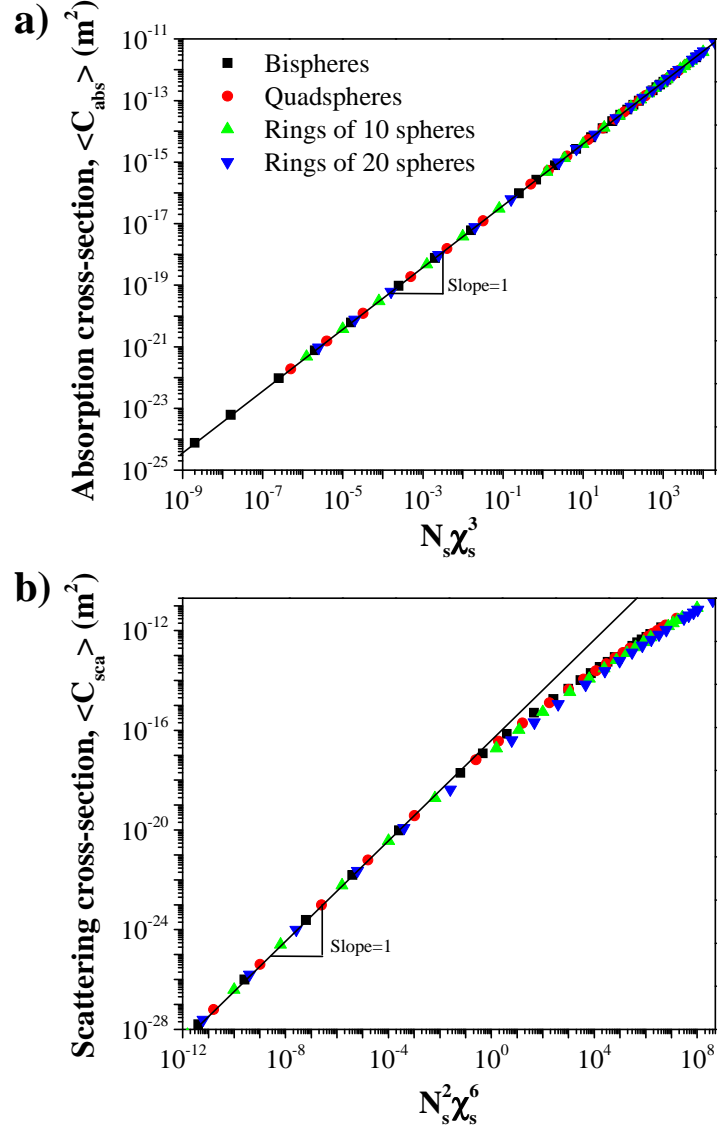


Figure 6.6: (a) Absorption and (b) scattering cross-sections of bispheres, quadspheres, rings of 10 and 20 spheres as functions of $N_s \chi_s^3$ and $N_s^2 \chi_s^6$, respectively.

6.4.2 Scattering phase function and asymmetry factor

Figure 6.7 shows the scattering phase function $F_{11}(\Theta)$ of randomly oriented (a) bispheres, (b) quadspheres, and circular rings of (c) 10 and (d) 20 spheres as functions of the scattering angles Θ for monomer size parameters $\chi_s = 0.01, 0.1, 1$, and 10 and for $m = 1.03 + i0.004$.

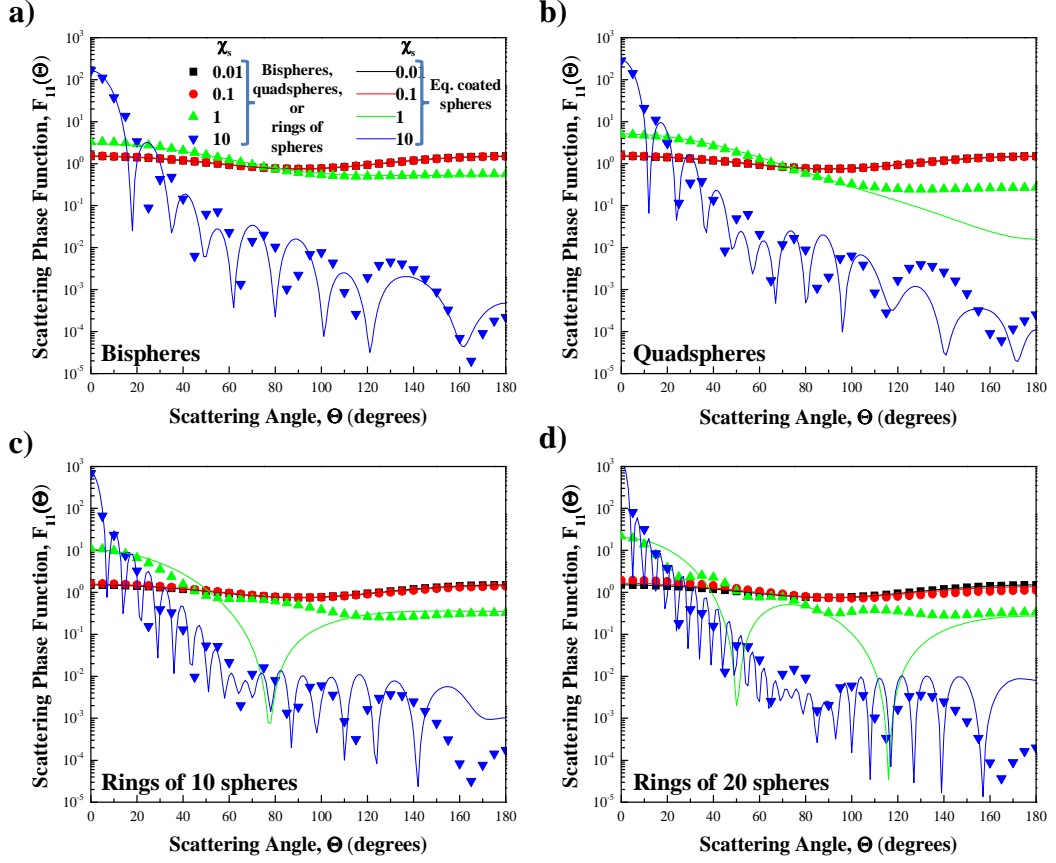


Figure 6.7: Scattering phase function $F_{11}(\Theta)$ as a function of scattering angles Θ for (a) bispheres, (b) quadspheres, and rings of spheres with (c) $N_s = 10$ and (d) $N_s = 20$ monomers with monomer size parameters $\chi_s = 0.01, 0.1, 1$, and 10 and $m = 1.03 + i0.004$ along with those for their corresponding volume and average projected area equivalent coated spheres.

It also plots the phase function of the corresponding volume and average projected area equivalent coated spheres. For any aggregate with monomer size parameter χ_s between 0.01 and 0.1 , the phase function was nearly uniform in all directions, corresponding to quasi-isotropic scattering. For monomer size parameter χ_s equal to 1 and 10 , scattering was mainly and increasingly in the forward direction. In addition, $F_{11}(\Theta)$ oscillated strongly with scattering angle Θ for χ_s equal to 10 . The number of oscillation lobes increased with increasing number of monomers N_s and with size parameter χ_s . The resonance angles and amplitudes of these oscillations were different for bispheres, quadspheres, and rings of

spheres. Note that in practical applications, monomers and aggregates may be polydisperse in terms of size parameter χ_s and monomer number N_s . In this case, we anticipate that the oscillations observed in Figure 6.7 would be “washed” out [172]. Moreover, the phase functions of the volume and average projected area equivalent coated spheres showed similar trends as those of the bispheres, quadspheres, and rings of spheres. Very good agreement was systematically observed for bispheres, quadspheres, and rings of spheres monomer size parameter χ_s less than 0.1. However, for χ_s larger than (i) 10 for bispheres and (ii) 1 for quadspheres and rings of spheres, the scattering phase function $F_{11}(\Theta)$ of the equivalent coated spheres featured more oscillations than that of the corresponding aggregate. This could be explained by the fact that the coating behaves as a waveguide causing radiation entering the coating to circumnavigate the core due to total internal refraction [167]. As this guided radiation escapes the coating, it interferes with the reflected radiation to cause the oscillations observed in the phase function of the equivalent coated sphere [167]. Note however, that for all aggregates and size parameters considered, $F_{11}(0^\circ)$ was predicted within 16%.

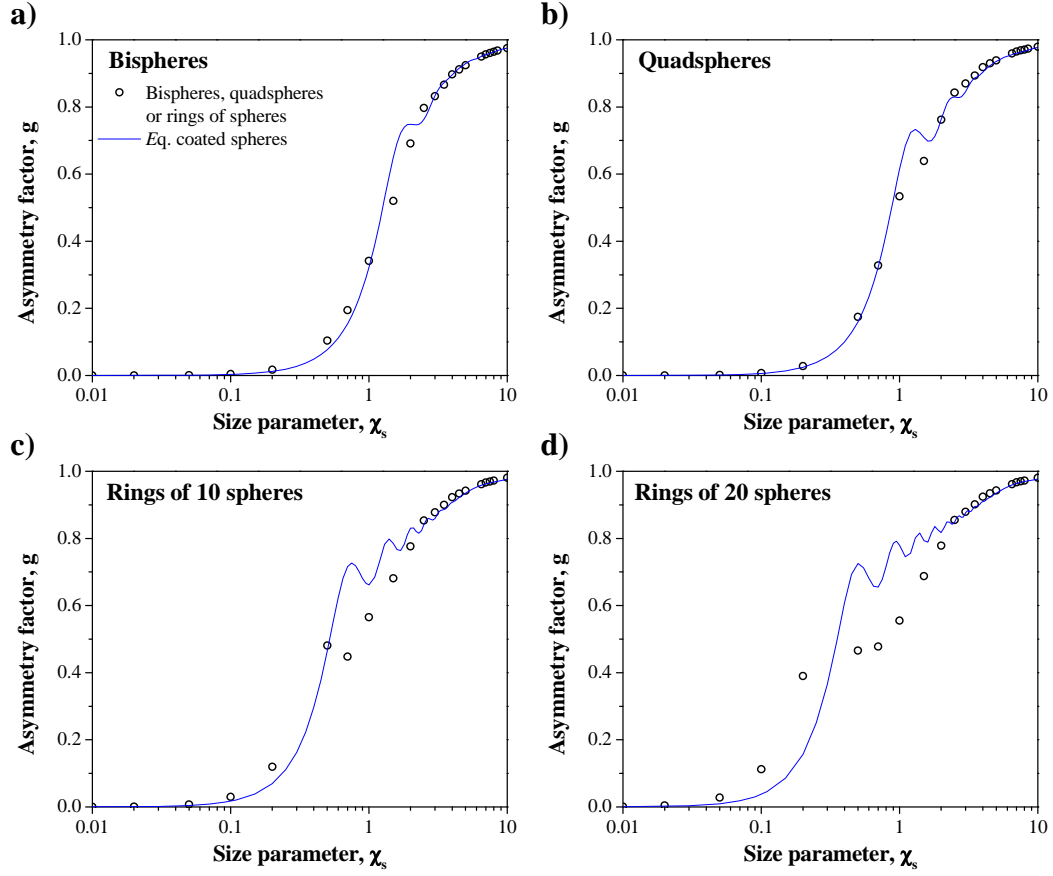


Figure 6.8: Asymmetry factor g as a function of monomer size parameter χ_s ranging from 0.01 to 10 with $m = 1.03 + i0.004$ for (a) bispheres, (b) quadspheres, and rings of spheres with (c) $N_s = 10$ and (d) $N_s = 20$ monomers and for their corresponding equivalent volume and average projected area coated spheres.

Figure 6.8 shows the asymmetry factor g , defined by Equation (6.4), as a function of the monomer size parameter χ_s for (a) bispheres, (b) quadspheres, and circular rings consisting of (c) $N_s = 10$ and (d) 20 spheres, respectively for $m = 1.03 + i0.004$. It also plots the values of g for the corresponding volume and average projected area equivalent coated spheres. The asymmetry factor g was smaller than 0.1 for all aggregates with monomer size parameter χ_s smaller than 0.1. In this regime, the aggregates scattered light quasi-isotropically and feature similar phase functions (Figure 6.7). For size parameter larger than 2, the aggregates were largely forward scattering and g approached unity. The asymmetry factor predicted for the volume and average projected area equivalent coated spheres was in good agreement with predictions by the T-matrix method for bispheres and quadspheres for all values of χ_s considered. Good agreement was also found for rings of spheres with size parameter less than 0.1 or larger than 2. The relative error increased with increasing number of monomers N_s present in the ring.

Overall, the asymmetry factor g of the bispheres, quadspheres, and rings of spheres and that of their corresponding volume and average projected area equivalent coated spheres showed reasonably good agreement. Note that knowing the integral radiation characteristics $\langle C_{abs}^a \rangle$, $\langle C_{sca}^a \rangle$, and g or the backscattering ratio is sufficient to predict light transfer through a microorganism suspension contained in open ponds and flat-plate PBRs [49, 165]. Thus, in the context of photobioreactor design and control, the above results establish that the types of cyanobacteria shown in Figure 7.1 can be approximated as coated spheres with the same volume and projected area and complex indices of refraction of the core and coating equal to those of the medium and cells, respectively.

6.4.3 Scattering matrix elements

The scattering matrix elements can provide useful information in applications considering the polarization of scattered radiation such as remote sensing of phytoplankton suspensions [113]. Figures 6.9(a) to 6.9(f) show the scattering matrix element ratios $-F_{12}(\Theta)/F_{11}(\Theta)$, $F_{33}(\Theta)/F_{11}(\Theta)$, $F_{44}(\Theta)/F_{11}(\Theta)$, and $F_{34}(\Theta)/F_{11}(\Theta)$ for randomly oriented bispheres and

quadspheres as functions of scattering angles Θ for monomer size parameters $\chi_s = 0.01, 0.1, 1$, and 10 with $m = 1.03 + i0.004$. They also show the scattering matrix elements of the corresponding volume and average projected area equivalent coated spheres. Similarly, Figures 6.10(a) to 6.10(f) show the scattering matrix element ratios for randomly oriented rings of 10 and 20 spheres and their corresponding volume and average projected area equivalent coated spheres. First, the scattering matrix ratio $F_{22}(\Theta)/F_{11}(\Theta)$ was found to be nearly 100% for bispheres, quadspheres, and rings of spheres for all scattering angles Θ between 0 and 180° and for all size parameters considered (not shown). In addition, for all aggregates, the degree of linear polarization of the scattered radiation, represented by the ratio $-F_{12}(\Theta)/F_{11}(\Theta)$, was zero in the forward ($\Theta = 0^\circ$) and backward ($\Theta = 180^\circ$) directions and reached a maximum of 100% at $\Theta = 90^\circ$. In addition, the element ratios $F_{33}(\Theta)/F_{11}(\Theta)$ and $F_{44}(\Theta)/F_{11}(\Theta)$ of the different aggregates were identical. These results were analogous to those for a single sphere and can be attributed to the dominant role of single scattering by the monomers [198,199]. Indeed, in the case of a single sphere, $F_{22}(\Theta) = F_{11}(\Theta)$ and $F_{33}(\Theta) = F_{44}(\Theta)$.

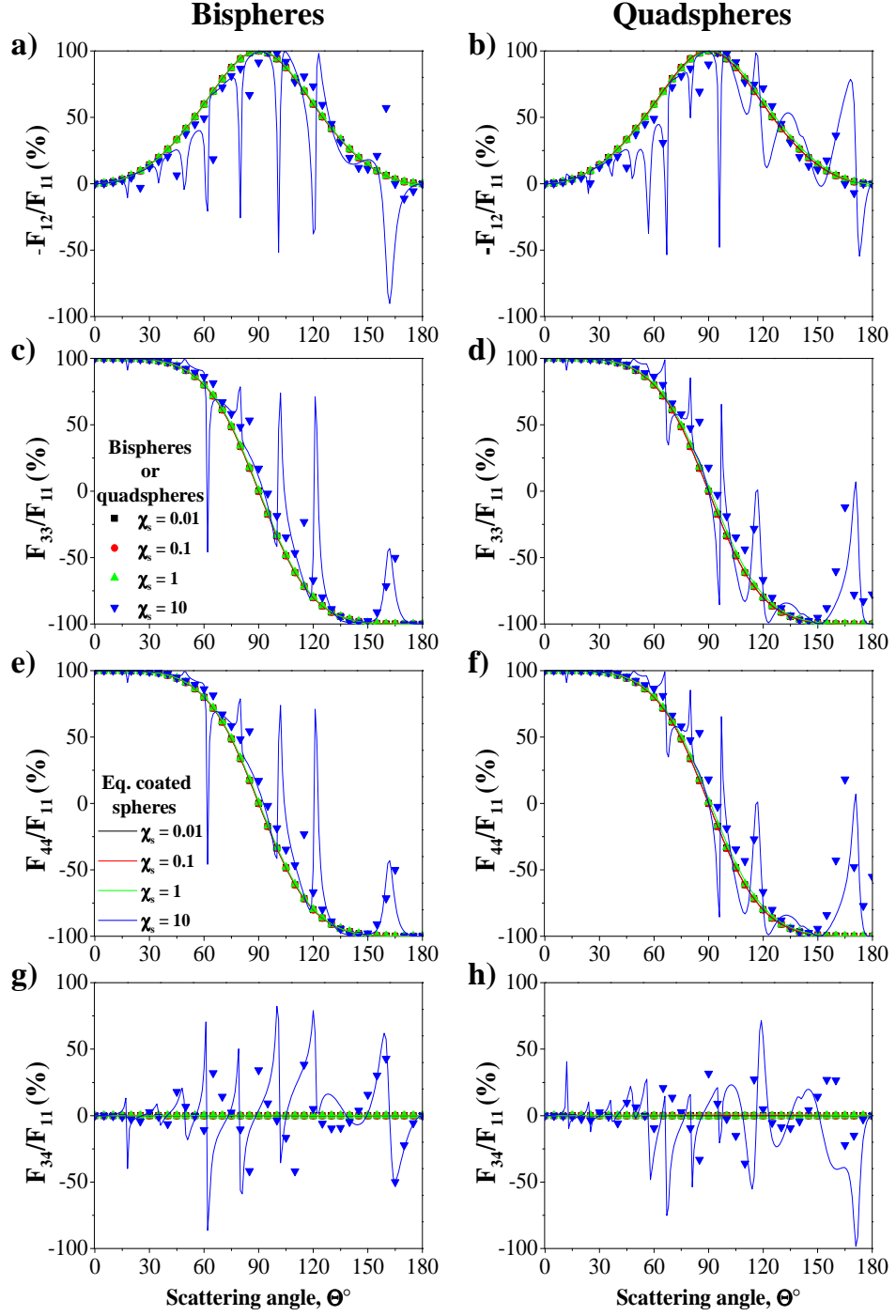


Figure 6.9: Scattering matrix element ratios (a) and (b) $-F_{12}/F_{11}$, (c) and (d) F_{33}/F_{11} , (e) and (f) F_{44}/F_{11} , and (g) and (h) F_{34}/F_{11} as functions of scattering angle Θ obtained with the T-matrix method for bispheres and quadspheres and for the corresponding volume and average projected area equivalent coated spheres for monomer size parameters $\chi_s = 0.01, 0.1, 1$, and 10 .

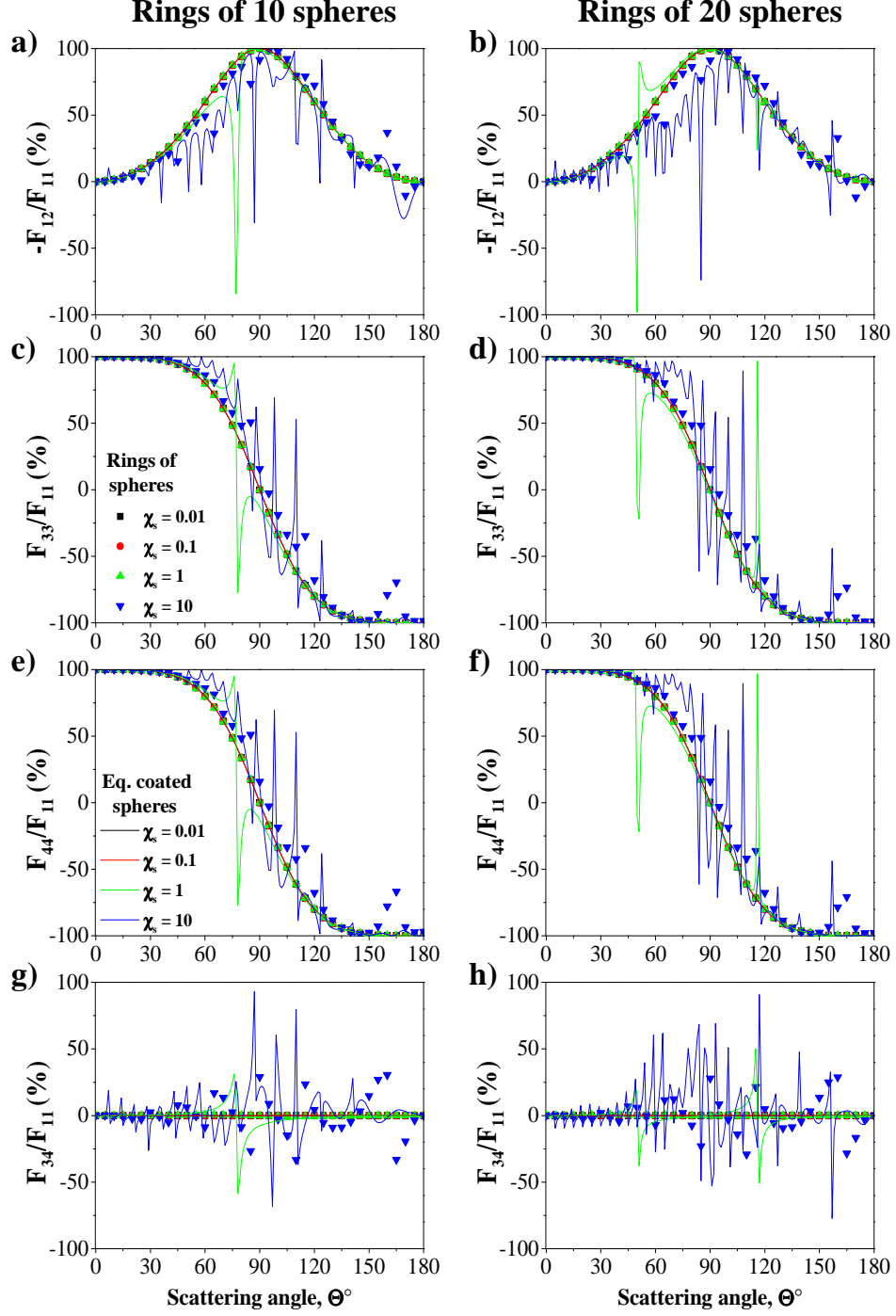


Figure 6.10: Scattering matrix element ratios (a) and (b) $-F_{12}/F_{11}$, (c) and (d) F_{33}/F_{11} , (e) and (f) F_{44}/F_{11} , and (g) and (h) F_{34}/F_{11} as functions of scattering angle Θ obtained with the T-matrix method for rings of 10 spheres and 20 spheres, respectively, and for the corresponding volume and average projected area equivalent coated spheres for monomer size parameters $\chi_s = 0.01, 0.1, 1$, and 10.

Oscillations in the scattering matrix element ratios $F_{33}(\Theta)/F_{11}(\Theta)$ and $F_{44}(\Theta)/F_{11}(\Theta)$ appeared for bispheres, quadspheres with size parameter $\chi_s = 10$ and for the circular rings of 10 and 20 spheres with size parameter $\chi_s = 1$ and 10. These oscillations were observed at the same resonance angles as those of the scattering phase function $F_{11}(\Theta)$ shown in Figure 6.7. Similarly, $F_{34}(\Theta)/F_{11}(\Theta)$ was equal to zero for all scattering angles for all monomer size parameters except for $\chi_s = 10$ for bispheres and quadspheres and $\chi_s = 1$ and 10 for rings of 10 and 20 monomers. Although the general trends of the scattering matrix element ratios for bispheres, quadspheres, and rings of spheres were captured by those of the corresponding volume and average projected area equivalent coated sphere, the latter generally exhibited more oscillations for a given value of χ_s . This can also be attributed to the waveguiding effects of the coating previously discussed.

Overall, the volume and average projected area equivalent coated sphere had scattering matrix elements similar to those of the bispheres, quadspheres, and rings of spheres except when χ_s and/or N_s were large. Then, the approximation could not capture the oscillations peaks in $F_{12}(\Theta)/F_{11}(\Theta)$, $F_{22}(\Theta)/F_{11}(\Theta)$, $F_{33}(\Theta)/F_{11}(\Theta)$, $F_{34}(\Theta)/F_{11}(\Theta)$, and $F_{44}(\Theta)/F_{11}(\Theta)$. Therefore, they should not be used for estimating these scattering matrix element ratios.

6.4.4 Effect of the relative complex index of refraction

The volume and average projected area equivalent coated spheres were shown to accurately approximate the absorption and scattering cross-sections and asymmetry factor of randomly oriented bispheres, quadspheres, and rings of 10 and 20 spheres consisting of optically soft monomers having relative complex index of refraction $m = 1.03 + i0.004$. One may wonder if this approximation is also valid for aggregates with different refractive and absorption indices. To address this question, the relative refractive index n of the monomers was increased from 1.03 to 1.2 and 1.5 while keeping the relative absorption index constant and equal to 0.004. Similarly, the relative absorption index k of the monomers was increased from 0.004 to 0.01 and 0.1 while keeping the relative refractive index constant at $n = 1.03$.

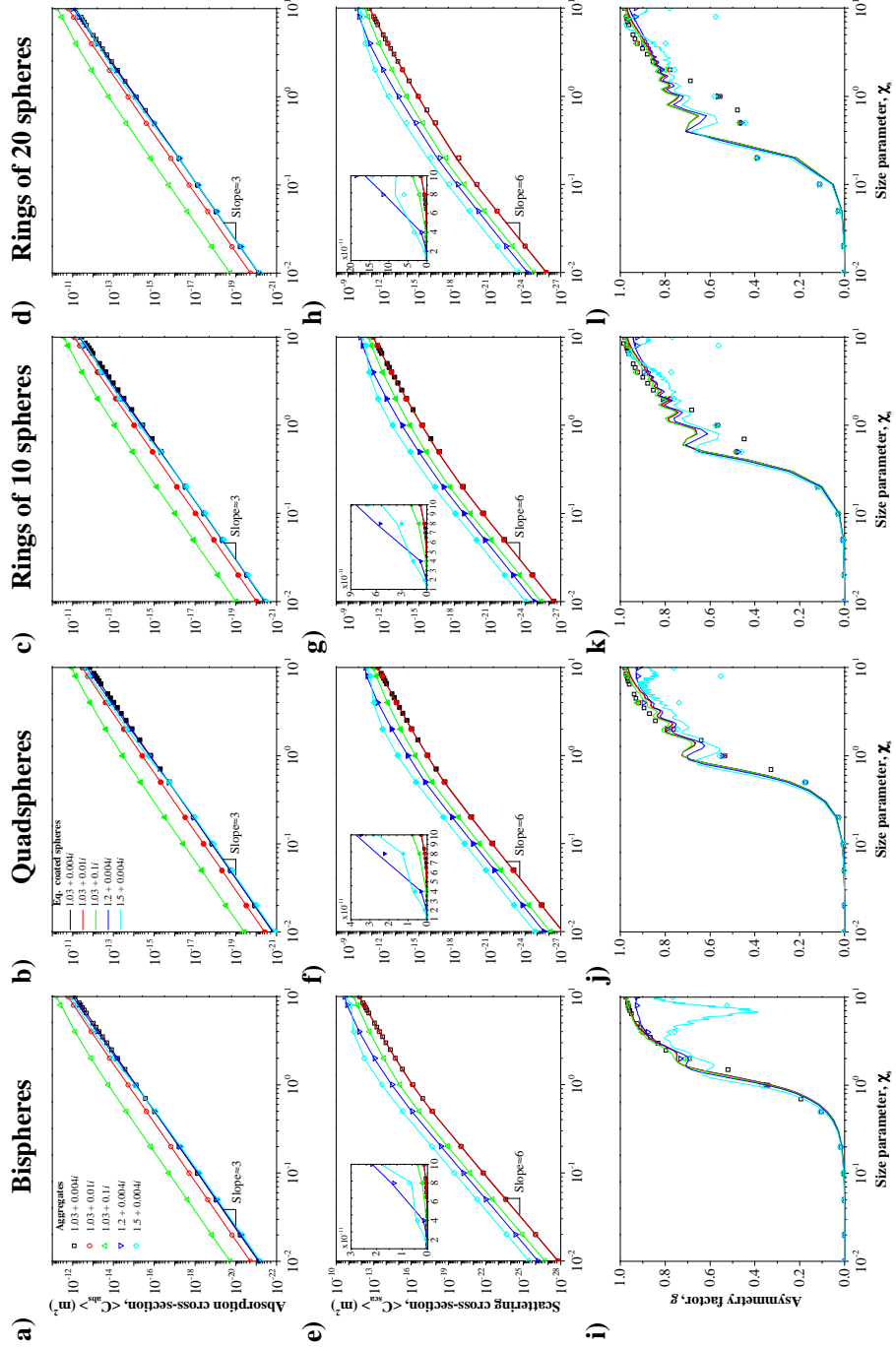


Figure 6.11: (a)-(d) Absorption and (e)-(h) scattering cross-sections and (i)-(l) asymmetry factors of bispheres, quadspheres, and rings of 10 and 20 spheres, respectively, as functions of monomer size parameters χ_s ranging from 0.01 to 10 and their corresponding volume and average projected area equivalent coated spheres with different complex indices of refraction.

Figure 6.11 shows the (a-d) absorption and (e-h) scattering cross-sections and (i-e) asymmetry factor of randomly oriented bispheres, quadrspheres, circular rings of 10 and 20 monomers predicted by the T-matrix method as functions of the monomers' size parameters χ_s ranging from 0.01 to 10 for different values of the complex index of refraction. It also plots predictions for the associated corresponding volume and average projected area equivalent coated spheres. It is evident that increasing the relative refractive index n resulted in increasing scattering cross-section of bispheres, quadrspheres, and rings of spheres due to the larger index mismatch at the interface between the monomers and the surrounding medium. Similarly, increasing the relative absorption index k of the monomers resulted in increasing absorption cross-section of all the aggregates considered. For all values of n and k considered, $\langle C_{abs}^a \rangle$ was proportional to $N_s \chi_s^3$ and $\langle C_{sca}^a \rangle$ was proportional to $N_s \chi_s^6$, for χ_s less than 1.0.

The relative error between the absorption cross-sections of the aggregates and that of the corresponding volume and average projected area equivalent coated spheres with relative refractive index n equal to 1.2 was less than 8% for all values of χ_s considered. However, it was significantly larger for $n = 1.5$, particularly for the rings of spheres with increasing size parameter χ_s and number of monomers N_s . On the other hand, increasing the relative absorption index k from 0.004 to 0.1 while n was kept constant at $n = 1.03$ did not affect the performance of the volume and average projected area equivalent coated sphere approximation. Then, the relative errors in the absorption cross-section was less than 6% for all values of k and χ_s considered. This indicates that potential shading among monomers was captured by the equivalent coated sphere approximation. These observations are consistent with the literature [117, 181, 188, 189, 192]. However, they are valid for optically soft scattering particles such that the penetration depth of the incident EM wave is larger than the particle size. In cases when the size of the scattering particle is larger than the penetration depth, absorption becomes a surface phenomenon and the proposed equivalent coated sphere approximation may not be valid.

Moreover, the relative error in the scattering cross-section between the aggregates and their volume and average projected area equivalent coated spheres increased with increasing

relative refractive index n and number of monomers N_s in the aggregates. Indeed, scattering is sensitive to particle shape and size and to the mismatch in refractive index between the particle and its surroundings. By contrast, the relative absorption index k did not affect the predictions of $\langle C_{sca}^a \rangle$ significantly. Here, the same trends in $\langle C_{sca}^a \rangle$ as those observed in Figure 6.5 were obtained for $k = 0.004$ while n increased from 1.03 to 1.2 and 1.5. For χ_s smaller than 0.1 and larger than 1, the relative error for any aggregate considered was less than 5% and 17% for n equal to 1.03 and 1.2, respectively. In the same χ_s range, the relative error for the bispheres, quadspheres, and rings of 10 and 20 spheres with $n = 1.5$ increased and reached up to 12%, 22%, 22%, and 44%, respectively.

Finally, the asymmetry factor did not change significantly when the monomers' relative refractive index n increased from 1.03 to 1.2 and their relative absorption index k varied from 0.004 to 0.1. However, for $n = 1.5$, the aggregates had smaller asymmetry factor than the volume and average projected area equivalent coated spheres for χ_s larger than 1.0.

Overall, approximating the integral radiation characteristics of bispheres by those of the volume and average projected area equivalent coated spheres was valid for all values of n , k , and χ_s considered. This approximation was also appropriate for quadspheres and rings of 10 and 20 spheres with relative refractive index n up to 1.2 and relative absorption index k up to 0.1 for monomer size χ_s between 0.01 and 10. This approximation became less accurate as the monomers' relative refractive index n and number N_s in the aggregates increased.

6.4.5 Aggregates of polydisperse monomers

The bispheres, quadspheres, and rings of 10 and 20 spheres considered so far consisted of monodisperse spherical monomers. However, the cells of cyanobacteria such as *A. elenkinii* and *A. circularis* are typically polydisperse, as illustrated in Figure 7.1. Furthermore, the heterocyst present in some cyanobacteria are usually larger than the vegetative cells. This section assesses whether the volume and average projected area equivalent coated sphere approximation was also valid for rings of spheres consisting of polydisperse monomers.

Table 6.1: Comparison between absorption and scattering cross-sections and asymmetry factor of randomly oriented rings of polydisperse spherical monomers and their volume and average projected area equivalent coated spheres. Here also, $m = 1.03 + i0.004$

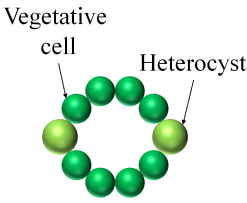
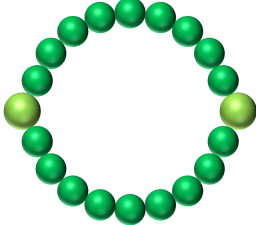
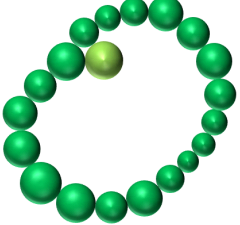
	Aggregate 1	Aggregate 2	Aggregate 3
Schematic			
χ_v/χ_h	8 / 9.6	8 / 9.6	5.3-10.6 / 9.4
N_v/N_h	8 / 2	18 / 2	19 / 1
V (μm^3)	30.6	57.3	57.1
\bar{A}_p (μm^2)	18.3	37.7	35.2
$\langle C_{abs}^a \rangle$ (μm^2)	2.24	4.19	4.16
$\langle C_{sca}^a \rangle$ (μm^2)	4.07	7.43	7.76
g	0.974	0.973	0.976
Volume and average projected area equivalent coated spheres			
$r_{\bar{A}_p,eq,i}$ (μm)	1.90	3.03	2.88
$r_{\bar{A}_p,eq,o}$ (μm)	2.42	3.46	3.35
$C_{abs/sca,V+\bar{A}_p}^{cs}$ (μm^2)	2.24	4.19	4.16
$C_{abs/sca,V+\bar{A}_p}^{cs}$ (μm^2)	4.11	7.38	7.72
g	0.971	0.971	0.972

Table 6.1 shows the schematics of the three different rings of spheres considered and their morphological features. The number of vegetative cells and heterocysts were respectively denoted by N_v and N_h such that $N_s = N_v + N_h$ while each cell type was monodisperse with size parameters χ_v and χ_h , respectively. Aggregate 1 consisted of 10 monomers including 2 heterocyst while Aggregates 2 and 3 had $N_s = 20$ monomers with 2 and 1 heterocysts,

respectively. The radius of the heterocysts in Aggregates 1 and 2 was taken to be 20% larger than that of the vegetative cells. The sizes and positions of the monomers in Aggregate 3 were derived using the micrograph reproduced in Figure 7.1d. In all cases, the size parameters χ_v and χ_h were larger than 5.0. The relative complex index of refraction was assumed to be $m = 1.03 + i0.004$ and identical for both vegetative cells and heterocysts. The average projected area of each of these aggregates was computed numerically to obtain the inner $r_{\bar{A}_p,eq,i}$ and outer $r_{\bar{A}_p,eq,o}$ radii of the corresponding volume V and average projected area \bar{A}_p of the equivalent coated sphere. Table 6.1 reports the absorption $\langle C_{abs}^a \rangle$ and scattering $\langle C_{sca}^a \rangle$ cross-sections and the asymmetry factor g of the three randomly oriented aggregates predicted by the superposition T-matrix method as well as those of the corresponding volume and average projected area equivalent coated spheres. They fell within 1% of each other for the three aggregates considered. In other words, the equivalent coated sphere approximation provided good estimates of $\langle C_{abs}^a \rangle$, $\langle C_{sca}^a \rangle$, and g for rings of polydisperse and optically soft spheres representative of multicellular cyanobacteria.

6.4.6 Computational time

Computing the radiation characteristics of a bisphere, quadisphere, and rings of $N_s = 10$ and 20 monodisperse spheres with $\chi_s = 10$ and $m = 1.03 + i0.004$ using the superposition T-matrix method required 9, 24, 227, and 2063 seconds, respectively, on a parallel computing cluster with 50 CPUs. By contrast, computing the radiation characteristics of the corresponding volume and average projected area equivalent coated spheres on a single dual core 2.53 GHz CPU required 1.3, 1.6, 2.9, and 3.3 microseconds, respectively. Note also that savings in computational time was found to increase as the size parameter χ_s and/or the number of monomers N_s increased. Thus, the proposed volume and average projected area equivalent coated spheres offers a way to estimate their absorption and scattering cross-sections and their asymmetry factor rapidly and relatively accurately.

6.5 Chapter summary

This chapter established that randomly oriented bispheres, quadspheres, and circular rings of spheres can be approximated as equivalent coated spheres with identical volume and average projected area for predicting the absorption and scattering cross-sections and their asymmetry factor. This approximation was valid for monomer size parameter between 0.01 and 10 and for relative refractive index up to 1.2 and absorption index up to 0.1. The general trends in the scattering matrix element ratios of bispheres, quadspheres, and rings of spheres were similar to those of their volume and average projected area equivalent coated spheres except for oscillations observed for monomer size parameters larger than 1.0. This was attributed to internal reflection in the coating and its waveguiding effect. Overall, the equivalent coated sphere approximation offer a simpler, rapid, and relatively accurate way of predicting the radiation characteristics of randomly oriented bispheres, quadspheres, and rings of spheres for a wide range of monomer number, size parameter, and relative complex index of refraction. It can be used for predicting the integral radiation characteristics of photosynthetic microorganisms as well as for retrieving their optical properties and/or their average volume and projected area from radiation characteristic measurements.

CHAPTER 7

Rapid and Accurate Retrieval of The Complex Index of Refraction of Aggregates and *Synechocystis sp.*

This chapter presents an inverse method for retrieving the spectral optical properties of photosynthetic microorganisms resembling bispheres, quadspheres, and fractal aggregates. The method was based on the average projected area and volume equivalent coated sphere approximation developed in Chapter 6. The method was validated for a range of refraction and absorption indices using average absorption and scattering cross-sections computed numerically for different suspensions consisting of bispheres, quadspheres, and fractal aggregates. In addition, the experimentally measured average absorption and scattering cross-sections, size distribution, and scattering phase function of cyanobacterium *Synechocystis sp.* were presented and its spectral complex index of refraction was retrieved.

7.1 Introduction

Measuring the spectral radiation characteristics experimentally requires specialized equipment and can be time consuming [5, 115, 121, 200]. Hence, it is advantageous to directly predict the radiation characteristics using the microorganisms' size distribution and complex index of refraction. Recently, we demonstrated that the integral radiation characteristics of bispheres, quadspheres, rings of spheres, and fractal aggregates could be approximated by those of coated spheres with identical volume and average projected area [201, 202]. This approximation led to significant savings in computational time and resources compared with predictions by the T-matrix method. The goal of the present study is to develop an inverse

method that can retrieve the spectral complex index of refraction of photosynthetic microorganisms with complex morphologies such as bispheres, quadspheres, and fractal aggregates from their radiation characteristics by treating them as volume and average projected area equivalent coated spheres. First, the feasibility of the inverse method was demonstrated using numerically predicted absorption and scattering cross-sections of polydisperse bispheres, quadspheres, and fractal aggregates. Second, the unicellular freshwater cyanobacterium *Synechocystis sp.*, featuring a dumbbell shape, was selected as a model organism to illustrate the method using experimental measurements.

7.1.1 *Synechocystis sp.*

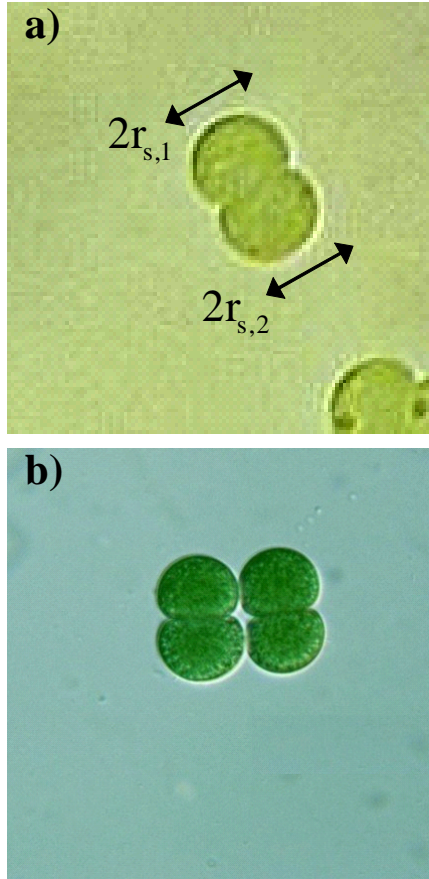


Figure 7.1: Micrographs of (a) free floating dumbbell-shaped *Synechocystis sp.* cell with lengths $r_{s,1}$ and $r_{s,2}$ about $1 \mu m$ long and (b) *Synechocystis sp.* immediately after cell division. Reproduced with permission from Prof. Yuuji Tsukii (Hosei University, <http://protist.i.hosei.ac.jp/>).

The unicellular freshwater cyanobacterium *Synechocystis sp.* PCC 6803 was the first photosynthetic organism whose entire genome was sequenced due to the similarities between its photosynthetic apparatus and that of higher plants [156]. It is widely used as a standard in studies involving photosynthesis, environmental stress response, pigment synthesis, lipid production, and other metabolic processes [156–159]. *Synechocystis sp.* contain different photosynthetic pigments including Chlorophyll *a* (Chl *a*), phycocyanin (PCCN), as well as photosynthetic (PSC) and photoprotective (PPC) carotenoids [203]. Each type of pigment

possess different spectral absorption bands enabling the microorganism to absorb photons in the photosynthetically active radiation (PAR) region ranging from 400 to 700 nm [4]. Figure 7.1a shows a micrograph of dumbbell-shaped *Synechocystis sp.* cells approximately 2 μm in length. Figure 7.1b shows a micrograph of *Synechocystis sp.* immediately after fission where the cell divides into two identical daughter cells [160].

7.1.2 Radiation characteristics of photosynthetic microorganisms

The absorption and scattering cross-sections and the scattering phase function of microorganism in the PAR region depend on wavelength as well as on their morphologies and composition. They can be determined either experimentally or numerically. Previous experimental studies have focused on quasi-spherical microalgae [5, 115] and filamentous cyanobacteria [114, 178]. Numerical studies have typically treated unicellular microorganisms as spheres [99, 177, 204] or coated spheres [201] and predicted their radiation characteristics using their complex index of refraction. Numerical methods, such as the T-matrix method [195], can compute the radiation characteristics of photosynthetic microorganisms with non-spherical shape or complex morphologies. However, these methods can be time-consuming and computationally intensive [201]. Alternatively, photosynthetic microorganisms of complex morphology such as filamentous or dumbbell-shape cyanobacteria could be treated as equivalent scattering particles with simpler shape [56, 99, 177, 201, 204]. Then, their radiation characteristics can be calculated using fast analytical solutions such as the Lorenz-Mie theory [78], the Aden-Kerker theory [166], or the anomalous diffraction approximation [125]. For example, Lee and Pilon [117] reported that randomly oriented filamentous cyanobacteria consisting of linear chains of optically soft spheres could be modeled as randomly oriented volume equivalent infinitely long cylinders for the purpose of predicting their integral radiation characteristics κ_λ , $\sigma_{s,\lambda}$, and g_λ . Similarly, our previous study [201] demonstrated that multicellular cyanobacteria with morphologies of bispheres, quadspheres, and rings of spheres could be approximated as coated spheres with identical average projected area and volume. Kandilian *et al.* [202] also demonstrated that this approximation was valid

for randomly oriented colonies of spherical unicellular microalgae.

The complex index of refraction of microorganisms is essential to compute the radiation characteristics. Aas [131] estimated the refractive index (real part) of phytoplankton cells from their metabolite composition by using a volume-weighted average of the refractive indices of the various constituents including protein, carbohydrate, water, and lipid. Pottier *et al.* [49] predicted the spectral absorption coefficient of *C. reinhardtii* from Lorenz-Mie theory by considering the absorption index as a weighted sum of the absorption indices of the major algal pigments and by taking their refractive index as constant and equal to 1.527. More recently, Dauchet [116] used the same method as Pottier *et al.* [49] to retrieve k_λ and estimated n_λ , on a spectral basis, using Kramer-Kronig relationship relating n_λ to k_λ . In these studies, the microorganism cells were treated as homogeneous spheres with some effective optical properties. Alternatively, the complex index of refraction of microorganisms has been retrieved from experimental measurements of their absorption and scattering cross-sections using inverse methods [175–178]. Here, treating the microorganism cells as simple equivalent scattering particles to compute the radiation characteristics is essential since the forward problem has to be solved numerous times. For example, Bricaud and Morel [175] predicted the complex index of refraction of phytoplanktonic cells by treating them as homogeneous spheres. Based on the anomalous diffraction approximation, the absorption coefficient was described as a continuous and monotonic function of the effective absorption index for a given wavelength and particle size distribution. Then, the spectral absorption index of the cells was determined by iteration until the computed spectral absorption coefficient agreed with the experimentally measured value. The retrieved absorption indices were used as input parameters into the Lorentz-Mie theory. The spectral refractive index of the cells were obtained by iteration until the computed spectral extinction coefficient matched the experimentally measured value. On the other hand, Lee *et al.* [177] developed an inverse method combining genetic algorithm (GA) [96] and the Lorenz-Mie theory [78] to retrieve both the absorption and refractive indices of various quasi-spherical microalgae. Similarly, Heng *et al.* [178] combined GA with electromagnetic wave theory for randomly oriented infinitely

long cylinders [60, 147] to retrieve the effective complex index of refraction of filamentous cyanobacteria *Anaebena cylindrica* from their experimentally measured absorption and scattering cross-sections.

The objective of the present study is to develop and validate an inverse method able to accurately retrieve the spectral complex index of refraction of photosynthetic microorganisms whose morphologies resemble bispheres, quadspheres, or fractal aggregates (colonies) of spherical monomers. First, the method was demonstrated using numerically predicted absorption and scattering cross-sections, based on the T-matrix method, for various cell size distributions and complex indices of refraction. Then, the method was illustrated with experimentally measured absorption and scattering cross-sections and size distribution of *Synechocystis sp.*.

7.2 Analysis

7.2.1 Assumptions

The photosynthetic microorganism cells were treated as homogeneous with some effective complex index of refraction. Although the cells were actually heterogeneous in nature, this assumption is reasonably accurate and has been widely used in the literature [49, 56, 99, 113, 117, 131, 175, 177, 181, 201, 202, 204, 205]. The cells in the culture were assumed to be randomly oriented. Indeed, PBRs are usually agitated by bubble sparging or stirring so as to distribute nutrients and light [37].

7.2.2 Aggregates and their equivalent coated spheres

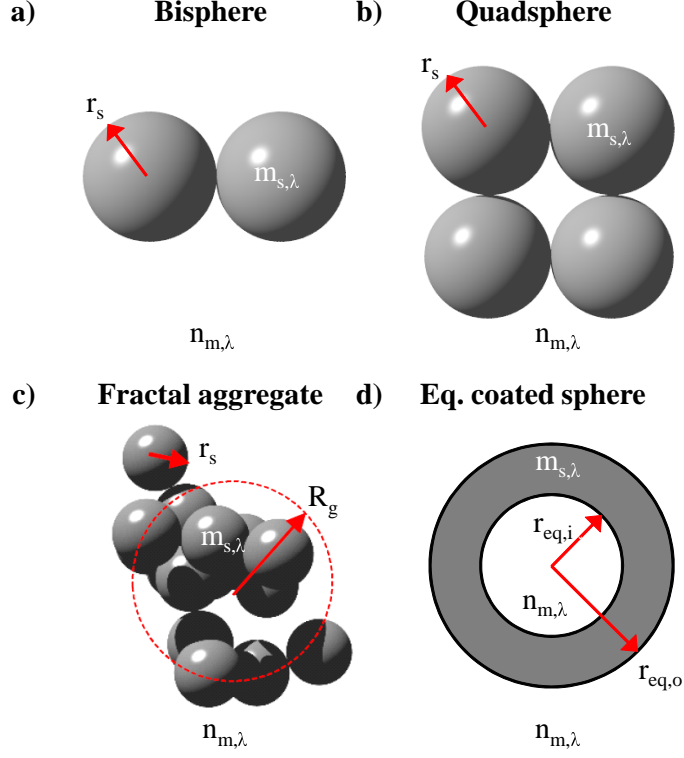


Figure 7.2: Schematics of (a) a bisphere, (b) a quadsphere, (c) a fractal aggregate of spherical monomer of radius r_s , and (d) an average projected area and volume equivalent coated sphere with inner radius $r_{eq,i}$ and outer radius $r_{eq,o}$. The monomers and the coating of the coated sphere had the same complex index of refraction $m_{s,\lambda}$. The surrounding medium and the core of the coated sphere were non-absorbing with refraction index $n_{m,\lambda}$.

Figures 7.2a to 7.2c show schematics of a bisphere, a quadsphere, and a fractal aggregate of spherical monomers, respectively. The number of monomers in each aggregate was denoted by N_s , e.g., $N_s = 2$ for bispheres and $N_s = 4$ for quadspheres. In addition, the radius of the monomers was denoted by r_s and the monomer size parameter was defined as $\chi_s = 2\pi r_s/\lambda$. The structure of fractal aggregates of N_s spherical monomers of radius r_s is characterized by its radius of gyration R_g , fractal dimension D_f , and fractal prefactor k_f [206]. The statistical

rule relating these parameters is given by [206]

$$N_s = k_f \left(\frac{R_g}{r_s} \right)^{D_f} \quad (7.1)$$

The monomers had spectral complex index of refraction $m_{s,\lambda} = n_{s,\lambda} + ik_{s,\lambda}$ where $n_{s,\lambda}$ denotes the spectral refraction index and $k_{s,\lambda}$ denotes the spectral absorption index. The surrounding medium was non-absorbing and had spectral refraction index $n_{m,\lambda}$. Then, the relative refraction n_λ and absorption k_λ indices of the monomers are defined as [92]

$$n_\lambda = \frac{n_{s,\lambda}}{n_{m,\lambda}} \quad \text{and} \quad k_\lambda = \frac{k_{s,\lambda}}{n_{m,\lambda}} \quad (7.2)$$

Figure 7.2d shows a schematic of the average projected area and volume equivalent coated sphere whose coating had the same complex index of refraction $m_{s,\lambda}$ as the monomers while its core consisted of the surrounding medium of refraction index $n_{m,\lambda}$. Its equivalent inner $r_{eq,i}$ and outer $r_{eq,o}$ radii can be expressed as [201]

$$r_{eq,i} = \sqrt[3]{\left(\frac{\bar{A}_p}{\pi} \right)^{3/2} - N_s r_s^3} \quad \text{and} \quad r_{eq,o} = \sqrt{\frac{\bar{A}_p}{\pi}} \quad (7.3)$$

where \bar{A}_p is the average projected area of the aggregate and can be computed numerically [201]. In practice, the average projected area of bispheres $\bar{A}_{p,b}$ and quadspheres $\bar{A}_{p,q}$ can be related to the radius r_s of the monomers according to [201]

$$\bar{A}_{p,b} = 5.35 r_s^2 \quad \text{and} \quad \bar{A}_{p,q} = 9.70 r_s^2 \quad (7.4)$$

In addition, the average projected area of fractal aggregates $\bar{A}_{p,agg}$ can be expressed as [202]

$$\bar{A}_{p,agg} = \pi r_s^2 N_s^\alpha \quad (7.5)$$

where the exponent α is a function of D_f and was shown to have a maximum value of $\alpha_{max} = 0.92$ when $D_f = 1.0$ and a minimum value of $\alpha_{min} = 0.73$ when $D_f = 3.0$ [202]. Then, the reduced variables $\alpha^* = (\alpha - \alpha_{min})/(\alpha_{max} - \alpha_{min})$ and $D_f^* = (D_f - 1)/2$ were found to be related by [202]

$$\alpha^* = (1 + D_f^{*1.8})^{1/1.8} \quad (7.6)$$

7.2.3 Inverse method algorithm

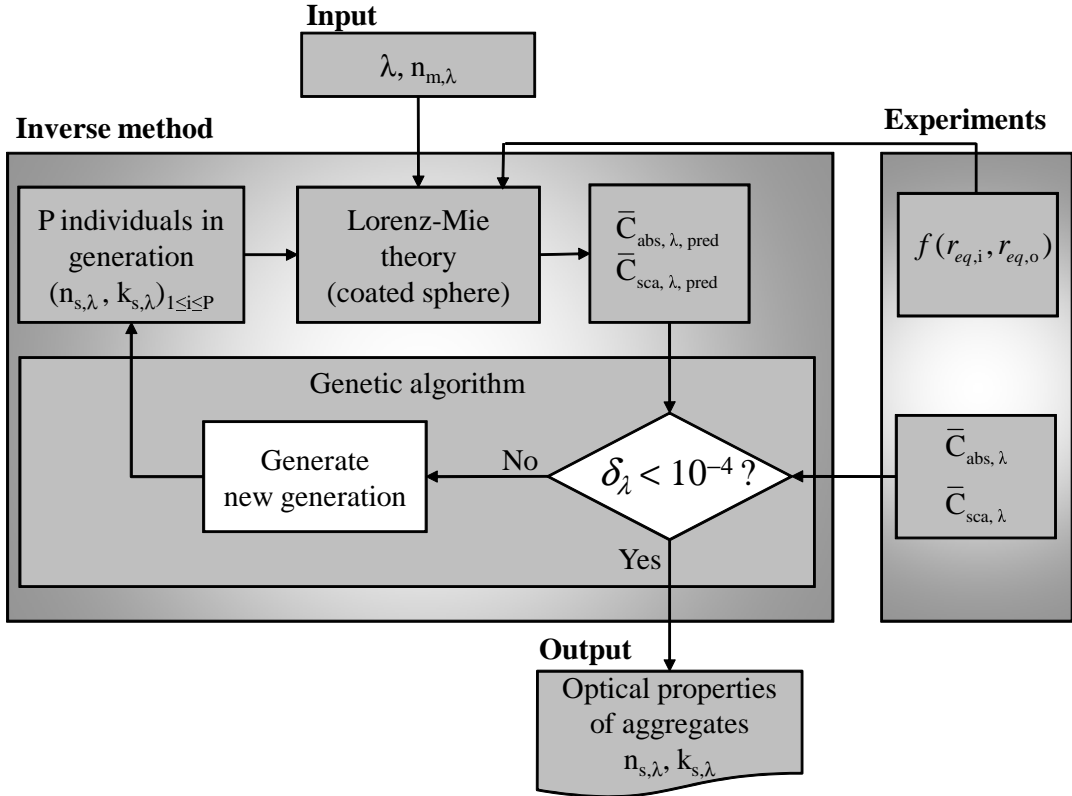


Figure 7.3: Block diagram of the procedure used to retrieve the refractive index $n_{s,\lambda}$ and absorption index $k_{s,\lambda}$ from the measured average spectral absorption and scattering cross-sections $\bar{C}_{abs,\lambda}$ and $\bar{C}_{sca,\lambda}$ and the volume and average projected area equivalent coated sphere radii distribution $f(r_{eq,i}, r_{eq,o})$. Here, $P=100$ individuals per generation for a maximum of 500 generations. The objective function δ_λ to be minimized is defined in Equation (7.7).

Figure 7.3 shows the block diagram of the inverse method used to retrieve the refractive $n_{s,\lambda}$ and absorption $k_{s,\lambda}$ indices of the monomers of polydisperse bisphere, quadisphere, and fractal aggregates of spherical monomers at each wavelength λ from (i) the spectral refractive index $n_{m,\lambda}$ of the medium, (ii) the equivalent coated sphere radii distribution $f(r_{eq,i}, r_{eq,o})$, and (iii) the measured average spectral absorption $\bar{C}_{abs,\lambda}$ and (iv) scattering $\bar{C}_{sca,\lambda}$ cross-sections. The Lorenz-Mie theory for coated spheres [60, 166] was used in the forward model to calculate

the predicted average absorption $\bar{C}_{abs,\lambda,pred}$ and scattering $\bar{C}_{sca,\lambda,pred}$ cross-sections. Then, the general purpose genetic algorithm PIKAIA [96] was used to simultaneously retrieve the values of $n_{s,\lambda}$ and $k_{s,\lambda}$ that minimized the difference between the measured average absorption $\bar{C}_{abs,\lambda}$ and scattering $\bar{C}_{sca,\lambda}$ cross-sections of the aggregates and the ones predicted using the equivalent coated sphere approximation. The use of a genetic algorithm such as PIKAIA provides a reliable method in the search for the global minimum of an objective function [96]. Here, the objective function δ_λ at wavelength λ to be minimized was defined as

$$\delta_\lambda = \left(\frac{\bar{C}_{abs,\lambda,pred} - \bar{C}_{abs,\lambda}}{\bar{C}_{abs,\lambda}} \right)^2 + \left(\frac{\bar{C}_{sca,\lambda,pred} - \bar{C}_{sca,\lambda}}{\bar{C}_{sca,\lambda}} \right)^2 \quad (7.7)$$

The genetic algorithm used a maximum of 500 generations and a population of 100 individuals per generation. Each individual consist of a pair $(n_{s,\lambda}, k_{s,\lambda})$. In the case when a generation featured an individual producing a value of δ_λ smaller than 10^{-4} , the corresponding values of $n_{s,\lambda}$ and $k_{s,\lambda}$ were reported as the retrieved refraction and absorption indices of the monomer at wavelength λ . Then, this procedure was repeated for another wavelength. It was performed on a single dual core 2.53 GHz CPU with 4.00 GB RAM.

7.2.4 Validation of the inverse method

In order to assess the validity of the inverse method for a broad range of suspensions and monomer relative complex index of refraction $m_\lambda = n_\lambda + ik_\lambda$, we considered four different suspensions of aggregates with various size distributions. The average absorption $\bar{C}_{abs,\lambda}$ and scattering $\bar{C}_{sca,\lambda}$ cross-sections of these suspensions were computed using the T-matrix method [195]. These results were then used in the inverse method to retrieve the relative refractive and absorption indices denoted by $n_{\lambda,pred}$ and $k_{\lambda,pred}$, respectively.

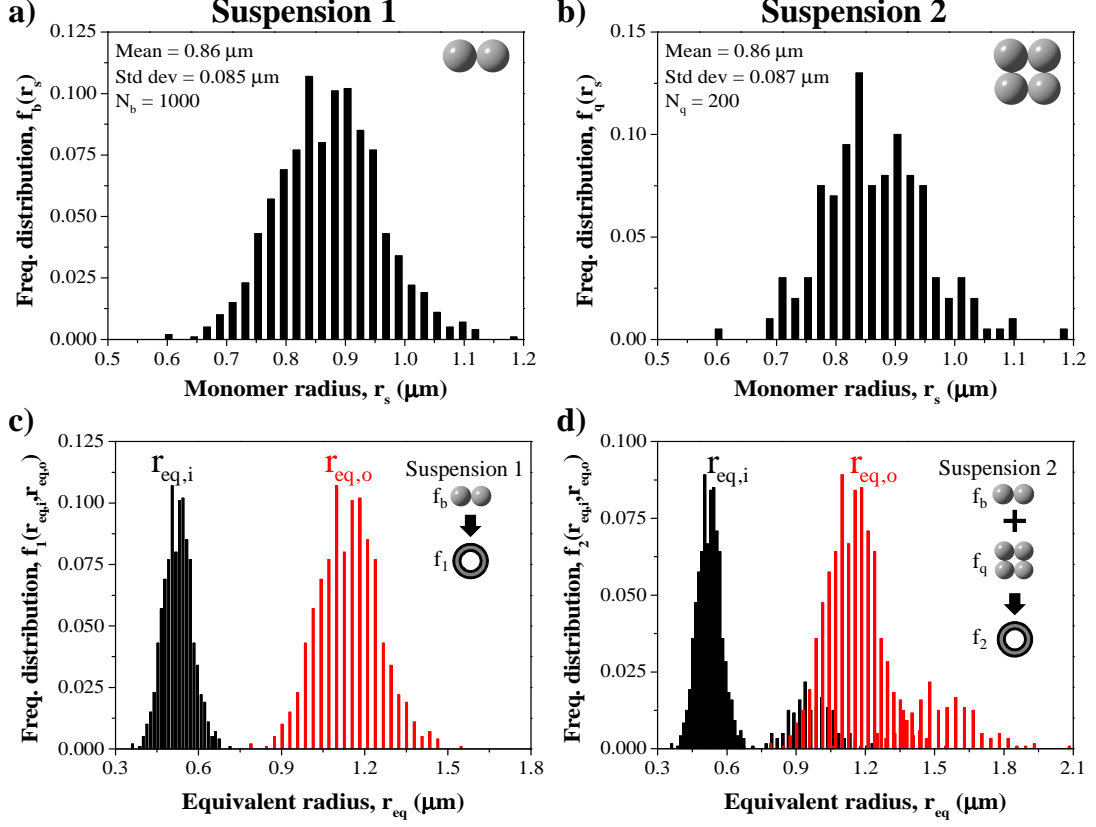


Figure 7.4: Histograms of the bisphere and quadisphere monomer radius frequency distribution and the equivalent coated sphere radii frequency distribution of Suspensions 1 and 2, respectively.

Suspension 1 consisted of $N_b = 1000$ bispheres consisting of two identical spherical monomers of radius frequency distribution $f_b(r_s)$. Suspension 2 was a mixture of aggregates consisting of 1000 bispheres from Suspension 1 and $N_q = 200$ quadispheres with spherical monomers of radius frequency distribution $f_q(r_s)$. These values were chosen based on an estimate of the number of *Synechocystis sp.* cells undergoing cell division during the exponential phase. Figures 7.4a and 7.4b show histograms of the monomer radius frequency distributions $f_b(r_s)$ and $f_q(r_s)$ for the bispheres and quadispheres, respectively. These distributions were then converted into the equivalent coated sphere radii frequency distributions $f_1(r_{eq,i}, r_{eq,o})$ and $f_2(r_{eq,i}, r_{eq,o})$, using Equations (7.3) and (7.4), as shown in Figures 7.4c and

7.4d for Suspensions 1 and 2, respectively. The wavelength of the incident light was taken as constant and equal to 676 nm, corresponding to the *in vivo* absorption peak of Chl *a*. This resulted in monomer size parameters χ_s of the bispheres and quadrspheres ranging from 5 to 11. In addition, the monomers were assigned relative refractive index n_λ ranging from 1.03 to 2.0 and relative absorption index k_λ ranging from 0.004 to 2.0.

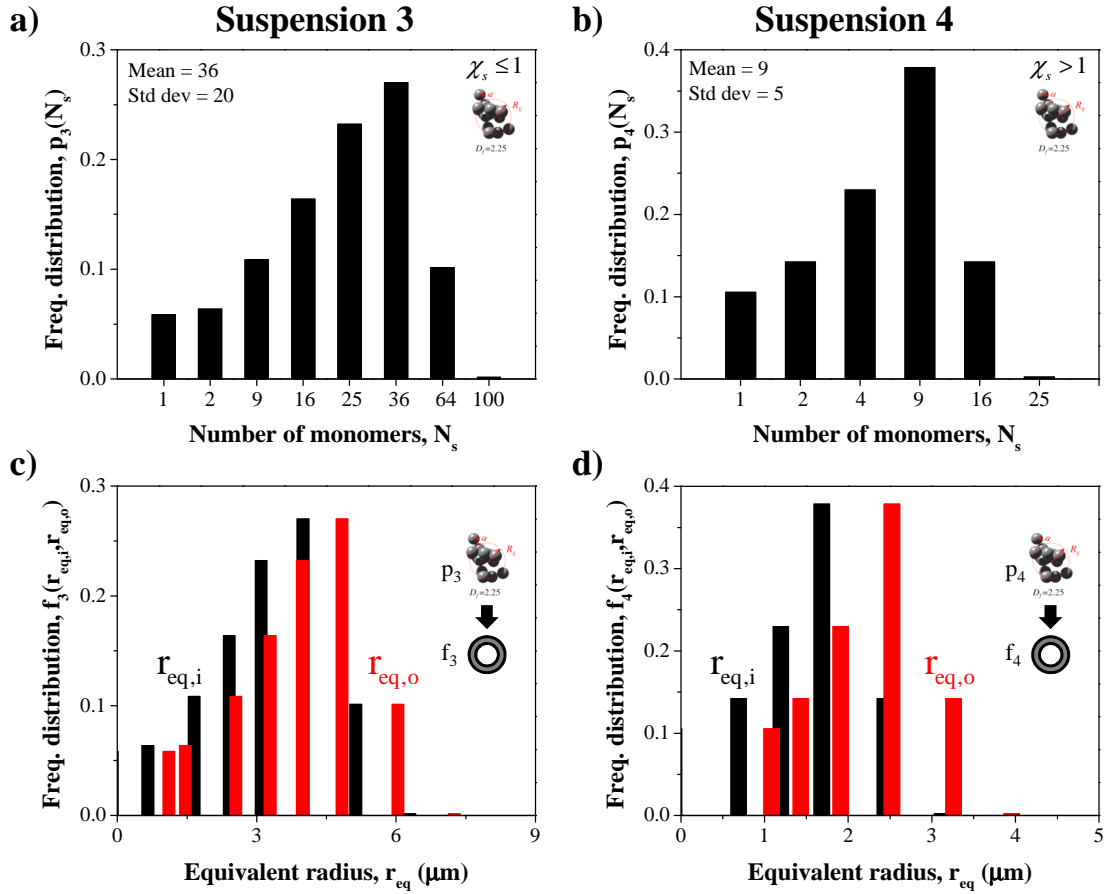


Figure 7.5: Histograms of the monomer number frequency distribution of Suspension 3 and Suspension 4, respectively and of the corresponding equivalent coated sphere radii frequency distribution.

Suspensions 3 and 4 consisted of fractal aggregates composed of monodisperse monomers $1 \mu m$ in radius with monomer number frequency distributions $p_3(N_s)$ and $p_4(N_s)$, respectively. They were generated using the particle cluster aggregation program developed by

Mroczka and co-workers [207–209]. All monomers in the fractal aggregates were in contact with each other but did not overlap. These aggregates featured a fractal dimension D_f of 2.25 and fractal prefactor k_f of 1.59. The former corresponded approximately to that of phytoplankton [210] while the latter corresponded to the most compact packing of monodisperse monomers [206, 208]. Figure 7.5a shows the monomer number frequency distributions $p_3(N_s)$ of Suspension 3 taken as a Gaussian distribution with mean monomer number N_s of 36 monomers and a standard deviation of 20 monomers. The monodisperse monomers were assigned size parameters χ_s of 0.01, 0.1, 0.5, or 1. On the other hand, Figure 7.5b shows the monomer number frequency distributions $p_4(N_s)$ of Suspension 4 composed of monomers of size parameters 5 or 10 and featuring a mean N_s of 9 and a standard deviation of 5 monomers. For both Suspensions 3 and 4, the monomers were assigned a constant relative refractive index n_λ of 1.0165 and relative absorption index k_λ ranging from 0.003 to 0.5. Figures 7.5c and 7.5d show the equivalent coated sphere radii frequency distributions $f_3(r_{eq,i}, r_{eq,o})$ and $f_4(r_{eq,i}, r_{eq,o})$ for Suspensions 3 and 4, respectively.

For each combination of n_λ and k_λ , the absorption $C_{abs,\lambda,j}$ and scattering $C_{sca,\lambda,j}$ cross-sections of randomly oriented aggregate “j” were computed using the T-matrix method [195]. The average absorption $\bar{C}_{abs,\lambda}$ and scattering $\bar{C}_{sca,\lambda}$ cross-sections of the entire suspension was obtained according to

$$\bar{C}_{abs/sca,\lambda} = \frac{1}{N} \sum_{j=1}^N C_{abs/sca,\lambda,j} \quad \text{where } j = 1, 2, \dots, N \quad (7.8)$$

Here, N represented the total number of aggregates in the suspension, i.e., $N = N_b$ for Suspension 1 and $N = N_b + N_q$ for Suspension 2.

Finally, the equivalent coated sphere radii frequency distributions $f(r_{eq,i}, r_{eq,o})$ and the average absorption $\bar{C}_{abs,\lambda}$ and scattering $\bar{C}_{sca,\lambda}$ cross-sections were used in conjunction with the inverse method to retrieve the absorption and scattering indices. These retrieved values $n_{\lambda,pred}$ and $k_{\lambda,pred}$ were compared to the values originally assigned to the monomers based on the sum of their absolute relative errors defined as

$$\epsilon_\lambda = \left| \frac{n_{\lambda,pred} - n_\lambda}{n_\lambda} \right| + \left| \frac{k_{\lambda,pred} - k_\lambda}{k_\lambda} \right| \quad (7.9)$$

7.3 Experimental Methods

7.3.1 Cultivation and sample preparation

The unicellular cyanobacterium *Synechocystis sp.* PCC 6803 was cultivated in F medium [211] in 250 ml culture bottles fitted with vented caps and illuminated from one side by a continuous photosynthetic photon flux density of $91 \mu\text{mol m}^{-2} \text{s}^{-1}$ provided by fluorescent light bulbs (GroLux by Sylvania, USA). The culture was maintained at 30°C throughout the growth and the cell number densities were measured daily using an automatic cell counter (Nexcelom Cellometer Auto M10). To do so, $20 \mu\text{L}$ samples were pipetted from the cultures into disposable haemocytometers (Nexcelom CHT4-SD100). The device counted the number of cells per unit volume N_T using 2D micrographs. Prior to taking a sample, the culture was shaken manually to ensure that it was well-mixed and that the sample was representative of the entire culture volume.

Six days after inoculation, the cultures were observed to be in their exponential growth phase. Then, the suspension was thoroughly shaken and samples of 3 ml were collected to measure their radiation characteristic measurements. To prevent possible absorption and scattering by F medium, the samples were centrifuged at 2,000 rpm (1,300 g) for 8 minutes. Then, the supernatant was replaced with phosphate buffer saline (PBS) solution and the samples were lightly vortexed to resuspend the *Synechocystis sp.* cells.

7.3.2 Size distribution

In order to characterize the size distribution of *Synechocystis sp.*, micrographs of the cells were captured using a 100X microscope connected to a CCD camera. We considered $N_{sp} = 252$ cells and manually measured the radii $r_{s,1}$ and $r_{s,2}$ of the two lobes in each cell using the image analysis software ImageJ, as illustrated in Figure 7.1a. Only the cells whose dumbbell shape could be easily discerned were selected for measurements. The morphology of the cells was simplified to that of bispheres consisting of two identical spherical monomers of radius

$r_s = (r_{s,1} + r_{s,2})/2$ (Figure 7.2a). These measurements led to the *Synechocystis sp.* radius frequency distribution $f_{b,exp}(r_s)$.

7.3.3 Radiation characteristics measurements

7.3.3.1 Assumptions

The following assumptions were made in measuring the scattering phase function and the average absorption and scattering cross-sections of *Synechocystis sp.*: (1) the suspension in the samples were well mixed and the cells were randomly oriented. (2) Single scattering prevailed due to the low cell number densities considered. (3) The scattering phase function had azimuthal symmetry and was only a function of polar angle θ . (4) The scattering phase function of *Synechocystis sp.* cells was assumed to be constant over the PAR region [115] and (5) largely forward scattering because of their large size parameters in the PAR region.

7.3.3.2 Scattering phase function

The scattering phase function of the *Synechocystis sp.* suspension $\Phi_{T,\lambda}(\theta)$ was measured with a polar nephelometer at 633 nm. The experimental setup, data analysis, and validation with latex microspheres were reported in detail by Berberoğlu *et al.* [114,115] and need not be repeated. Due to obstruction by the probe, the scattering phase function for scattering angles θ beyond 170° in the backward direction was not reported.

7.3.3.3 Absorption and scattering coefficients

Normal-normal transmittance of the microorganism suspension, denoted by $T_{n,\lambda}$, was measured in 1 cm pathlength cuvettes using a UV-VIS spectrophotometer (Shimadzu, USA, Model UV-3103PC) from 400 to 750 nm with 1 nm spectral resolution [114]. These measurements were calibrated using the transmittance of the reference medium (i.e., PBS), denoted by $T_{n,\lambda,ref}$, in order to correct for reflection and refraction by the cuvette. The

apparent extinction coefficient χ_λ was defined as [92, 122]

$$\chi_\lambda = -\frac{1}{t} \ln \left(\frac{T_{n,\lambda}}{T_{n,\lambda,ref}} \right) \quad (7.10)$$

Due to the finite acceptance angle of the detector, a fraction ϵ_n of the light scattered in the forward direction was captured by the detector. The experimentally measured scattering phase function $\Phi_{T,\lambda}(\theta)$ can be used to estimate ϵ_n according to [123, 124]

$$\epsilon_n = \frac{1}{2} \int_0^{\theta_a} \Phi_{T,\lambda}(\theta) \sin\theta \, d\theta \quad (7.11)$$

where θ_a is the half acceptance angle of the detector. Then, the apparent extinction coefficient χ_λ can be related to the actual absorption and scattering coefficients according to [123, 124]

$$\chi_\lambda = \sigma_{s,\lambda} + \kappa_\lambda - \epsilon_n \sigma_{s,\lambda} \quad (7.12)$$

Normal-hemispherical transmittance $T_{h,\lambda}$ was also measured with an integrating sphere (ISR-3100 by Shimadzu, USA) and the above mentioned spectrophotometer [114]. After calibrating the measurements with the normal-hemispherical transmittance of the reference medium $T_{h,\lambda,ref}$, the apparent absorption coefficient $\chi_{h,\lambda}$ was defined as

$$\chi_{h,\lambda} = -\frac{1}{t} \ln \left(\frac{T_{h,\lambda}}{T_{h,\lambda,ref}} \right) \quad (7.13)$$

Due to imperfect reflections in the inner surface of the integrating sphere and the geometry of the setup, a fraction of the scattered and transmitted light was unable to reach the detector. In order to account for these phenomena, the apparent absorption coefficient was related to the actual absorption and scattering coefficients by

$$\chi_{h,\lambda} = \kappa_\lambda + (1 - \epsilon_h) \sigma_{s,\lambda} \quad (7.14)$$

where ϵ_h represents the fraction of light captured by the detector and was assumed to be independent of wavelength over the PAR region. It can be estimated by using a wavelength at which *Synechocystis sp.* does not absorb, i.e., 750 nm [145]. At this wavelength, the absorption coefficient $\kappa_{750} = 0 \, \text{m}^{-1}$ and Equation (7.14) simplifies to [123, 124]

$$\epsilon_h = 1 - \frac{\chi_{h,750}}{\sigma_{s,750}} \quad (7.15)$$

Then, combining Equations (7.12), (7.14), and (7.15), the actual spectral absorption coefficient κ_λ can be expressed as [123,124]

$$\kappa_\lambda = \chi_{h,\lambda} - \chi_{h,750} \frac{\chi_\lambda - \chi_{h,\lambda}}{\chi_{750} - \chi_{h,750}} \quad (7.16)$$

Finally, the actual scattering coefficient $\sigma_{s,\lambda}$ was obtained by substituting Equation (7.16) into Equation (7.12).

The samples were manually shaken prior to the transmission measurements to ensure a well mixed suspension with randomly oriented microorganisms. In addition, the measurements were performed for two different cell number densities by diluting the samples with PBS. For each sample, the normal-normal and normal-hemispherical transmittances were measured three times and the results were averaged. Absorption κ_λ and scattering $\sigma_{s,\lambda}$ coefficients were normalized by the cell number density N_T estimated using the automatic cell counter according to Equation (3.4) and (3.5) to obtain the average absorption $\bar{C}_{abs,\lambda}$ and scattering $\bar{C}_{sca,\lambda}$ cross-sections of the suspension. It was established that single and independent scattering prevailed by verifying that the cross-sections $\bar{C}_{abs,\lambda}$ and $\bar{C}_{sca,\lambda}$ for different values of cell densities N_T collapse onto a single line [125].

7.4 Results and discussions

7.4.1 Validation of inverse method

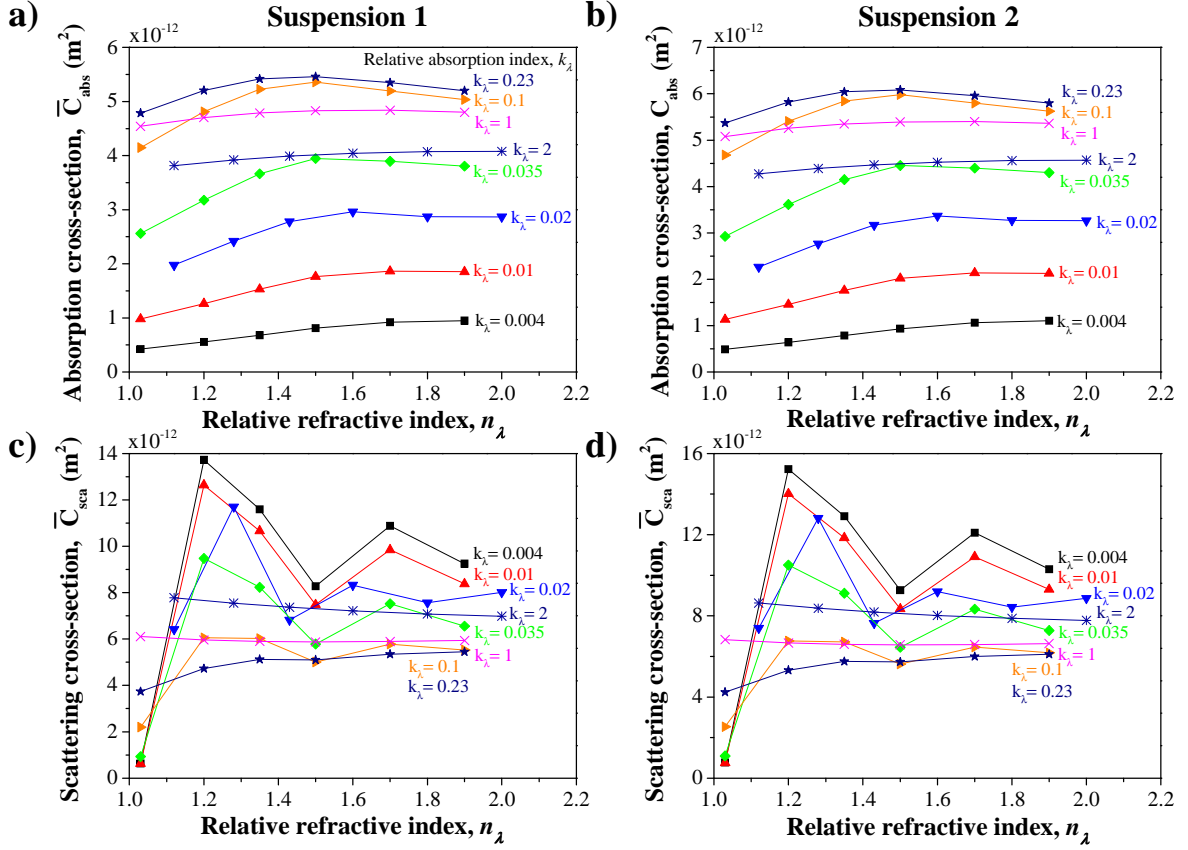


Figure 7.6: (a) and (b) Absorption $\bar{C}_{abs,\lambda}$ and (c) and (d) scattering cross-section $\bar{C}_{sca,\lambda}$ as functions of relative refractive n_λ and absorption k_λ indices for Suspensions 1 and 2, respectively.

Figures 7.6a and 7.6b plots the average absorption cross-sections $\bar{C}_{abs,\lambda}$ of Suspensions 1 and 2 computed using the T-matrix method as functions of the relative refractive n_λ and absorption k_λ indices, respectively. Similarly, Figures 7.6c and 7.6d shows contour plots of the corresponding average scattering cross-sections $\bar{C}_{sca,\lambda}$ of Suspensions 1 and 2, respectively. For given n_λ and k_λ , Suspension 2 had slightly larger $\bar{C}_{abs,\lambda}$ and $\bar{C}_{sca,\lambda}$ than Suspension 1 due to the fact that quadspheres had a larger number of monomers than bispheres. In addition, it was evident that increasing k_λ resulted in larger $\bar{C}_{abs,\lambda}$. However, when k_λ exceeded 0.3, $\bar{C}_{abs,\lambda}$ started decreasing. In this region, a large portion of the incident EM wave was reflected by the monomers without even penetrating the monomers where absorption takes

place. Also, increasing n_λ , for a given value of k_λ , led to a slight increase in $\bar{C}_{abs,\lambda}$. This could be attributed to the fact that the larger index mismatch across the interface between the monomers and the surrounding medium caused EM waves entering the monomers to be confined in the monomers due to total internal refraction. Hence, its attenuation due to EM wave absorption increased. In cases when k_λ was constant, $\bar{C}_{sca,\lambda}$ was observed to oscillate with increasing n_λ . In addition, $\bar{C}_{sca,\lambda}$ decreased and its oscillatory behaviour was damped when k_λ increased. This behaviour is typical of the scattering cross-sections of dielectric scatterers [92].

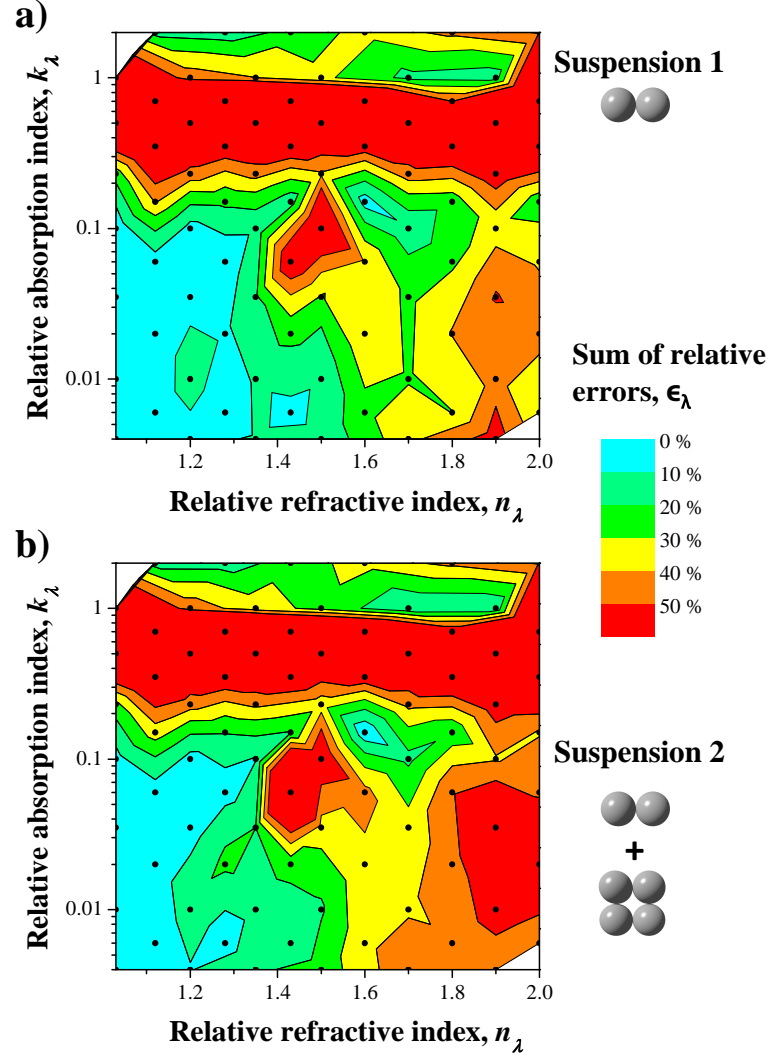


Figure 7.7: Contour plots of the sum of relative errors ϵ between the input and retrieved refraction and absorption index as a function of relative refraction n and absorption index k of the monomers in Suspensions (a) 1 and (b) 2, respectively. The dots on the contour plots represent the location of the computed data points.

The computed average absorption $\bar{C}_{abs,\lambda}$ and scattering $\bar{C}_{sca,\lambda}$ cross-sections were used to retrieve $n_{\lambda,pred}$ and $k_{\lambda,pred}$ by approximating Suspensions 1 and 2 as suspensions of volume and projected area equivalent coated spheres with size distributions $f_1(r_{eq,i}, r_{eq,o})$ and $f_2(r_{eq,i}, r_{eq,o})$, respectively. Figures 7.7a and 7.7b show contour plots of the sum of relative

cumulative error ϵ_λ defined by Equation (7.9) as a function of the input relative refraction n_λ and absorption k_λ indices for Suspensions 1 and 2, respectively. In both cases, the contour plots showed similar trends. The error ϵ_λ was less than 10% for n_λ less than 1.3 and k_λ less than 0.1. It did not exceed 20% when n_λ was between 1.3 and 1.4 and k_λ was less than 0.1. For these ranges of n_λ and k_λ corresponding to optically soft scatterers, the relative errors could be considered acceptable and the inverse method was valid. These results are consistent with analysis of the forward problem indicating that approximations of bispheres and quadspheres by volume and average projected area equivalent coated spheres were valid for $n_\lambda \leq 1.2$ and $k_\lambda \leq 0.1$ for monomer size parameters χ_s ranging from 0.01 to 10 [201]. Note that the relative refractive and absorption indices of photosynthetic microorganisms reported in the literature typically range from 1.01 to 1.1 and from 0.0 and 0.01, respectively [99,177,178]. Therefore, using the inverse method for photosynthetic microorganisms whose morphologies resemble that of bispheres and quadspheres seems appropriate.

Table 7.1: Comparison of (i) the relative refractive n_λ and absorption k_λ indices and size parameter χ_s of the monomers used as input in T-matrix method to compute the average absorption $\bar{C}_{abs,\lambda}$ and scattering $\bar{C}_{sca,\lambda}$ cross-sections in Suspensions 3 and 4 and (ii) those retrieved by inverse method treating the aggregates as homogeneous volume and average projected area equivalent coated spheres.

T-matrix method						Inverse Method		
Suspension	χ_s	n_λ	k_λ	$\bar{C}_{abs,\lambda}$ (μm^2)	$\bar{C}_{sca,\lambda}$ (μm^2)	$n_{\lambda,pred}$	$k_{\lambda,pred}$	ϵ_λ (%)
3	0.01	1.0165	0.003	6.4×10^{-3}	1.2×10^{-8}	1.0173	0.003	0.1
3	0.1	1.0165	0.003	6.5×10^{-2}	8.82×10^{-5}	1.0165	0.0029	4.3
3	0.5	1.0165	0.003	0.33	1.2×10^{-2}	1.0178	0.003	0.8
3	1	1.0165	0.003	0.66	7.1×10^{-2}	1.0176	0.003	1.4
3	1	1.0165	0.03	6.17	0.27	1.0234	0.029	5.0
3	1	1.0165	0.07	13.2	1.07	1.0383	0.065	9.1
3	1	1.0165	0.5	48.0	19.8	1.0005	0.474	6.8
4	5	1.0165	0.003	0.88	0.43	1.0166	0.0032	6.7
4	10	1.0165	0.003	1.7	1.71	1.0162	0.003	0.7

Table 7.1 shows the relative refractive n_λ and absorption k_λ indices used in predicting the average absorption $\bar{C}_{abs,\lambda}$ and scattering $\bar{C}_{sca,\lambda}$ cross-sections of Suspensions 3 and 4 using the T-matrix method as well as those retrieved by the inverse method $n_{\lambda,pred}$ and $k_{\lambda,pred}$. Each suspension featured aggregates with monomer number frequency distributions $p_3(N_s)$ and $p_4(N_s)$ shown in Figures 7.5a and 7.5b. The aggregates had fractal dimension D_f of 2.25 and were composed of monodisperse monomers of size parameter χ_s equals to 0.01, 0.1, 0.5, or 1 for Suspension 3 and 5 or 10 for Suspension 4. The monomer relative refraction index n_λ was equal to 1.0165 and the relative absorption index k_λ was taken as 0.003, 0.03, 0.07, or 0.5. The sum of relative differences between the assigned and retrieved refraction and absorption indices ϵ_λ was less than 9.1% for all cases considered. The error was smaller

for aggregates composed of optically soft monomers with small absorption index. On the other hand, the relative error in the retrieved complex index of refraction did not show any obvious trend with monomer size parameter. This demonstrates the capability of the inverse method to retrieve the relative complex index of refraction of fractal aggregates based on the volume and average projected area equivalent coated sphere approximation and their average absorption $\bar{C}_{abs,\lambda}$ and scattering $\bar{C}_{sca,\lambda}$ predicted by the T-matrix method. It also confirms that the method can be applied to photosynthetic microorganisms with a wide range of morphologies and size parameters and such that $1.0 \leq n_\lambda \leq 1.1$ and $0 \leq k_\lambda \leq 0.01$.

7.4.2 Experimental results

7.4.2.1 Size distribution

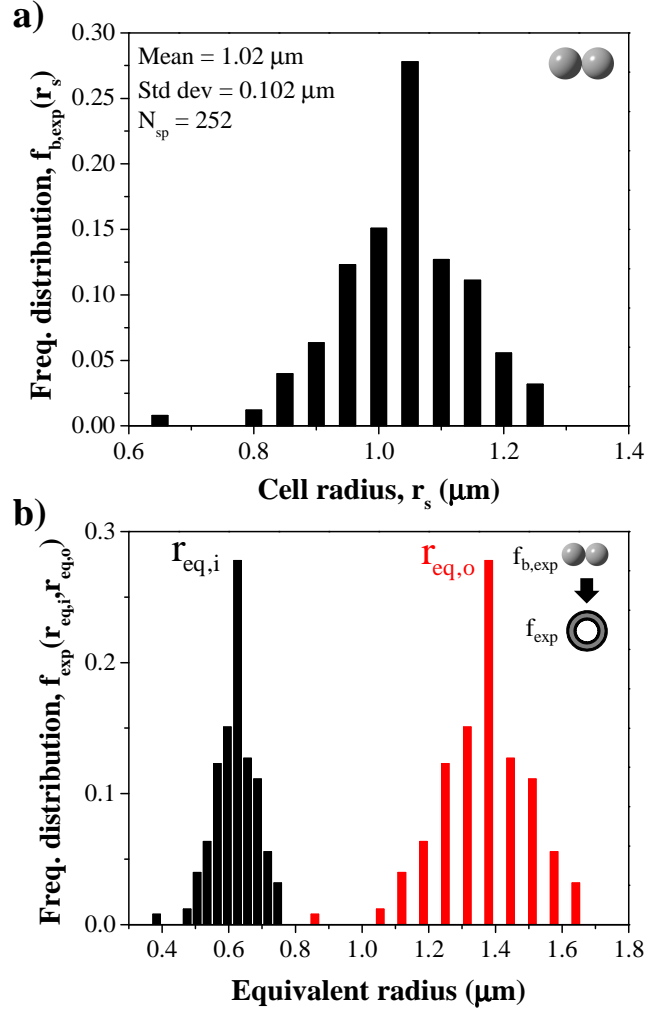


Figure 7.8: Histograms of (a) the measured *Synechocystis sp.* radius distribution $f_{b,exp}(r_s)$ and of (b) the equivalent coated sphere radii distribution $f_{exp}(r_{eq,i}, r_{eq,o})$.

Figure 7.8a shows a histogram of the radius frequency distribution $f_{b,exp}(r_s)$ of the *Synechocystis sp.* grown experimentally with bin size of 0.05 μm and mean radius of 1.02 μm . For each of these cells, the two radii $r_{s,1}$ and $r_{s,2}$ were found to fall within 20% of each other. Hence, treating the cells as bispheres with identical monomers of radius r_s taken as the average of $r_{s,1}$ and $r_{s,2}$ was reasonably accurate. Figure 7.8b shows a histogram of the equivalent coated sphere radii distribution $f_{exp}(r_{eq,i}, r_{eq,o})$ converted from $f_{b,exp}(r_s)$.

7.4.2.2 Scattering phase function

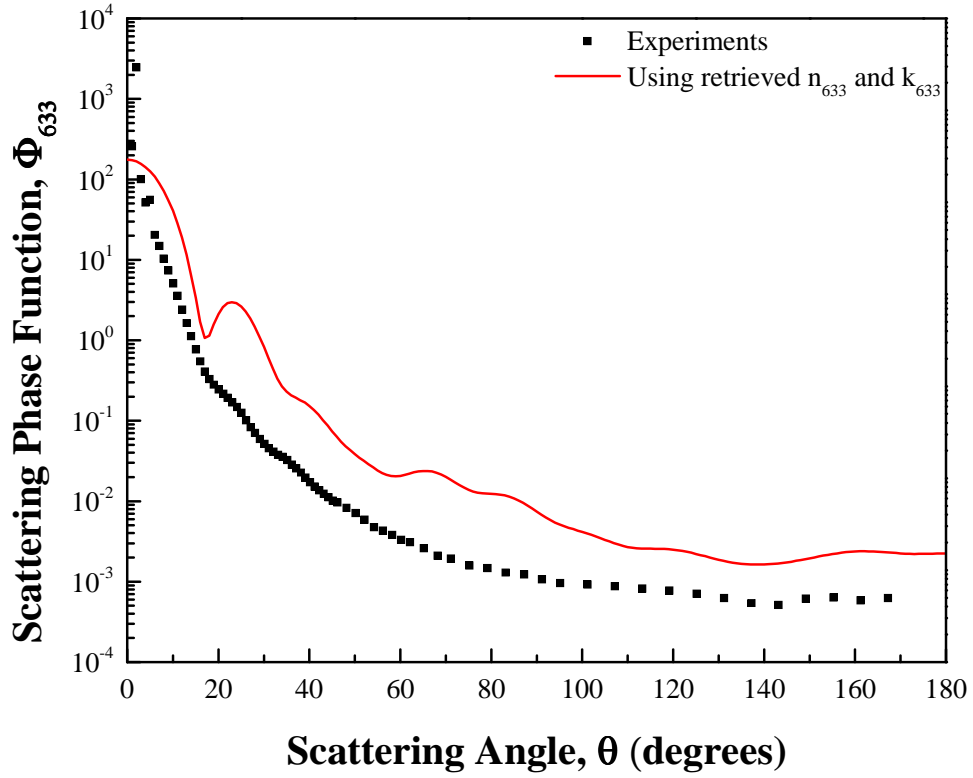


Figure 7.9: Scattering phase function of *Synechocystis sp.* at 633 nm as a function of scattering angle θ from 0 to 180° measured experimentally using a polar nephelometer and predicted using the equivalent coated sphere approximation in conjunction with $f_{exp}(r_{eq,i}, r_{eq,o})$, plotted in Figure 8, and n_{633} and k_{633} , retrieved using the inverse method.

Figure 7.9 shows the scattering phase function of *Synechocystis sp.* measured at 633 nm. As expected, scattering was strongly in the forward direction due to the large size parameters of the cells $\chi_s \approx 10$. In addition, the asymmetry factor g_{633} was estimated to be 0.993.

7.4.2.3 Mass absorption and scattering cross-sections

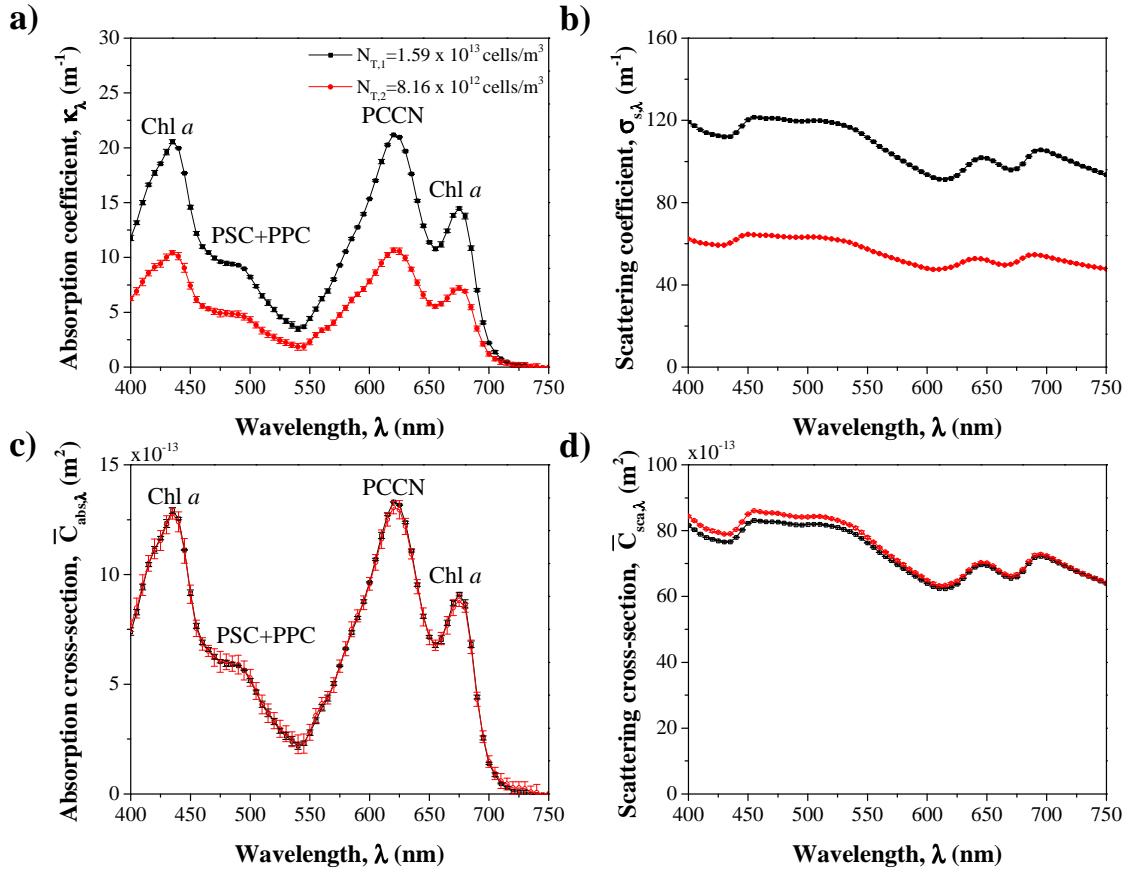


Figure 7.10: Measured (a) absorption coefficient κ_λ , (b) scattering coefficient $\sigma_{s,\lambda}$, (c) average absorption cross-section $\bar{C}_{abs,\lambda} = \kappa_\lambda/N_T$, and (d) average scattering cross-section $\bar{C}_{sca,\lambda} = \sigma_{s,\lambda}/N_T$ of *Synechocystis sp.* as functions of wavelength λ from 400 to 750 nm for cell number densities $N_{T,1} = 1.89 \times 10^{13}$ cells/m³ and $N_{T,2} = 8.16 \times 10^{12}$ cells/m³.

Figures 7.10a and 7.10b respectively show the spectral absorption κ_λ and scattering $\sigma_{s,\lambda}$ coefficients measured in the spectral range from 400 to 750 nm for *Synechocystis sp.* collected after 6 days of growth for cell number densities $N_{T,1} = 1.89 \times 10^{13}$ cells/m³ and $N_{T,2} = 8.16 \times 10^{12}$ cells/m³. Each data point represents the arithmetic mean of κ_λ and $\sigma_{s,\lambda}$ measured three times for each cell number density while the error bars correspond to 95% confidence interval. It is evident that the sample with larger cell number density $N_{T,1}$ had larger coefficients κ_λ and $\sigma_{s,\lambda}$.

Figures 7.10c and 7.10d show the average absorption $\bar{C}_{abs,\lambda}$ and scattering $\bar{C}_{sca,\lambda}$ cross-sections in the spectral range from 400 to 750 nm after normalizing κ_λ and $\sigma_{s,\lambda}$, shown in Figures 7.10a and 7.10b, by their respective cell number density N_T , according to Equation (3.4) and (3.5). Both datasets collapse on a single line confirming that single and independent scattering prevailed and that the cross-sections were directly proportionate to cell number density. Moreover, both the absorption coefficient κ_λ and the cross-section $\bar{C}_{abs,\lambda}$ of *Synechocystis sp.* featured peaks (i) at 435 and 676 nm corresponding to the absorption peaks of Chl *a* [4], (ii) at 625 nm corresponding to that of PCCN [212], and (iii) a shoulder around 485 nm corresponding to absorption by PSC and PPC [4]. The scattering coefficient $\sigma_{s,\lambda}$ and the scattering cross-section $\bar{C}_{sca,\lambda}$ featured resonance peaks and dips around wavelengths corresponding to the absorption peaks.

7.4.2.4 Effective optical properties of *Synechocystis sp.*

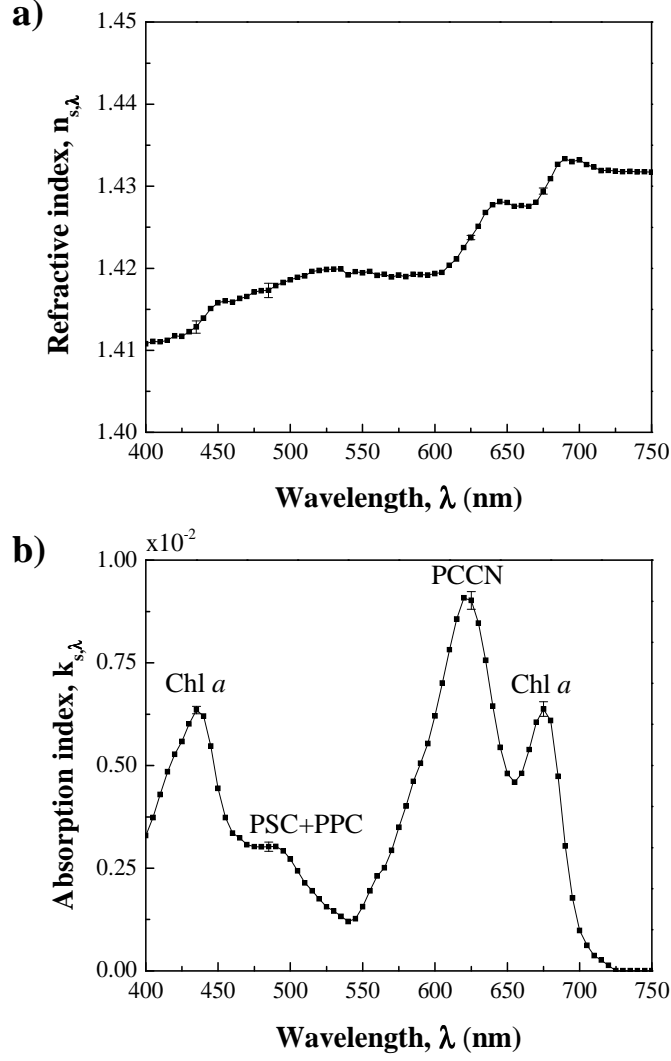


Figure 7.11: Retrieved effective (a) refraction n_λ and (b) absorption k_λ indices of *Synechocystis sp.* as functions of wavelength λ from 400 to 750 nm using the inverse method shown in Figure 3 with $f_{exp}(r_{eq,i}, r_{eq,o})$, $\bar{C}_{abs,\lambda}$, and $\bar{C}_{sca,\lambda}$ plotted in Figures 8 and 10, respectively.

Figure 7.11 shows (a) the effective refraction index $n_{s,\lambda}$ and (b) the effective absorption index $k_{s,\lambda}$ of *Synechocystis sp.* between 400 and 750 nm retrieved from (i) the measured average absorption and scattering cross-sections $\bar{C}_{abs,\lambda}$ and $\bar{C}_{sca,\lambda}$, (ii) the equivalent coated sphere radii distribution $f_{exp}(r_{eq,i}, r_{eq,o})$, and (iii) the refraction index of PBS given by the Cauchy

dispersion relation [100]

$$n_{m,\lambda} = 1.32711 + \frac{0.0026}{\lambda^2} + \frac{0.00005}{\lambda^4} \quad (7.17)$$

where the wavelength λ is expressed in μm . The error bars were estimated from error propagation analysis at wavelengths close to the pigment absorption peaks. Although each pair $(n_{s,\lambda}, k_{s,\lambda})$ was retrieved for each individual wavelength, the results feature $n_{s,\lambda}$ and $k_{s,\lambda}$ as continuous functions of wavelength. In addition, the absorption index $k_{s,\lambda}$ also featured the same absorption peaks as those observed in κ_λ and $\bar{C}_{abs,\lambda}$ corresponding to Chl *a*, PCCN, and carotenoids. The refraction index $n_{s,\lambda}$ featured resonance peaks and dips around wavelengths corresponding to the peaks in k_λ . The values of the retrieved absorption index $k_{s,\lambda}$ were consistent with those found for other photosynthetic microorganisms [177, 178]. However, the retrieved values of refraction index $n_{s,\lambda}$ was found to be larger. In fact, the refraction index $n_{s,\lambda}$ of cyanobacteria *A. cylindrica* [178] and several hydrogen and lipid producing microalgae [177] ranged between 1.35 and 1.36. The difference in $n_{s,\lambda}$ can be attributed to the difference in composition of these microorganisms. For example, cells with higher water content would have lower values of $n_{s,\lambda}$ while large lipid, protein, and carbohydrate contents as well as cell walls would result in large effective refractive index [131].

Moreover, the retrieved refractive and absorption indices at 633 nm and $f_{exp}(r_{eq,i}, r_{eq,o})$ were used in the forward method to predict the scattering phase function of *Synechocystis sp.* treated as polydisperse projected area and volume equivalent coated spheres. Figure 7.9 shows the predicted scattering phase function with respect to the scattering angle θ . As expected, both the predicted and measured scattering phase functions were largely forward scattering. The predicted asymmetry factor was 0.973 compared with 0.993 measured experimentally.

7.5 Chapter summary

An inverse method was developed to retrieve the absorption and refraction indices from the absorption and scattering cross-sections of multicellular cyanobacteria with bisphere or

quadsphere morphologies and fractal aggregates of unicellular microalgae. The method was validated using absorption and scattering cross-sections computed for four different suspensions consisting of bispheres, quadspheres, and fractal aggregates. The inverse method was found to accurately retrieve the monomer complex index of refraction for relative refraction index less than 1.3 and relative absorption index less than 0.1. This paper also reported the scattering phase function, absorption and scattering cross-sections of *Synechocystis sp.* measured experimentally from 400 to 750 nm during the exponential growth phase in F medium. Their optical properties were also retrieved by approximating *Synechocystis sp.* cells as homogeneous average projected area and volume equivalent coated spheres. Both the absorption cross-section and the absorption index featured distinct peaks corresponding to chlorophyll *a* and phycocyanin and a shoulder around 485 nm corresponding to carotenoids. These results can be used for predicting light distribution in photobioreactors cultivating *Synechocystis sp.*. In addition, the inverse method can be used for other similar and optically soft aggregates.

CHAPTER 8

Summary

The objective of the study was to characterize and optimize light transfer in photobioreactors in order to improve biofuel production rates. To achieve this, the radiation characteristics of photosynthetic microorganisms were essential parameters and could be obtained either through experimental measurements or model predictions. The following summarizes the tasks carried out in order to meet this objective.

The unicellular green algae *Botryococcus braunii*, *Chlorella sp.*, and *Chlorococcum littorale* were treated as homogeneous polydisperse spheres with equivalent diameter such that their surface area was identical to that of their actual spheroidal shape. Based on this approximation, their spectral complex index of refraction between 400 and 750 nm were retrieved from their experimentally measured average absorption and scattering cross-sections. The inverse method used in the retrieval process was developed by combining Lorentz-Mie theory as the forward method and genetic algorithm.

Next, the temporal evolution of the scattering and absorbing cross-sections of marine eustigmatophycease *Nannochloropsis oculata* grown in flat-plate photobioreactor (PBR) was reported. The radiation characteristics between 400 and 750 nm and pigment concentrations of *N. oculata* were measured systematically every 24 hours for up to 18 days. They were found to vary significantly with time in response to changes in light and nutrients availability. The results were interpreted in terms of up- and down-regulations of pigments and other intracellular components. Finally, this study demonstrates that the light transfer in the PBR could be predicted using constant radiation characteristics measured during the exponential growth phase with reasonable accuracy provided that the cultures were not nitrogen limited.

During nitrogen starvation, pigment concentrations decreased and radiation characteristics evolved rapidly.

In addition, this study presents experimental measurements of the absorption and scattering cross-sections and the spectral complex index of refraction of filamentous cyanobacterium *Anabaena cylindrica*. Its filaments consisted of long chains of polydisperse cells. Their average mass scattering and absorption cross-sections were measured from 400 to 750 nm at four different times during their batch growth. The spectral complex index of refraction were retrieved using an inverse method based on genetic algorithm. The microorganisms were modeled as infinitely long and randomly oriented volume-equivalent cylinders. The absorption index featured peaks corresponding to chlorophyll *a* (Chl *a*) at 436 and 676 nm and phycocyanin (PCCN) at 630 nm and a shoulder around 480 nm corresponding to photoprotective carotenoids. The absorption peaks of Chl *a* and PCCN concentrations increased and the shoulder due to carotenoids decreased in response to photolimitation caused by biomass growth. Subsequent nitrogen limitation caused the PCCN absorption peak to decrease significantly due to degradation of PCCN as an endogenous source of nitrogen for nitrogenase maintenance and synthesis, as confirmed by increasing heterocyst differentiation.

Furthermore, this study demonstrates that the absorption and scattering cross-sections and asymmetry factor of randomly oriented and optically soft bispheres, quadrspheres, and circular rings of spheres, with either monodisperse or polydisperse monomers, can be approximated by an equivalent coated sphere with identical volume and average projected area. This approximation could also apply to the angle-dependent scattering matrix elements for monomer size parameter less than 0.1. However, it quickly deteriorated with increasing monomer number and/or size parameter. It was shown to be superior to previously proposed approximations considering a volume equivalent homogeneous sphere and a coated sphere with identical volume and surface area. Based on this approximation an inverse method for retrieving the optical properties of photosynthetic microorganisms was developed by integrating genetic algorithm with the Lorenz-Mie theory for coated spheres. The method was validated for a range of refraction and absorption indices using average

absorption and scattering cross-sections computed numerically for different suspensions consisting of bispheres, quadspheres, and fractal aggregates. In addition, this study presents the experimentally measured average absorption and scattering cross-sections, size distribution, and scattering phase function of cyanobacterium *Synechocystis sp.*. The dumbbell shaped *Synechocystis sp.* cells were treated as randomly oriented homogeneous bispheres and their spectral complex index of refraction was retrieved using the inverse method.

Overall, these results can be used to predict light transfer in PBRs hence leading to their optimizations. This would also enable better control over the PBR operating conditions. The approximate models used to predict the radiation characteristics for microorganisms of different morphologies can provide a fast and accurate alternative to experimental measurements. This can be useful when screening many different species of microorganisms for their biofuel potentials.

REFERENCES

- [1] P.S. Sharma, “Algae biodiesel tremendous potential for next-generation green energy”, <http://saferenvironment.wordpress.com/2008/10/03/algae-tremendous-potential-for-next-generation-green-energy-%E2%80%93-93-%E2%80%93algae-biodiesel%E2%80%93/>, 2008.
- [2] L. Pilon, H. Berberoglu, and R. Kandilian, “Radiation transfer in photobiological carbon dioxide fixation and fuel production by microalgae”, *Journal of Quantitative Spectroscopy & Radiative Transfer*, vol. 112, pp. 2639–2660, 2011.
- [3] C. Gueymard, D. Myers, and K. Emery, “Proposed reference irradiance spectra for solar energy systems testing”, *Solar Energy*, vol. 73, no. 6, pp. 443–467, 2002.
- [4] R. Bidigare, M. Ondrusek, J. Morrow, and D. Kiefer, “In vivo absorption properties of algal pigments”, *Ocean Optics X*, vol. 1302, pp. 290–301, 1990.
- [5] H. Berberoğlu, P.S. Gomez, and L. Pilon, “Radiation characteristics of *Botryococcus braunii*, *Chlorococcum littorale*, and *Chlorella sp.* used for CO₂ fixation and biofuel production”, *Journal of Quantitative Spectroscopy and Radiative Transfer*, vol. 110, pp. 1879–1893, 2009.
- [6] Y. Chisti, “Biodiesel from microalgae”, *Biotechnology Advances*, vol. 25, no. 3, pp. 294–306, 2007.
- [7] C.U. Ugwu, H. Aoyagi, and H. Uchiyama, “Photobioreactors for mass cultivation of algae”, *Bioresource Technology*, vol. 99, pp. 4021–4028, 2008.
- [8] Intergovernmental Panel on Climate Change, *Climate Change 1992: The Supplementary Report To The Ipcc Scientific Assessment*, Press Syndicate of the University of Cambridge, Cambridge UK, 1992.
- [9] BP p.l.c., “Bp energy outlook 2030”, http://www.bp.com/liveassets/bp_internet/globalbp/STAGING/global_assets/downloads/0/2012_2030_energy_outlook_booklet.pdf, 2012.
- [10] Paris: International Energy Agency, “World energy outlook 2007”, http://www.iea.org/textbase/nppdf/free/2007/weo_2007.pdf, 2007.
- [11] R. Luque, J. Campelo, and J. Clark, *Handbook of biofuels production*, Woodhead Publishing Limited, Cambridge UK, 2011.
- [12] Alternative Fuels Data Center, “Ethanol fuel basics”, http://www.afdc.energy.gov/fuels/ethanol_fuel_basics.html, 2012.
- [13] W. Seifritz, “Co₂ disposal by means of silicates”, *Nature*, vol. 345, pp. 486, 1990.

- [14] H. Berberoğlu, “Photobiological hydrogen production and carbon dioxide sequestration”, 2008.
- [15] C.C. Winterbourn, “Comparison of superoxide with other reducing agents in the biological production of hydroxyl radicals”, *Biochem J.*, vol. 182, no. 2, pp. 625–628, 1979.
- [16] T. Kondo, M. Arakawa, T. Wakayama, and J. Miyake, “Hydrogen production by combining two types of photosynthetic bacteria with different characteristics”, *International Journal of Hydrogen Energy*, vol. 27, no. 11-12, pp. 1303–1308, 2002.
- [17] B. Ke, *Photosynthesis, Photobiocchemistry and Photobiophysics*, Kluwer Academic Publishers, Dordrecht, The Netherlands, 2001.
- [18] C.P. Wolk, J. Thomas, and P.W. Shaffer, “Pathway of nitrogen metabolism after fixation of ^{13}N -labeled nitrogen gas by the cyanobacterium, *Anabaena cylindrica*”, *Biochemical And Biophysical Research Communications*, vol. 65, no. 3, pp. 846–856, 1975.
- [19] Q. Hu, M. Sommerfeld, E. Jarvis, M. Ghirardi, M. Posewitz, M. Seibert, and A. Darzins, “Microbial triacylglycerols as feedstocks for biofuel production: perspectives and advances”, *The Plant Journal*, vol. 54, pp. 621–639, 2008.
- [20] J. Ohlrogge and J. Browse, “Lipid biosynthesis”, *Plant Cell*, vol. 7, pp. 957–970, 1995.
- [21] C. Ratledge, “An Overview of Microbial Lipids”, in *In Microbial Lipids*, C. Ratledge and S.G. Wilkerson, Eds., vol. 1. Academic Press, New York, NY, 1988.
- [22] A. Sukenik, Y. Yamaguchi, and A. Livne, “Alterations in lipid molecular species of the marine eustigmatophyte *Nannochloropsis sp.*”, *Journal of Phycology*, vol. 29, pp. 620–626, 1993.
- [23] D.M. Orcutt and G.W. Patterson, “Effect of light intensity upon *Nitzschia closterium* (*Cylindrotheca fusiformis*)”, *Lipids*, vol. 9, pp. 1000–1003, 1974.
- [24] J.C. Weissman and J.R. Benemann, “Hydrogen production by nitrogen-starved cultures of *Anabaena cylindrica*”, *Applied and Environmental Microbiology*, vol. 33, no. 1, pp. 123–131, 1977.
- [25] L. Rodolfi, G.C. Zittelli, N. Bassi, G. Padovani, N. Biondi, G. Bonini, and M.R. Tredici, “Microalgae for oil: Strain selection, induction of lipid synthesis and outdoor mass cultivation in a low-cost photobioreactor”, *Biotechnology and Bioengineering*, vol. 102, no. 1, pp. 100–112, 2009.
- [26] O. Pulz and W. Gross, “Valuable products from biotechnology of microalgae”, *Applied Microbiology and Biotechnology*, vol. 65, no. 6, pp. 635–648, 2004.

- [27] A. Richmond, *Handbook of Microalgal Culture: Biotechnology and Applied Phycology*, Blackwell Science Ltd, Oxford, UK, 2004.
- [28] B. Wang, Y. Li, N. Wu, and C.Q. Lan, “CO₂ bio-mitigation using microalgae”, *Applied Microbiology and Biotechnology*, vol. 79, no. 5, pp. 707–718, 2008.
- [29] NASA, “Sun: Facts & figures”, <http://solarsystem.nasa.gov/planets/profile.cfm?Display=Facts&Object=Sun>.
- [30] J.A. Duffie and W.A. Beckman, *Solar Engineering of Thermal Processes*, John Wiley and Sons, Hoboken, New Jersey, 3rd edition, 2006.
- [31] J.S. Burlew, *Algal Culture from Laboratory to Pilot Plant*, Carnegie Institution of Washington, Washington, DC, 1953.
- [32] H.H. Khoo, P.N. Sharratt, P. Das, R.K. Balasubramanian, P.K. Naraharisetti, and S. Shaik, “Importance of algal oil as a source of biodiesel”, *Bioresource Technology*, vol. 102, pp. 5800–5807, 2011.
- [33] M.J. Griffiths and S. Harrison, “Lipid productivity as a key characteristic for choosing algal species for biodiesel production”, *Applied and Environmental Microbiology*, vol. 33, no. 1, pp. 123–131, 1977.
- [34] E.M. Grima, E.-H. Belarbi, F.G.A. Fernandez, A.R. Medina, and Y. Chisti, “Recovery of microalgal biomass and metabolites: process options and economics”, *Biotechnology Advances*, Year = 2003, Volume = 20, Pages = 491-515,.
- [35] A. Demirbas and M.F. Demirbas, “Importance of algal oil as a source of biodiesel”, *Energy Conversion and Management*, vol. 52, pp. 163–170, 2011.
- [36] J.U. Grobbelaar, “Physiological and technological considerations for optimising mass algal cultures”, *Journal of Applied Phycology*, vol. 12, no. 3-5, pp. 201–206, 2000.
- [37] N.T. Eriksen, “The technology of microalgal culturing”, *Biotechnology Letters*, vol. 30, no. 9, pp. 1525–1536, 2008.
- [38] J.H. Yoon, S.J. Sim, M.S. Kim, and T.H. Park, “High cell density culture of *Anabaena variabilis* using repeated injections of carbon dioxide for the production of hydrogen”, *International Journal of Hydrogen Energy*, vol. 27, pp. 1265–1270, 2002.
- [39] A. Melis, J. Neidhardt, and J.R. Benemann, “*Dunaliella salina* (Chlorophyta) with small chlorophyll antenna sizes exhibit higher photosynthetic productivities and photon use efficiencies than normally pigmented cells”, *Journal of Applied Phycology*, vol. 10, no. 6] Pages = 515-525,, 1999.
- [40] J.R. Benemann, “Hydrogen production by microalgae”, *Journal of Applied Phycology*, vol. 12, no. 3-5, pp. 291–300, 2000.

- [41] E.H. Harris, *The Chlamydomonas Sourcebook - Volume 1*, Academic Press, San Diego, CA, 1989.
- [42] L.J. Wang and C.L. Weller, “Recent advances in extraction of nutraceuticals from plants”, *Trends in Food Science & Technology*, vol. 17, no. 6, pp. 300–312, 2006.
- [43] A. Hosikian, S. Lim, R. Halim, and M.K. Danquah, “Chlorophyll extraction from microalgae: A review on the process engineering aspects”, *International Journal of Chemical Engineering*, vol. 2010, pp. 11, 2010.
- [44] R.J. Porra, W.A. Thompson, and P.E. Kriedemann, “Determination of accurate extinction coefficients and simultaneous equations for assaying chlorophylls a and b extracted with four different solvents: verification of the concentration of chlorophyll standards by atomic absorption spectroscopy”.
- [45] R. Ritchie, “Consistent sets of spectrophotometric chlorophyll equations for acetone, methanol and ethanol solvents”, *Photosynthesis Research*, vol. 89, no. 1, pp. 27–41, 2006.
- [46] M.F. Modest, *Radiative heat transfer*, Academic Press, San Diego, CA, 2003.
- [47] H. Berberoğlu, J. Yin, and L. Pilon, “Simulating light transfer in a bubble sparged photobioreactor for simultaneous hydrogen fuel production and CO_2 mitigation”, *International Journal of Hydrogen Energy*, vol. 32, no. 13, pp. 2273–2285, 2007.
- [48] H. Berberoğlu and L. Pilon, “Experimental measurement of the radiation characteristics of *Anabaena variabilis* ATCC 29413-U and *Rhodobacter sphaeroides* ATCC 49419”, *International Journal of Hydrogen Energy*, vol. 32, no. 18, pp. 4772–4785, 2007.
- [49] L. Pottier, J. Pruvost, J. Deremetz, J.F. Cornet, J. Legrand, and C.G. Dussap, “A fully predictive model for one-dimensional light attenuation by *Chlamydomonas reinhardtii* in a torous photobioreactor”, *Biotechnology and Bioengineering*, vol. 91, pp. 569–582, 2005.
- [50] J-F. Cornet and C-G. Dussap, “A simple and reliable formula for assessment of maximum volumetric productivities in photobioreactors”, *Biotechnology Progress*, vol. 25, no. 2, pp. 424–435, 2009.
- [51] D. Stramski and C.D. Mobley, “Effect of microbial particles on oceanic optics: a database of single-particle optical properties”, *Limnology and Oceanography*, vol. 42, pp. 538–549, 1997.
- [52] K.J. Daniel, N.M. Laurendeau, and F.P. Incropera, “Prediction of radiation absorption and scattering in turbid water bodies”, *ASME Journal of Heat Transfer*, vol. 101, pp. 63–67, 1979.

- [53] B.M. Agrawal and M.P. Mengüç, “Forward and inverse analysis of single and multiple scattering of collimated radiation in an axisymmetric system”, *International Journal of Heat and Mass Transfer*, vol. 34, pp. 633–647, 1991.
- [54] M. Jonasz and G.R. Fournier, *Light Scattering by Particles in Water: Theoretical and Experimental Foundations*, Academic Press, San Diego, CA, 2007.
- [55] R.R. Bidigare, R.C. Smith, K.S. Baker, and J. Marra, “Oceanic primary production estimates from measurements of spectral irradiance and pigment concentrations”, *Global Biogeochemical Cycles*, vol. 1, pp. 171–186, 1987.
- [56] A. Quirantes A and S. Bernard, “Light scattering by marine algae: two-layer spherical and nonspherical models”, *Journal of Quantitative Spectroscopy and Radiative Transfer*, vol. 89, no. 1-4, pp. 311–321, 2004.
- [57] A. Bricaud and A. Morel, “Light attenuation and scattering by phytoplanktonic cells: A theoretical modeling”, *Applied Optics*, vol. 25, pp. 571–580, 1986.
- [58] S. Bernard, T.A. Probyn, and R.G. Barlow, “Measured and modelled optical properties of particulate matter in the southern benguela”, *South African Journal of Science*, vol. 97, pp. 410–420, 2001.
- [59] D. Stramski, A. Bricaud, and A. Morel, “Modeling the inherent optical properties of the ocean based on the detailed composition of planktonic community”, *Applied Optics*, vol. 40, pp. 2929–2945, 2001.
- [60] C.F. Bohren and D.R. Huffman, *Absorption and Scattering of Light by Small Particles*, John Wiley & Sons, New York, NY, 1998.
- [61] H.C. Van De Hulst, *Light Scattering by Small Particles*, Wiley, New York, NY, 1957.
- [62] A. Bricaud, J. Ronald, V. Zaneveld, and J.C. Kitchen, “Backscattering efficiency of coccolithophorids: use of a three-layered sphere model”, *Proceedings of SPIE*, vol. 1750, pp. 27–33, 1992.
- [63] J. Ronald, V. Zaneveld, and J.C. Kitchen, “The variation in the inherent optical properties of phytoplankton near an absorption peak as determined by various models of cell structure”, *Proceedings of SPIE*, vol. 100, pp. 13309–13320, 1995.
- [64] M.I. Mishchenko, J.W. Hovenier, and L.D. Travis, *Light Scattering by Nonspherical Particles*, Academic Press, San Diego, CA, 2000.
- [65] H. Berberoğlu H, A. Melis, and Pilon L., “Radiation characteristics of *Chlamydomonas reinhardtii* CC125 and its truncated chlorophyll antenna transformants *tla1*, *tlaX*, and *tla1-CW⁺*”, *International Journal of Hydrogen Energy*, vol. 33, no. 22, pp. 6467–6483, 2008.

- [66] P. Gerhardt, T. C. Beaman, T. R. Corner, J. T. Greenamyre, and L. S. Tisa, “Photometric immersion refractometry of bacterial spores”, *Journal of Bacteriology*, vol. 150, pp. 643–648, 1982.
- [67] M. Jonasz, G. Fournier, and D. Stramski, “Photometric immersion refractometry: a method for determining the refractive index of marine microbial particles from beam attenuation”, *Applied Optics*, vol. 36, no. 18, pp. 4214–4225, 1997.
- [68] F.D. Bryant, B.A. Seiber, and P. Latimer, “Absolute optical cross sections of cells and chloroplasts”, *Archives of Biochemistry and Biophysics*, vol. 135, pp. 79–108, 1969.
- [69] R.E. Green, H.M. Sosik, R.J. Olson, and M.D. Durand, “Flow cytometric determination of size and complex refractive index for marine particles: comparison with independent and bulk estimates”, *Applied Optics*, vol. 42, pp. 526–541, 2003.
- [70] R.W. Spinrad and J.F. Brown, “Relative real refractive index of marine microorganisms: a technique for flow cytometric estimation”, *Applied Optics*, vol. 25, pp. 1930–1934, 1986.
- [71] R. Barer and S. Joseph, “Refractometry of living cells. part I: Basic principles”, *Quarterly Journal of Microscopical Science*, vol. 96, pp. 399–423, 1954.
- [72] M.D. DuRand and R.J. Olson, “Diel patterns in optical properties of the chlorophyte *Nannochloris* sp.: Relating individual-cell to bulk measurements”, *Limnology and Oceanography*, vol. 43, pp. 1107–1118, 1998.
- [73] J.F. Cornet, C.G. Dussap, and G. Dubertret, “A structured model for simulation of cultures of the cyanobacterium *spirulina platensis* in photobioreactors: I. Coupling between light transfer and growth kinetics”, *Biotechnology and Bioengineering*, vol. 40, no. 7, pp. 817–825, 1992.
- [74] J.F. Cornet, C.G. Dussap, J.B. Gross, C. Binois, and C. Lasseur, “A simplified monodimensional approach for modeling coupling between radiant light transfer and growth kinetics in photobioreactors”, *Chemical Engineering Science*, vol. 50, no. 9, pp. 1489–1500, 1995.
- [75] L.M. Duysens, “The flattening of the absorption spectra of suspensions as compared to that of solutions”, *Biochimica et Biophysica Acta*, vol. 19, pp. 1–12, 1956.
- [76] D. Stramski, A. Morel, and A. Bricaud, “Modeling the light attenuation and scattering by spherical phytoplanktonic cells: a retrieval of the bulk refractive index”, *Applied Optics*, vol. 27, pp. 3954–3957, 1988.
- [77] L. Pilon, H. Berberoğlu, and R. Kandilian, “Radiation transfer in photobiological carbon dioxide fixation and fuel production by microalgae”, *Journal of Quantitative Spectroscopy and Radiation Transfer*, vol. 112, no. 17, pp. 2639–2660, 2011.

- [78] G. Mie, “Beiträge zur Optik trüber Medien, speziell kolloidaler Metallsungen”, *Annalen der Physik*, vol. 25, no. 3, pp. 377–445, 1908.
- [79] M. I. Mishchenko and L. D. Travis, “Capabilities and limitations of a current FORTRAN implementation of the T-matrix method for randomly oriented, rotationally symmetric scatterers”, *Journal of Quantitative Spectroscopy and Radiative Transfer*, vol. 60, no. 3, pp. 309–324, 1998.
- [80] P. Metzger, C. Berkaloof, E. Casadevall, and A. Coute, “Alkadiene- and botryococ-
ceneproducing races of wild strains of *Botryococcus braunii*”, *Phytochemistry*, vol. 24,
no. 10, pp. 2305–2320, 1985.
- [81] S. Sawayama, S. Inoue, and S. Yokoyama, “Continuous culture of hydrocarbon-rich
microalga *Botryococcus braunii* in secondarily treated sewage”, *Applied Microbiology
and Biotechnology*, vol. 41, no. 6, pp. 729–731, 1994.
- [82] J. Sheehan, T. Dunahay, J. Benemann, and P. Roessler, “A look back at the U.S.
Department of Energy’s aquatic species program - Biodiesel from algae”, Tech. Rep.
TP-580-24190, NREL, 1998.
- [83] Y. Chisti, “Biodiesel from algae”, *Biotechnology Advances*, vol. 25, pp. 294–306, 2007.
- [84] J.Y. Lee, T.S. Kwon, K. Baek, and J.W. Yang, “Biological fixation of CO₂ by *Chlorella*
sp. HA-1 in a semi-continuous and series reactor system”, *Journal of Microbiology and
Biotechnology*, vol. 15, no. 3, pp. 461–465, 2005.
- [85] S.Y. Chiu, C.Y. Kao, C.H. Chen, T.C. Kuan, S.C. Ong, and C.S. Lin, “Reduction of
CO₂ by a high-density culture of *Chlorella sp.* in a semicontinuous photobioreactor”,
Bioresource Technology, vol. 99, no. 9, pp. 3389–3396, 2008.
- [86] M. Kodama, H. Ikemoto, and S. Miyachi, “A new species of highly CO₂-tolerant
fast growing marine microalga suitable for high density culture”, *Journal of Marine
Biotechnology*, vol. 1, pp. 21–25, 1993.
- [87] Q. Hu, K. Kurano, M. Kawachi, I. Iwasaki, and S. Miyachi, “Ultrahigh cell density
culture of a marine green algae *Chlorococcum littorale* in a flat plate photobioreactor”,
Applied Microbiology and Biotechnology, vol. 49, pp. 655–662, 1998.
- [88] A. Quirantes and S. Bernard, “Light-scattering methods for modelling algal particles
as a collection of coated and/or nonspherical scatterers”, *Journal of Quantitative
Spectroscopy and Radiative Transfer*, vol. 100, pp. 315–324, 2006.
- [89] M.E. Baird, “Numerical approximations of the mean absorption cross-section of a
variety of randomly oriented microalgal shapes”, *Journal of Mathematical Biology*, vol.
47, pp. 325–336, 2003.

- [90] M.I. Mishchenko and L.D. Travis, “Light scattering by polydispersions of randomly oriented spheroids with sizes comparable to wavelengths to observation”, *Applied Optics*, vol. 33, no. 30, pp. 7206–7225, 1994.
- [91] W.S. Rasband, “ImageJ”, U.S. National Institute of Health, Bethesda, Maryland, USA, <http://rsb.info.nih.gov/ij/>, 1997-2007.
- [92] M.F. Modest, *Radiative Heat Transfer*, Academic Press, San Diego, CA, 2003.
- [93] E. Lee, R-L. Heng, and L. Pilon, “Spectral optical properties of selected photosynthetic microalgae producing biofuels”, *JQSRT*.
- [94] T. Baeck, *Genetic Algorithms in Theory and Practice*, The Oxford University Press, Oxford, UK, 1996.
- [95] P. Charbonneau, “Genetic algorithms in astronomy and astrophysics”, *The Astrophysical Journal*, vol. 101, pp. 309, 1995.
- [96] P. Charbonneau and B. Knapp, “A User’s guide to PIKAIA 1.0”, Tech. Rep. NCAR Technical Note 418+IA, National Center for Atmospheric Research, 1995.
- [97] P. Charbonneau, “An Introduction to Genetic Algorithms for Numerical Optimization”, Tech. Rep. NCAR Technical Note 450+IA, National Center for Atmospheric Research, 2002.
- [98] P. Charbonneau, “Release Notes for PIKAIA 1.2”, Tech. Rep. NCAR Technical Note 451+STR, National Center for Atmospheric Research, 2002.
- [99] A. Morel and A. Bricaud, “Inherent optical properties of algal cells including picoplankton: Theoretical and experimental results”, *Canadian Bulletin of Fisheries and Aquatic Sciences*, pp. 521–560, 1986.
- [100] O. Zhernovaya, O. Sydoruk, V. Tuchin, and A. Douplik, “The refractive index of human hemoglobin in the visible range”, *Physics in Medicine and Biology*, vol. 56, no. 13, pp. 4013–4021, 2011.
- [101] G. M. Hale and M. R. Querry, “Optical constants of water in the 200-nm to 200-m wavelength region”, *Applied Optics*, vol. 12, pp. 555563, 1973.
- [102] X. Ma, J.Q. Lu, R.S. Brock, K.M. Jacobs, P. Yang, and H.H. Hu, “Determination of complex refractive index of polystyrene microspheres from 370 to 1610 nm”, *Physics of Medical Biology*, vol. 48, pp. 4165–4172, 2003.
- [103] I. D. Nikolov and C. D. Ivanov, “Optical plastic refractive measurements in the visible and the near-infrared regions”, *Applied Optics*, vol. 39, no. 13, pp. 2067–2070, 2000.
- [104] E. Aas, “Refractive index of phytoplankton derived from its metabolite composition”, *Journal of Plankton Research*, vol. 18, no. 12, pp. 2223–2249, 1996.

- [105] V. Ashokkumar and R. Rengasamy, “Mass culture of *Botryococcus braunii* kutz. under open raceway pond for biofuel production”, *Bioresource Technology*, vol. 104, pp. 394–399, 2012.
- [106] M.R. Brown and S.W. Jeffrey, “Biochemical composition of microalgae from the green algal classes Chlorophyceae and Prasinophyceae. 1. Amino acids, sugars and pigments”, *Journal of Experimental Marine Biology and Ecology*, vol. 161, no. 1, pp. 91–113, 1992.
- [107] T. Tanoi, M. Kawachi, and M.M. Watanabe, “Effects of carbon source on growth and morphology of *Botryococcus braunii*”, *Journal of Applied Phycology*, vol. 23, no. 1, pp. 25–33, 2011.
- [108] L. Barsanti and P. Gualtieri, *Algae: Anatomy, Biochemistry, and Biotechnology*, CRC Press, Boca Raton, FL, 2005.
- [109] R.E. Blankenship, *Molecular Mechanisms of Photosynthesis*, Wiley-Blackwell, Hoboken, NJ, 2008.
- [110] P. Falkowski and J. LaRoche, “Acclimation to spectral irradiance in algae”, *J. Phycol*, vol. 27, pp. 8–14, 1991.
- [111] Z. Dubinsky and N. Stambler, “Photoacclimation processes in phytoplankton: mechanisms, consequences, and applications”, *Aquatic Microbial Ecology*, vol. 56, pp. 163–176, 2009.
- [112] R.R. Bidigare, M.E. Ondrusek, J.H. Morrow, and D.A. Kiefer, “*In-vivo* absorption properties of algal pigments”, *Proceedings of the Society of Photo-Optical Instrumentation 1302, Ocean Optics X*, vol. 1302, pp. 290–301, 1990.
- [113] M. Jonasz and G. Fournier, *Light Scattering by Particles in Water: Theoretical and Experimental Foundations*, Academic Press, San Diego, CA, 2007.
- [114] H. Berberoğlu and L. Pilon, “Experimental measurement of the radiation characteristics of *Anabaena variabilis* ATCC 29413-U and *Rhodobacter sphaeroides* ATCC 49419”, *International Journal of Hydrogen Energy*, vol. 32, no. 18, pp. 4772–4785, 2007.
- [115] H. Berberoğlu, L. Pilon, and A. Melis, “Radiation characteristics of *Chlamydomonas reinhardtii* CC125 and its truncated chlorophyll antenna transformants *tla1*, *tlaX* and *tla1-CW+*”, *International Journal of Hydrogen Energy*, vol. 33, no. 22, pp. 6467–6483, 2008.
- [116] J. Dauchet, *Analyse Radiative des Photobioréacteurs*, PhD thesis, Université Blaise Pascal, Clermont Ferrand II, France, 2012.
- [117] E. Lee and L. Pilon, “Absorption and scattering by long and randomly oriented linear chains of spheres”, *Journal of the Optical Society of America A*, vol. 30, no. 9, pp. 1892–1900, 2013.

- [118] J-F. Cornet, C-G. Dussap, and G. Dubertret, “A structured model for simulation of cultures of the cyanobacterium *Spirulina platensis* in photobioreactors: I. Coupling between light transfer and growth kinetics”, *Biotechnology and Bioengineering*, vol. 40, no. 7, pp. 817–825, 1992.
- [119] P.M. Slegers, R.H. Wijffels, G. Van Straten, and A.J.B. Van Boxtel, “Design scenarios for flat panel photobioreactors”, *Applied Energy*, vol. 88, no. 10, pp. 3342–3353, 2011.
- [120] L. Rodolfi, G. Chini Zittelli, N. Bassi, G. Padovani, N. Biondi, G. Bonini, and M.R. Tredici, “Microalgae for oil: Strain selection, induction of lipid synthesis and outdoor mass cultivation in a low-cost photobioreactor”, *Biotechnology and Bioengineering*, vol. 102, no. 1, pp. 100–112, 2009.
- [121] R. Kandilian, E. Lee, and L. Pilon, “Radiation and optical properties of *Nannochloropsis oculata* grown under different irradiances and spectra”, *Bioresource Technology*, vol. 137, pp. 63–73, 2013.
- [122] R.J. Davies-Colley, R.D. Pridmore, and J.E. Hewitt, “Optical properties of some freshwater phytoplanktonic algae”, *Hydrobiologia*, vol. 133, no. 2, pp. 165–178, 1986.
- [123] B.M. Agrawal and M.P. Mengüç, “Forward and inverse analysis of single and multiple scattering of collimated radiation in an axisymmetric system”, *International Journal of Heat and Mass Transfer*, vol. 34, no. 3, pp. 633–647, 1991.
- [124] K.G. Privoznik, K.J. Daniel, and F.P. Incropera, “Absorption, extinction, and phase function measurements for algal suspensions of *Chlorella pyrenoidosa*”, *Journal of Quantitative Spectroscopy and Radiation Transfer*, vol. 20, pp. 345–352, 1978.
- [125] H.C. van de Hulst, *Light Scattering by Small Particles*, Courier Dover Publications, Mineola, NY, 2012.
- [126] A.R. Wellburn, “The spectral determination of chlorophyll a and chlorophyll b, as well as total carotenoids, using various solvents with spectrophotometers of different resolution”, *Journal of Plant Physiology*, vol. 144, no. 3, pp. 307–313, 1994.
- [127] J.D. Strickland and T.R. Parsons, *A Practical Handbook of Seawater Analysis*, Fisheries Research Board of Canada, Ottawa, Canada, 1968.
- [128] E.W. Becker, *Microalgae: Biotechnology and Microbiology*, vol. 10, Cambridge University Press, Cambridge, UK, 1994.
- [129] S-Y. Chiu, C-Y. Kao, M-T. Tsai, S-C. Ong, C-H. Chen, and C-S. Lin, “Lipid accumulation and CO₂ utilization of *Nannochloropsis oculata* in response to CO₂ aeration”, *Bioresource Technology*, vol. 100, no. 2, pp. 833–838, 2009.
- [130] D. Simionato, E. Sforza, E. Corteggiani Carpinelli, A. Bertucco, G.M. Giacometti, and T. Morosinotto, “Acclimation of *Nannochloropsis gaditana* to different illumination

- regimes: Effects on lipids accumulation”, *Bioresource Technology*, vol. 102, no. 10, pp. 6026–6032, 2011.
- [131] E. Aas, “Refractive index of phytoplankton derived from its metabolite composition”, *Journal of Plankton Research*, vol. 18, no. 12, pp. 2223–2249, 1996.
 - [132] S.M. Renaud, D.L. Parry, L-V. Thinh, C. Kuo, A. Padovan, and N. Sammy, “Effect of light intensity on the proximate biochemical and fatty acid composition of *Isochrysis sp.* and *Nannochloropsis oculata* for use in tropical aquaculture”, *Journal of Applied Phycology*, vol. 3, no. 1, pp. 43–53, 1991.
 - [133] L. de Vasconcelos and P. Fay, “Nitrogen metabolism and ultrastructure in *Anabaena cylindrica*”, *Archives of Microbiology*, vol. 96, no. 1, pp. 271–279, 1974.
 - [134] E. Lee and L. Pilon, “Light scattering by long and randomly oriented linear chains of spheres”, *Journal of the Optical Society of America A*, vol. 30, no. 9, pp. 1892–1900, 2013.
 - [135] P. Fay, “Photostimulation of nitrogen fixation in *Anabaena cylindrica*”, *Biochimica et Biophysica Acta (BBA) - Bioenergetics*, vol. 216, no. 2, pp. 353 – 356, 1970.
 - [136] N.M. Weare and J.R. Benemann, “Nitrogen fixation by *Anabaena cylindrica*”, *Archives of Microbiology*, vol. 90, no. 4, pp. 323–332, 1973.
 - [137] W.D.P. Stewart and P. Rowell, “Effects of l-methionine-dl-sulphoximine on the assimilation of newly fixed nh_3 , acetylene reduction and heterocyst production in *Anabaena Cylindrica*”, *Biochemical And Biophysical Research Communications*, vol. 65, no. 3, pp. 846–856, 1975.
 - [138] J.R. Benemann, “Production of nitrogenfertilizer with nitrogen-fixing blue - green algae”, *Enzyme and Microbial Technology*, vol. 1, pp. 83–90, 1979.
 - [139] P. Fay, “Cell differentiation and pigment composition in *Anabaena cylindrica*”, *Archives of Microbiology*, vol. 67, no. 1, pp. 62–70, 1969.
 - [140] C.P. Wolk and R.D. Simon, “Pigments and lipids of heterocysts”, *Planta*, vol. 86, pp. 92–97, 1969.
 - [141] T.R. Parsons, K. Stephens, and J.D.H. Strickland, “On the chemical composition of eleven species of marine phytoplanktons”, *Journal of Fisheries Research Board of Canada*, vol. 18, pp. 1001 – 1016, 1961.
 - [142] P. J. le B. Williams and L.M.L. Laurens, “Microalgae as biodiesel and biomass feedstocks: Review and analysis of the biochemistry, energetics and economics”, *Energy Environmental Science*, vol. 3, pp. 554–590, 2010.
 - [143] P.A. Roger, A. Tirol, S. Ardales, and I. Watanabe, “Chemical composition of cultures and natural samples of N_2 -fixing blue-green algae from rice fields”, *Biology and Fertility of Soils*, vol. 2, pp. 131–146, 1986.

- [144] D.C. Sigee, J. Teper, and E. Levado, “Elemental composition of the cyanobacterium *Anabaena flos-aquae* collected from different depths within a stratified lake”, *European Journal of Phycology*, vol. 34, no. 5, pp. 477–485, 1999.
- [145] R.J. Davies-Colley, R.D. Pridmore, and J.E. Hewitt, “Optical properties and reflectance spectra of 3 shallow lakes obtained from a spectrophotometric study”, *New Zealand Journal of Marine and Freshwater Research*, vol. 17, no. 4, pp. 445–459, 1983.
- [146] E. Lee, R-L. Heng, and L. Pilon, “Spectral optical properties of selected photosynthetic microalgae producing biofuels”, *Journal of Quantitative Spectroscopy and Radiation Transfer*, vol. 114, pp. 112–135, 2013.
- [147] M. Kerker, *The Scattering of Light, and Other Electromagnetic Radiation*, Academic Press, New York, NY, 1969.
- [148] P.F. Brownell and D.J.D. Nicholas, “Some effects of sodium on nitrate assimilation and N₂ fixation in *Anabaena cylindrica*”, *Plant Physiology*, vol. 42, no. 3, pp. 915–921, 1967.
- [149] M.M. Allen and A.J. Smith, “Nitrogen chlorosis in blue-green algae”, *Archives of Microbiology*, vol. 69, no. 2, pp. 114–120, 1969.
- [150] M.M. Allen and F. Hutchison, “Nitrogen limitation and recovery in the cyanobacterium *Aphanocapsa* 6308”, *Archives of Microbiology*, vol. 128, no. 1, pp. 1–7, 1980.
- [151] I. Canto de Loura, J.P. Dubacq, and J.C. Thomas, “The effects of nitrogen deficiency on pigments and lipids of cyanobacteria”, *Plant Physiology*, vol. 83, no. 4, pp. 838–843, 1987.
- [152] M.J. Griffiths, C. Garcin, R.P. van Hille, and S.T. Harrison, “Interference by pigment in the estimation of microalgal biomass concentration by optical density”, *Journal of Microbiological Methods*, vol. 85, pp. 199–123, 2011.
- [153] R. Kitamura, L. Pilon, and M. Jonasz, “Optical constants of silica glass from extreme ultraviolet to far infrared at near room temperature”, *Applied optics*, vol. 46, no. 33, pp. 8118–8133, 2007.
- [154] I.H. Malitson, “Interspecimen comparison of the refractive index of fused silica”, *Journal of the Optical Society of America*, vol. 55, no. 10, pp. 1205–1209, 1965.
- [155] B.E. Schirrmeister, J.M. de Vos, A. Antonelli, and H.C. Bagheri, “Evolution of multicellularity coincided with increased diversification of cyanobacteria and the great oxidation event”, *Proceedings of the National Academy of Sciences*, vol. 110, no. 5, pp. 1791–1796, 2013.
- [156] T. Kaneko, S. Sato, H. Kotani, A. Tanaka, E. Asamizu, Y. Nakamura, N. Miyajima, M. Hirose, M. Sugiura, S. Sasamoto, T. Kimura, T. Hosouchi, A. Matsuno,

- A. Muraki, N. Nakazaki, K. Naruo, S. Okumura, S. Shimpō, C. Takeuchi, T. Wada, A. Watanabe, M. Yamada, M. Yasuda, and S. Tabata, “Sequence analysis of the genome of the unicellular cyanobacterium *Synechocystis* sp. strain PCC6803 II. Sequence determination of the entire genome and assignment of potential protein-coding regions”, *DNA Research*, vol. 3, no. 3, pp. 109–136, 1996.
- [157] Y. Hihara, K. Sonoike, M. Kanehisa, and M. Ikeuchi, “DNA microarray analysis of redox-responsive genes in the genome of the cyanobacterium *Synechocystis* sp. strain PCC 6803”, *Journal of Bacteriology*, vol. 185, no. 5, pp. 1719–1725, 2003.
- [158] D. Lagarde, L. Beuf, and W. Vermaas, “Increased production of zeaxanthin and other pigments by application of genetic engineering techniques to *Synechocystis* sp. strain PCC 6803”, *Applied and Environmental Microbiology*, vol. 66, no. 1, pp. 64–72, 2000.
- [159] M.A. Vega-Palas, F. Madueño, A. Herrero, and E. Flores, “Identification and cloning of a regulatory gene for nitrogen assimilation in the cyanobacterium *Synechocystis* sp. strain PCC 7942”, *Journal of Bacteriology*, vol. 172, no. 2, pp. 643–647, 1990.
- [160] M.G. Pinho, M. Kjos, and J.W. Veening, “How to get (a) round: mechanisms controlling growth and division of coccoid bacteria”, *Nature Reviews Microbiology*, vol. 11, no. 9, pp. 601–614, 2013.
- [161] I. Berman-Frank, P. Lundgren, and P. Falkowski, “Nitrogen fixation and photosynthetic oxygen evolution in cyanobacteria”, *Research in Microbiology*, vol. 154, no. 3, pp. 157–164, 2003.
- [162] J.R. Benemann, “Production of nitrogen fertilizer with nitrogen-fixing blue-green algae”, *Enzyme and Microbial Technology*, vol. 1, no. 2, pp. 83–90, 1979.
- [163] D. Das and T.N. Veziroğlu, “Hydrogen production by biological processes: a survey of literature”, *International Journal of Hydrogen Energy*, vol. 26, no. 1, pp. 13–28, 2001.
- [164] A. Tiwari and A. Pandey, “Cyanobacterial hydrogen production—a step towards clean environment”, *International Journal of Hydrogen Energy*, vol. 37, no. 1, pp. 139–150, 2012.
- [165] H. Berberoğlu, J. Yin, and L. Pilon, “Light transfer in bubble sparged photobioreactors for H₂ production and CO₂ mitigation”, *International Journal of Hydrogen Energy*, vol. 32, no. 13, pp. 2273–2285, 2007.
- [166] A.L. Aden and M. Kerker, “Scattering of electromagnetic waves from two concentric spheres”, *Journal of Applied Physics*, vol. 22, no. 10, pp. 1242–1246, 1951.
- [167] M. Kerker, *The Scattering of Light, and other Electromagnetic Radiation*, Academic Press, New York, NY, 1969.
- [168] J.R. Wait, “Scattering of a plane wave from a circular dielectric cylinder at oblique incidence”, *Canadian Journal of Physics*, vol. 33, no. 5, pp. 189–195, 1955.

- [169] P.C. Waterman, “Matrix formulation of electromagnetic scattering”, *Proceedings of the Institute of Electrical and Electronics Engineers*, vol. 53, no. 8, pp. 805–812, 1965.
- [170] D.W. Mackowski, “Calculation of total cross sections of multiple-sphere clusters”, *Journal of the Optical Society of America A*, vol. 11, no. 11, pp. 2851–2861, 1994.
- [171] M.I. Mishchenko, L.D. Travis, and A.A. Lacis, *Scattering, Absorption, and Emission of Light by Small Particles*, Cambridge University Press, Cambridge, UK, 2002.
- [172] M.I. Mishchenko, D.W. Mackowski, and L.D. Travis, “Scattering of light by bispheres with touching and separated components”, *Applied Optics*, vol. 34, no. 21, pp. 4589–4599, 1995.
- [173] B.T. Draine, “The discrete-dipole approximation and its application to interstellar graphite grains”, *The Astrophysical Journal*, vol. 333, pp. 848–872, 1988.
- [174] K.N. Liou, *An Introduction to Atmospheric Radiation*, Academic Press, Waltham, MA, 2002.
- [175] A. Bricaud and A. Morel, “Light attenuation and scattering by phytoplanktonic cells: a theoretical modeling”, *Applied Optics*, vol. 25, no. 4, pp. 571–580, 1986.
- [176] A. Quirantes and S. Bernard, “Light-scattering methods for modelling algal particles as a collection of coated and/or nonspherical scatterers”, *Journal of Quantitative Spectroscopy and Radiative Transfer*, vol. 100, no. 1, pp. 315–324, 2006.
- [177] E. Lee, R.L. Heng, and L. Pilon, “Spectral optical properties of selected photosynthetic microalgae producing biofuels”, *Journal of Quantitative Spectroscopy and Radiative Transfer*, vol. 114, pp. 122 – 135, 2013.
- [178] R.L. Heng, E. Lee, and L. Pilon, “Radiation characteristics and optical properties of filamentous cyanobacterium *Anabaena cylindrica*”, *Journal of the Optical Society of America A*, vol. 31, no. 4, pp. 836–845, 2014.
- [179] C.F. Bohren and D.R. Huffman, *Absorption and Scattering of Light by Small Particles*, John Wiley and Sons, New York, NY, 1998.
- [180] S. Manickavasagam and M.P. Mengüç, “Scattering-matrix elements of coated infinite-length cylinders”, *Applied Optics*, vol. 37, no. 12, pp. 2473–2482, 1998.
- [181] H.R. Gordon, “Light scattering and absorption by randomly-oriented cylinders: dependence on aspect ratio for refractive indices applicable for marine particles”, *Optics Express*, vol. 19, no. 5, pp. 4673–4691, 2011.
- [182] M.I. Mishchenko, G. Videen, V.A. Babenko, N.G. Khlebtsov, and T. Wriedt, “T-matrix theory of electromagnetic scattering by particles and its applications: a comprehensive reference database”, *Journal of Quantitative Spectroscopy and Radiative Transfer*, vol. 88, no. 1-3, pp. 357–406, 2004.

- [183] B.N. Khlebtsov, V.A. Khanadeyev, J. Ye, D.W. Mackowski, G. Borghs, and N.G. Khlebtsov, “Coupled plasmon resonances in monolayers of metal nanoparticles and nanoshells”, *Physical Review B*, vol. 77, no. 3, pp. 035440, 2008.
- [184] L.L. Zhao, K.L. Kelly, and G.C. Schatz, “The extinction spectra of silver nanoparticle arrays: influence of array structure on plasmon resonance wavelength and width”, *The Journal of Physical Chemistry B*, vol. 107, no. 30, pp. 7343–7350, 2003.
- [185] H. Kimura, L. Kolokolova, and I. Mann, “Optical properties of cometary dust: constraints from numerical studies on light scattering by aggregate particles”, *Astronomy and Astrophysics*, vol. 407, no. 1, pp. L5–L8, 2003.
- [186] D.W. Mackowski and M.I. Mishchenko, “Calculation of the T matrix and the scattering matrix for ensembles of spheres”, *Journal of the Optical Society of America A*, vol. 13, no. 11, pp. 2266–2278, 1996.
- [187] M.P. Mengüç, S. Manickavasagam, and D.A. D’Sa, “Determination of radiative properties of pulverized coal particles from experiments”, *Fuel*, vol. 73, no. 4, pp. 613–625, 1994.
- [188] K.N. Liou and Y. Takano, “Light scattering by nonspherical particles: Remote sensing and climatic implications”, *Atmospheric Research*, vol. 31, no. 4, pp. 271–298, 1994.
- [189] F.M. Kahnert, J.J. Stamnes, and K. Stamnes, “Can simple particle shapes be used to model scalar optical properties of an ensemble of wavelength-sized particles with complex shapes?”, *Journal of the Optical Society of America A*, vol. 19, no. 3, pp. 521–531, 2002.
- [190] P. Yang, G.W. Kattawar, and W.J. Wiscombe, “Effect of particle asphericity on single-scattering parameters: comparison between platonic solids and spheres”, *Applied Optics*, vol. 43, no. 22, pp. 4427–4435, 2004.
- [191] P. Latimer, “Experimental tests of a theoretical method for predicting light scattering by aggregates”, *Applied Optics*, vol. 24, no. 19, pp. 3231–3239, 1985.
- [192] B.L. Drolen and C.L. Tien, “Absorption and scattering of agglomerated soot particulate”, *Journal of Quantitative Spectroscopy and Radiative Transfer*, vol. 37, no. 5, pp. 433–448, 1987.
- [193] K. Kumar, C.N. Dasgupta, B. Nayak, P. Lindblad, and D. Das, “Development of suitable photobioreactors for CO₂ sequestration addressing global warming using green algae and cyanobacteria”, *Bioresource Technology*, vol. 102, no. 8, pp. 4945–4953, 2011.
- [194] D.J. Brown and G.T. Vickers, “The use of projected area distribution functions in particle shape measurement”, *Powder Technology*, vol. 98, no. 3, pp. 250–257, 1998.

- [195] D.W. Mackowski and M.I. Mishchenko, “A multiple sphere T-matrix Fortran code for use on parallel computer clusters”, *Journal of Quantitative Spectroscopy and Radiative Transfer*, vol. 112, no. 13, pp. 2182–2192, 2011.
- [196] C. Mätzler, “MATLAB functions for Mie scattering and absorption, version 2”, *Institut für Angewandte Physik Research Report No. 2002-11*, vol. 8, 2002.
- [197] T.L. Farias, Ü.Ö. Köylü, and M.G. Carvalho, “Range of validity of the Rayleigh-Debye-Gans theory for optics of fractal aggregates”, *Applied Optics*, vol. 35, no. 33, pp. 6560–6567, 1996.
- [198] R.A. West, “Optical properties of aggregate particles whose outer diameter is comparable to the wavelength”, *Applied Optics*, vol. 30, no. 36, pp. 5316–5324, 1991.
- [199] L. Liu and M.I. Mishchenko, “Effects of aggregation on scattering and radiative properties of soot aerosols”, *Journal of Geophysical Research: Atmospheres*, vol. 110, no. D11, 2005.
- [200] R.L. Heng and L. Pilon, “Time-dependent radiation characteristics of *Nannochloropsis oculata* during batch culture”, *Journal of Quantitative Spectroscopy and Radiative Transfer*, vol. 144, pp. 154–163, 2014.
- [201] R.L. Heng, K.C. Sy, and L. Pilon, “Absorption and scattering by bispheres, quad-spheres, and circular rings of spheres and their equivalent coated spheres”, *Journal of the Optical Society of America A*, vol. Manuscript ID: 217647.
- [202] R. Kandilian, R.L. Heng, K.C. Sy, and L. Pilon, “Absorption and scattering by fractal aggregates and by their equivalent coated spheres”, *Journal of Quantitative Spectroscopy and Radiative Transfer*, vol. Manuscript ID: JQSRT-D-14-00262.
- [203] M. Scott, C. McCollum, S. Vasil’ev, C. Crozier, G.S. Espie, M. Krol, N.P.A. Huner, and D. Bruce, “Mechanism of the down regulation of photosynthesis by blue light in the cyanobacterium *Synechocystis* sp. PCC 6803”, *Biochemistry*, vol. 45, no. 29, pp. 8952–8958, 2006.
- [204] D. Stramski, G. Rosenberg, and L. Legendre, “Photosynthetic and optical properties of the marine chlorophyte *Dunaliella tertiolecta* grown under fluctuating light caused by surface-wave focusing”, *Marine Biology*, vol. 115, no. 3, pp. 363–372, 1993.
- [205] D. Stramski and A. Morel, “Optical properties of photosynthetic picoplankton in different physiological states as affected by growth irradiance”, *Deep Sea Research Part A. Oceanographic Research Papers*, vol. 37, no. 2, pp. 245–266, 1990.
- [206] C.M. Sorensen, “Light scattering by fractal aggregates: a review”, *Aerosol Science and Technology*, vol. 35, no. 2, pp. 648–687, 2001.

- [207] M. Woźniak, F.R.A. Onofri, S. Barbosa, J. Yon, and J. Mroczka, “Comparison of methods to derive morphological parameters of multi-fractal samples of particle aggregates from TEM images”, *Journal of Aerosol Science*, vol. 47, pp. 12–26, 2012.
- [208] J. Mroczka, M. Woźniak, and F.R.A. Onofri, “Algorithms and methods for analysis of the optical structure factor of fractal aggregates”, *Metrology and Measurement Systems*, vol. 19, no. 3, pp. 459–470, 2012.
- [209] K. Skorupski, J. Mroczka, T. Wriedt, and N. Riefler, “A fast and accurate implementation of tunable algorithms used for generation of fractal-like aggregate models”, *Physica A: Statistical Mechanics and its Applications*, vol. 404, pp. 106–117, 2014.
- [210] G.A. Jackson, R. Maffione, D.K. Costello, A.L. Alldredge, B.E. Logan, and H.G. Dam, “Particle size spectra between 1 μm and 1 cm at monterey bay determined using multiple instruments”, *Deep Sea Research Part I: Oceanographic Research Papers*, vol. 44, no. 11, pp. 1739–1767, 1997.
- [211] R.R.L. Guillard and J.H. Ryther, “Studies of marine planktonic diatoms: I. *Cyclotella nana* hustedt, and *Detonula confervacea* (cleve) gran.”, *Canadian Journal of Microbiology*, vol. 8, no. 2, pp. 229–239, 1962.
- [212] X. Su, P.G. Fraenkel, and L. Bogorad, “Excitation energy transfer from phycocyanin to chlorophyll in an apcA-defective mutant of *Synechocystis* sp. PCC 6803.”, *Journal of Biological Chemistry*, vol. 267, no. 32, pp. 22944–22950, 1992.